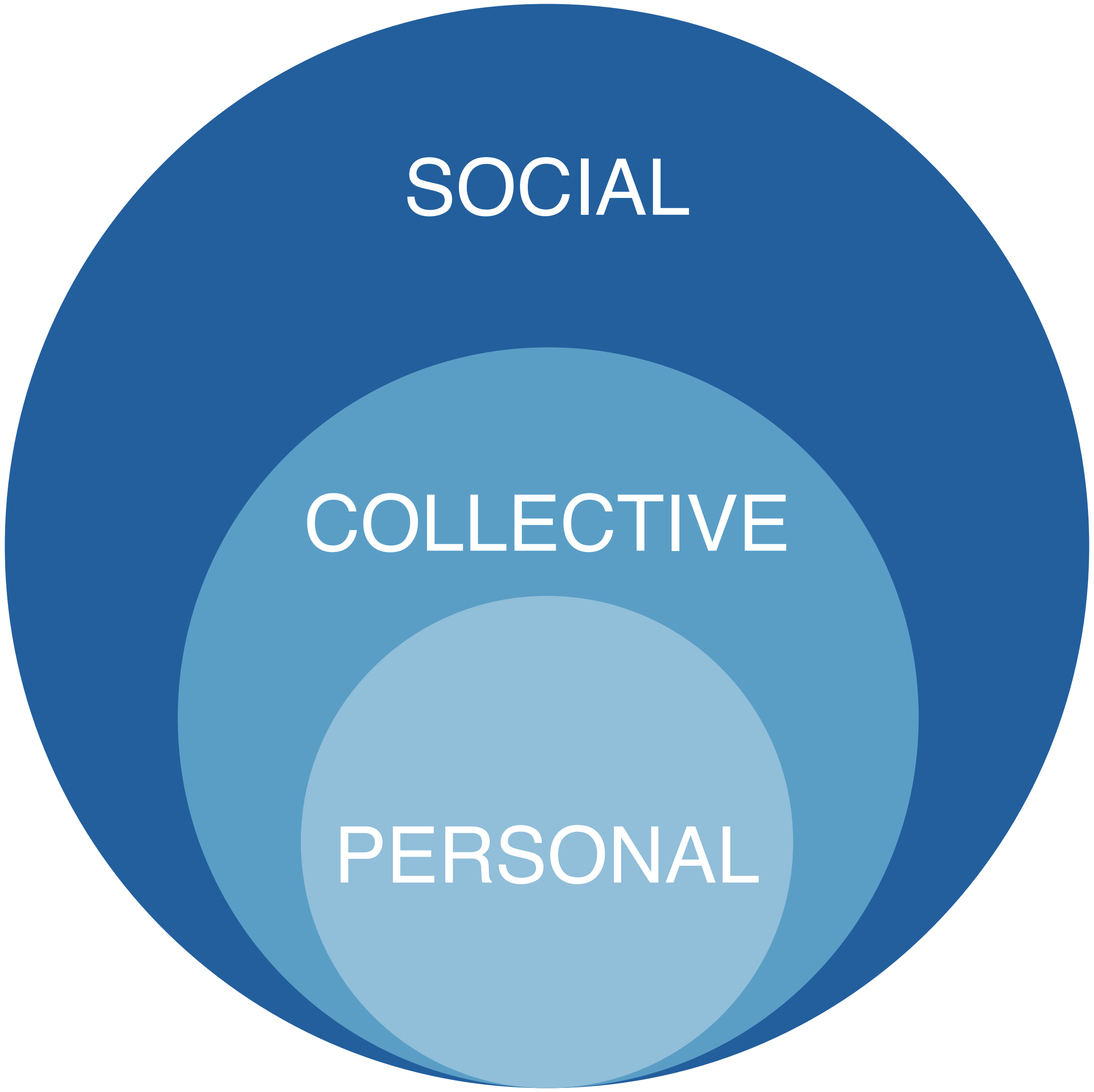
SOCIAL
COLLECTIVE
PERSONAL


illa *BD*. Eodem argumento in fine temporis ejuſdem reperietur alicubi in linea *CD*, & idcirco in utriuſq; lineæ concurſu *D* reperiri neceſſe eſt.

Corol. II.

Et hinc patet compoſitio vis directæ AD ex viribus quibuſvis obliquis AB & BD, & viciſſim reſolutio vis cujuſvis directæ AD in obliquas quaſcunq; AB & BD. Quæ quidem Compoſitio & reſolutio abunde confirmatur ex Mechanica.

Ut ſi de rotæ alicujus centro O exeuntes radij inæquales *OM*, *ON* filis *MA*, *NP* ſuſtineant pondera *A* & *P*, & quærantur vires ponderum ad movendam rotam: per centrum O agatur recta *KOL* filis perpendiculariter occurrens in *K* & *L*, centroq; O & intervallorum *OK*, *OL*, majore *OL*, deſcribatur circulus occurrens filo *MA* in *D*: & actæ rectæ *OD* parallela ſit *AC* & perpendicularis *DC*. Quoniam nihil refert utrum filorum puncta *K*, *L*, *D* affixa ſint vel non affixa ad planum rotæ, pondera idem valebunt ac ſi ſuſpenderentur a punctis *K* & *L* vel *D* & *L*. Ponderis autem *A* exponatur vis tota per lineam *AD*, & hæc reſolvetur in vires *AC*, *CD*, quarum *AC* trahendo radium *OD* directe a centro nihil valet ad movendam rotam; vis autem altera *DC*, trahendo radium *DO* perpendiculariter, idem valet ac ſi perpendiculariter traheret radium *OL* ipſi *OD* æqualem; hoc eſt idem atq; pondus *P*, ~~quod ſit~~ ad pondus *A* ut vis *DC* ad vim *DA*, id eſt (ob ſimilia triangula *ADC*, *DOK*,) ut *OK* (ad *OD*) ad *OL*. Pondera igitur *A* & *P*, quæ ſunt reciproce ut radii in directum poſiti *OK* & *OL*, idem pollebunt & ſic conſiſtent in æquilibrio: (quæ eſt proprietas notiſſima Libræ, Vectis

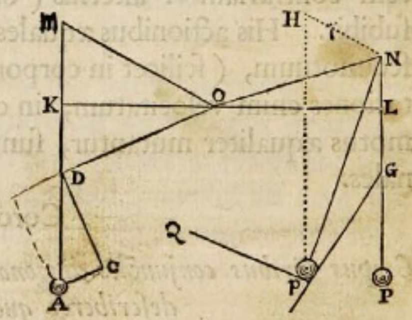

Si modo pondus illud sit

propagation time, the events have a combined signal-to-noise ratio (SNR) of 24 [45].

Only the LIGO detectors were observing at the time of GW150914. The Virgo detector was being upgraded, and GEO 600, though not sufficiently sensitive to detect this event, was operating but not in observational mode. With only two detectors the source position is primarily determined by the relative arrival time and localized to an area of approximately 600 deg^2 (90% credible region) [39,46].

The basic features of GW150914 point to it being produced by the coalescence of two black holes—i.e., their orbital inspiral and merger, and subsequent final black hole ringdown. Over 0.2 s, the signal increases in frequency and amplitude in about 8 cycles from 35 to 150 Hz, where the amplitude reaches a maximum. The most plausible explanation for this evolution is the inspiral of two orbiting masses, m_1 and m_2, due to gravitational-wave emission. At the lower frequencies, such evolution is characterized by the chirp mass [11]

$$\mathcal{M} = \frac{(m_1 m_2)^{3/5}}{(m_1+m_2)^{1/5}} = \frac{c^3}{G}\left[\frac{5}{96}\pi^{-8/3} f^{-11/3} \dot{f}\right]^{3/5},$$

where f and $\dot{f}$ are the observed frequency and its time derivative and G and c are the gravitational constant and speed of light. Estimating f and $\dot{f}$ from the data in Fig. 1, we obtain a chirp mass of $\mathcal{M} \simeq 30 M_\odot$, implying that the total mass $M = m_1 + m_2$ is $\gtrsim 70 M_\odot$ in the detector frame. This bounds the sum of the Schwarzschild radii of the binary components to $2GM/c^2 \gtrsim 210$ km. To reach an orbital frequency of 75 Hz (half the gravitational-wave frequency) the objects must have been very close and very compact; equal Newtonian point masses orbiting at this frequency would be only ≃350 km apart. A pair of neutron stars, while compact, would not have the required mass, while a black hole neutron star binary with the deduced chirp mass would have a very large total mass, and would thus merge at much lower frequency. This leaves black holes as the only known objects compact enough to reach an orbital frequency of 75 Hz without contact. Furthermore, the decay of the waveform after it peaks is consistent with the damped oscillations of a black hole relaxing to a final stationary Kerr configuration. Below, we present a general-relativistic analysis of GW150914; Fig. 2 shows the calculated waveform using the resulting source parameters.

III. DETECTORS

Gravitational-wave astronomy exploits multiple, widely separated detectors to distinguish gravitational waves from local instrumental and environmental noise, to provide source sky localization, and to measure wave polarizations. The LIGO sites each operate a single Advanced LIGO

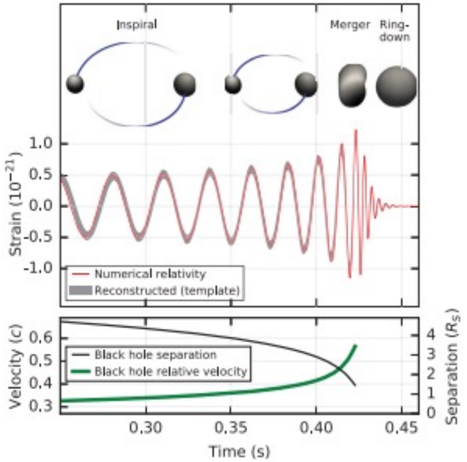

FIG. 2. *Top:* Estimated gravitational-wave strain amplitude from GW150914 projected onto H1. This shows the full bandwidth of the waveforms, without the filtering used for Fig. 1. The inset images show numerical relativity models of the black hole horizons as the black holes coalesce. *Bottom:* The Keplerian effective black hole separation in units of Schwarzschild radii ($R_S = 2GM/c^2$) and the effective relative velocity given by the post-Newtonian parameter $v/c = (GM\pi f/c^3)^{1/3}$, where f is the gravitational-wave frequency calculated with numerical relativity and M is the total mass (value from Table I).

detector [33], a modified Michelson interferometer (see Fig. 3) that measures gravitational-wave strain as a difference in length of its orthogonal arms. Each arm is formed by two mirrors, acting as test masses, separated by $L_x = L_y = L = 4$ km. A passing gravitational wave effectively alters the arm lengths such that the measured difference is $\Delta L(t) = \delta L_x - \delta L_y = h(t)L$, where h is the gravitational-wave strain amplitude projected onto the detector. This differential length variation alters the phase difference between the two light fields returning to the beam splitter, transmitting an optical signal proportional to the gravitational-wave strain to the output photodetector.

To achieve sufficient sensitivity to measure gravitational waves, the detectors include several enhancements to the basic Michelson interferometer. First, each arm contains a resonant optical cavity, formed by its two test mass mirrors, that multiplies the effect of a gravitational wave on the light phase by a factor of 300 [48]. Second, a partially transmissive power-recycling mirror at the input provides additional resonant buildup of the laser light in the interferometer as a whole [49,50]: 20 W of laser input is increased to 700 W incident on the beam splitter, which is further increased to 100 kW circulating in each arm cavity. Third, a partially transmissive signal-recycling mirror at the output optimizes propagation time, the events have a combined signal-to-noise ratio (SNR) of 24 [45].

Only the LIGO detectors were observing at the time of GW150914. The Virgo detector was being upgraded, and GEO 600, though not sufficiently sensitive to detect this event, was operating but not in observational mode. With only two detectors the source position is primarily determined by the relative arrival time and localized to an area of approximately 600 deg^2 (90% credible region) [39,46].

The basic features of GW150914 point to it being produced by the coalescence of two black holes—i.e., their orbital inspiral and merger, and subsequent final black hole ringdown. Over 0.2 s, the signal increases in frequency and amplitude in about 8 cycles from 35 to 150 Hz, where the amplitude reaches a maximum. The most plausible explanation for this evolution is the inspiral of two orbiting masses, m_1 and m_2, due to gravitational-wave emission. At the lower frequencies, such evolution is characterized by the chirp mass [11]

$$\mathcal{M} = \frac{(m_1 m_2)^{3/5}}{(m_1 + m_2)^{1/5}} = \frac{c^3}{G}\left[\frac{5}{96}\pi^{-8/3} f^{-11/3} \dot{f}\right]^{3/5},$$

where f and $\dot{f}$ are the observed frequency and its time derivative and G and c are the gravitational constant and speed of light. Estimating f and $\dot{f}$ from the data in Fig. 1, we obtain a chirp mass of $\mathcal{M} \simeq 30 M_\odot$, implying that the total mass $M = m_1 + m_2$ is $\gtrsim 70 M_\odot$ in the detector frame. This bounds the sum of the Schwarzschild radii of the binary components to $2GM/c^2 \gtrsim 210$ km. To reach an orbital frequency of 75 Hz (half the gravitational-wave frequency) the objects must have been very close and very compact; equal Newtonian point masses orbiting at this frequency would be only $\simeq$350 km apart. A pair of neutron stars, while compact, would not have the required mass, while a black hole neutron star binary with the deduced chirp mass would have a very large total mass, and would thus merge at much lower frequency. This leaves black holes as the only known objects compact enough to reach an orbital frequency of 75 Hz without contact. Furthermore, the decay of the waveform after it peaks is consistent with the damped oscillations of a black hole relaxing to a final stationary Kerr configuration. Below, we present a general-relativistic analysis of GW150914; Fig. 2 shows the calculated waveform using the resulting source parameters.

III. DETECTORS

Gravitational-wave astronomy exploits multiple, widely separated detectors to distinguish gravitational waves from local instrumental and environmental noise, to provide source sky localization, and to measure wave polarizations. The LIGO sites each operate a single Advanced LIGO

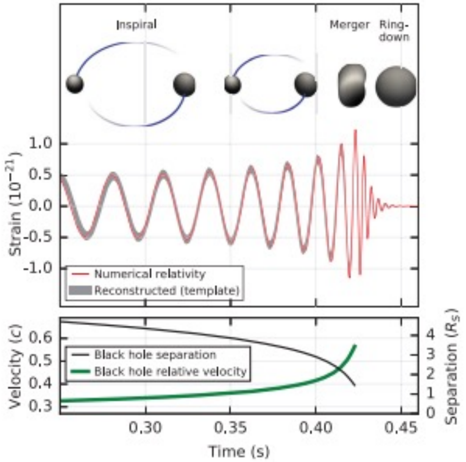

FIG. 2. *Top:* Estimated gravitational-wave strain amplitude from GW150914 projected onto H1. This shows the full bandwidth of the waveforms, without the filtering used for Fig. 1. The inset images show numerical relativity models of the black hole horizons as the black holes coalesce. *Bottom:* The Keplerian effective black hole separation in units of Schwarzschild radii ($R_S = 2GM/c^2$) and the effective relative velocity given by the post-Newtonian parameter $v/c = (GM\pi f/c^3)^{1/3}$, where f is the gravitational-wave frequency calculated with numerical relativity and M is the total mass (value from Table I).

detector [33], a modified Michelson interferometer (see Fig. 3) that measures gravitational-wave strain as a difference in length of its orthogonal arms. Each arm is formed by two mirrors, acting as test masses, separated by $L_x = L_y = L = 4$ km. A passing gravitational wave effectively alters the arm lengths such that the measured difference is $\Delta L(t) = \delta L_x - \delta L_y = h(t)L$, where h is the gravitational-wave strain amplitude projected onto the detector. This differential length variation alters the phase difference between the two light fields returning to the beam splitter, transmitting an optical signal proportional to the gravitational-wave strain to the output photodetector.

To achieve sufficient sensitivity to measure gravitational waves, the detectors include several enhancements to the basic Michelson interferometer. First, each arm contains a resonant optical cavity, formed by its two test mass mirrors, that multiplies the effect of a gravitational wave on the light phase by a factor of 300 [48]. Second, a partially transmissive power-recycling mirror at the input provides additional resonant buildup of the laser light in the interferometer as a whole [49,50]: 20 W of laser input is increased to 700 W incident on the beam splitter, which is further increased to 100 kW circulating in each arm cavity. Third, a partially transmissive signal-recycling mirror at the output optimizes

?

Force11, 2012


SciPy2016
Rowan

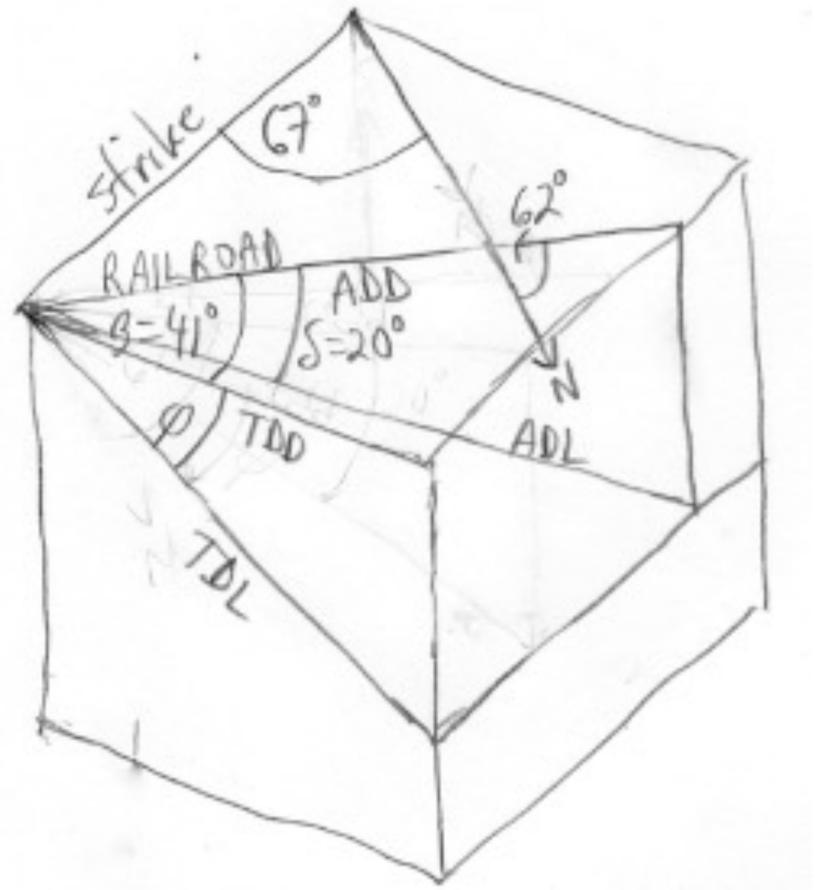
strike
67°
62°
RAILROAD
ADD
β=41°
δ=20°
N
φ
TDD
ADL
TDL

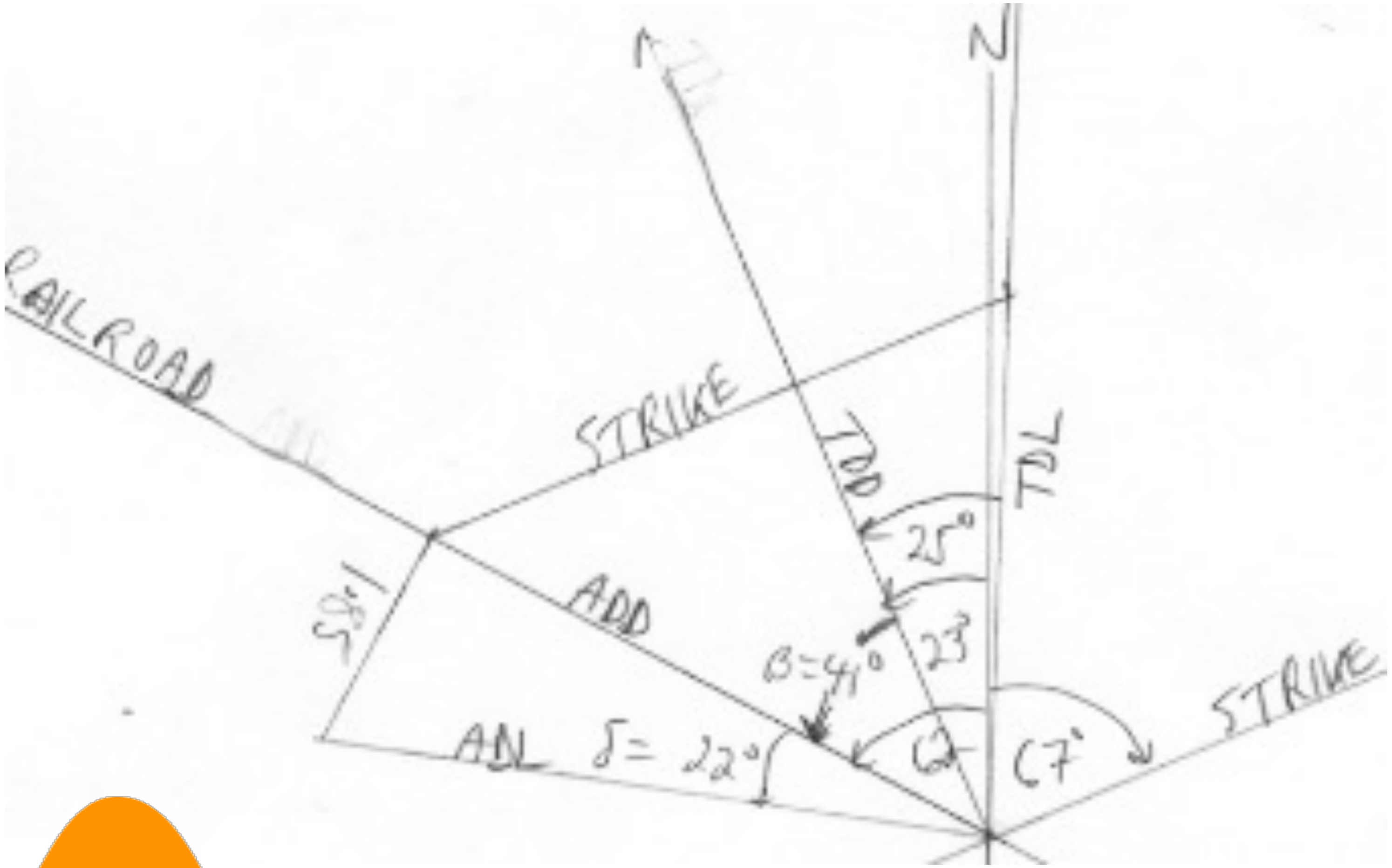
N
RAILROAD
STRIKE
TDD
TDL
25°
23°
ADD
β=41°
ADL
δ= 22°
62
67°
STRIKE

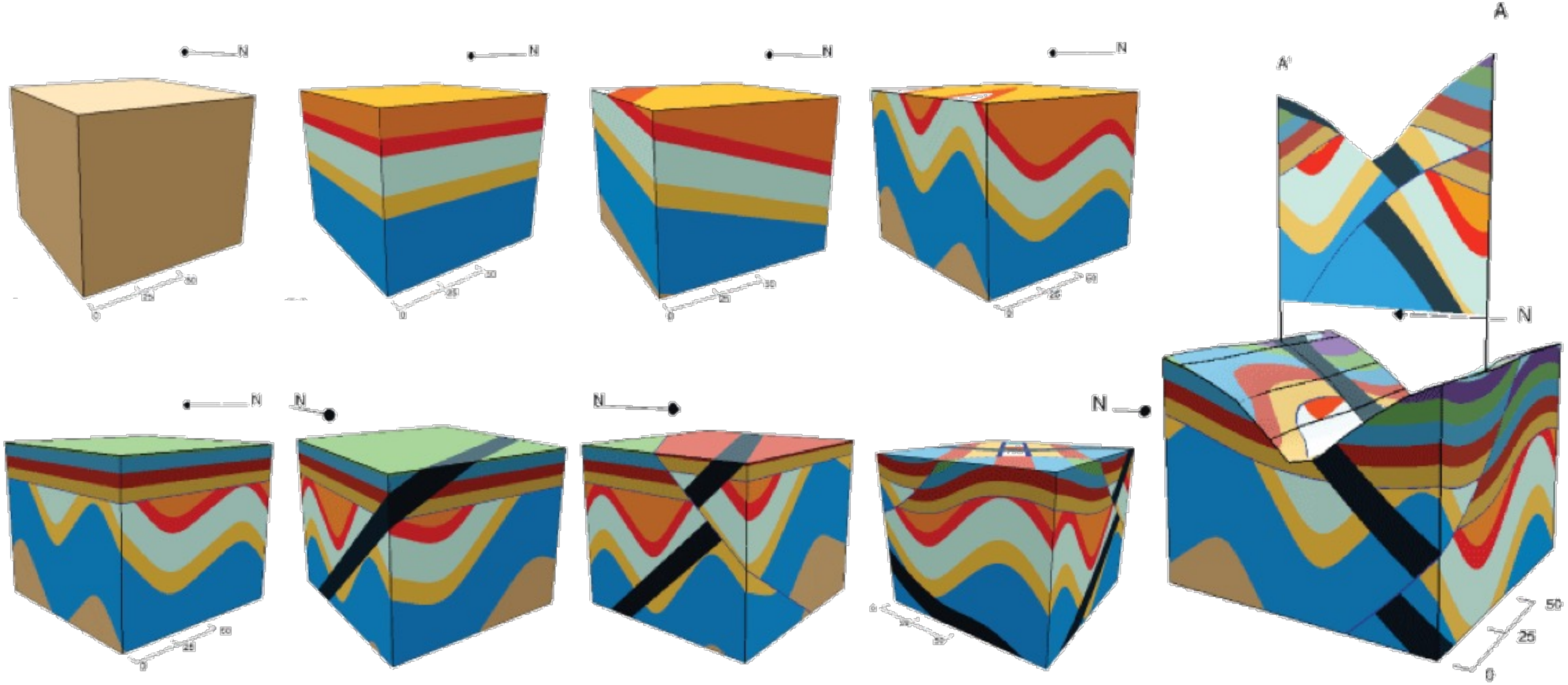
N
A
A'
50
25
0

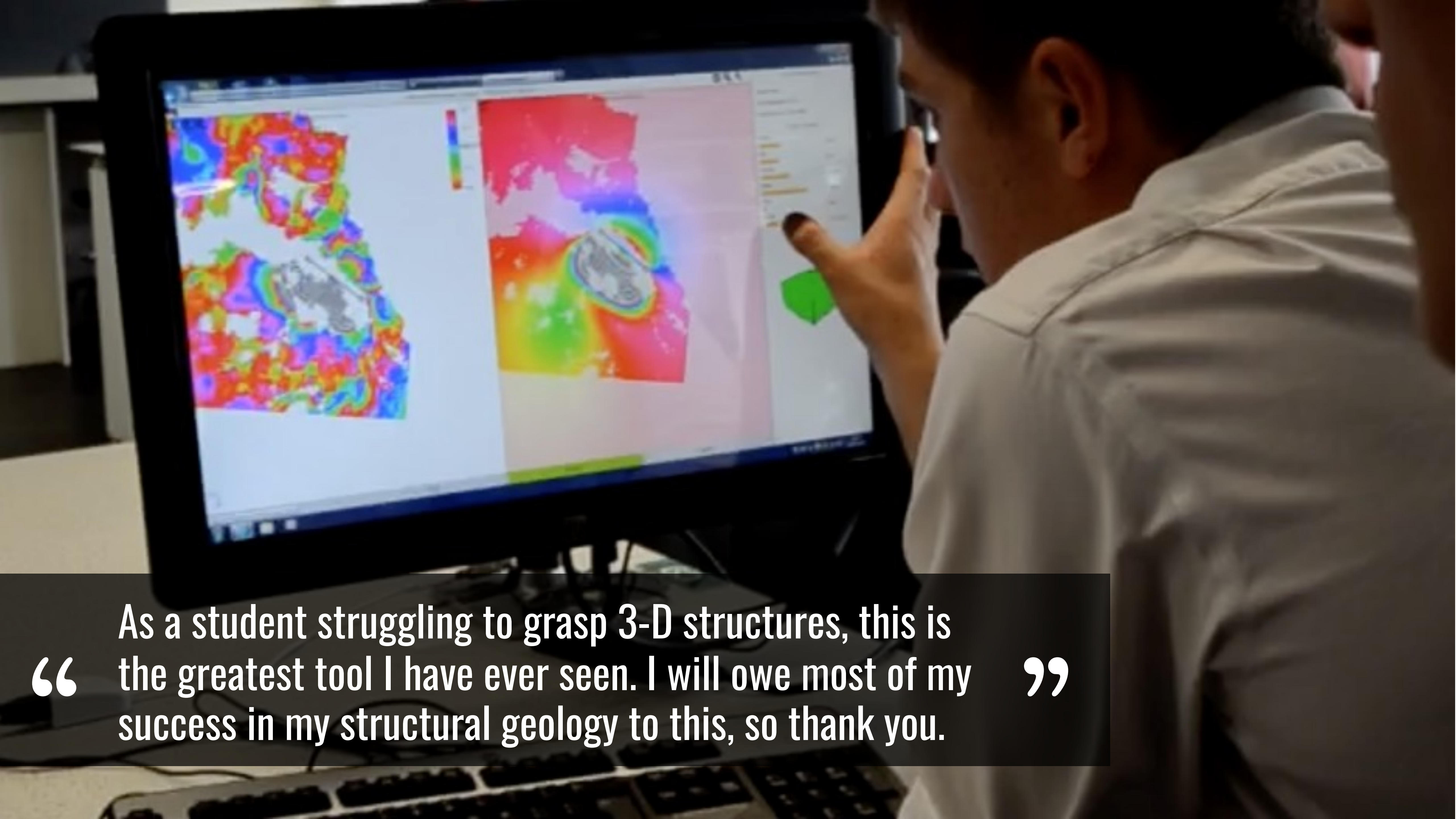
“ As a student struggling to grasp 3-D structures, this is the greatest tool I have ever seen. I will owe most of my success in my structural geology to this, so thank you. ”

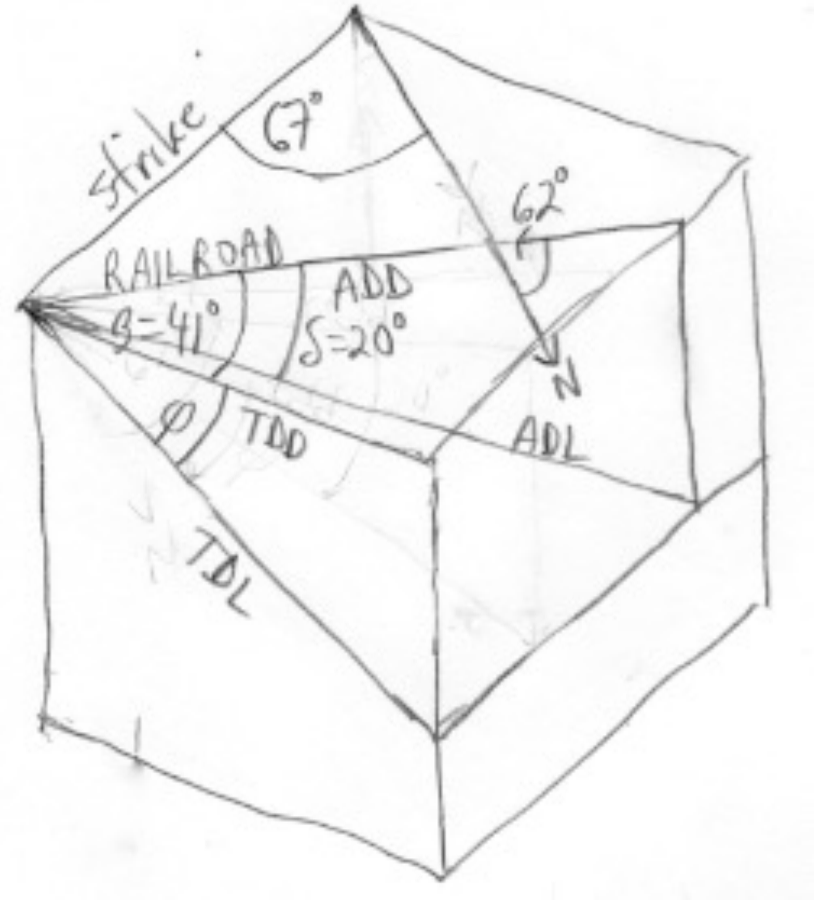
strike
67°
62°
RAILROAD
β=41°
ADD
δ=20°
N
φ
TDD
ADL
TDL

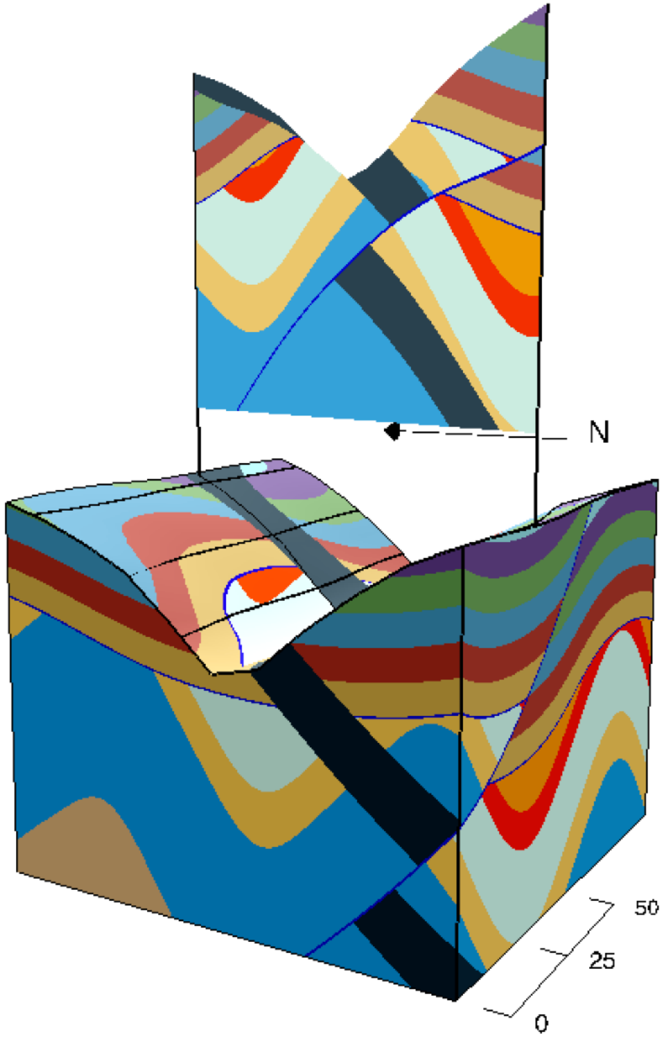
N
50
25
0

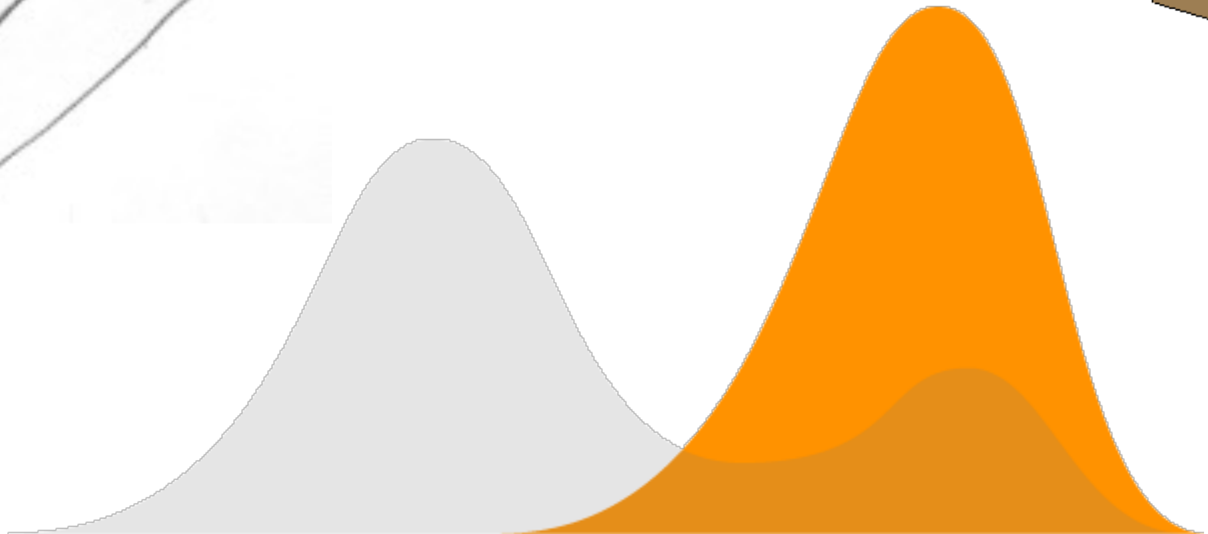

HYDROGEOLOGY

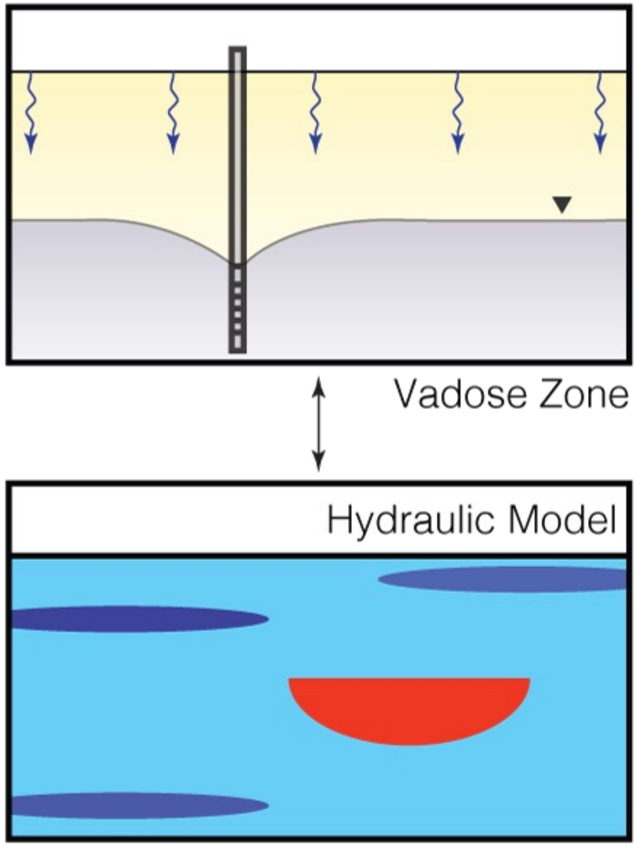

GEOPHYSICS

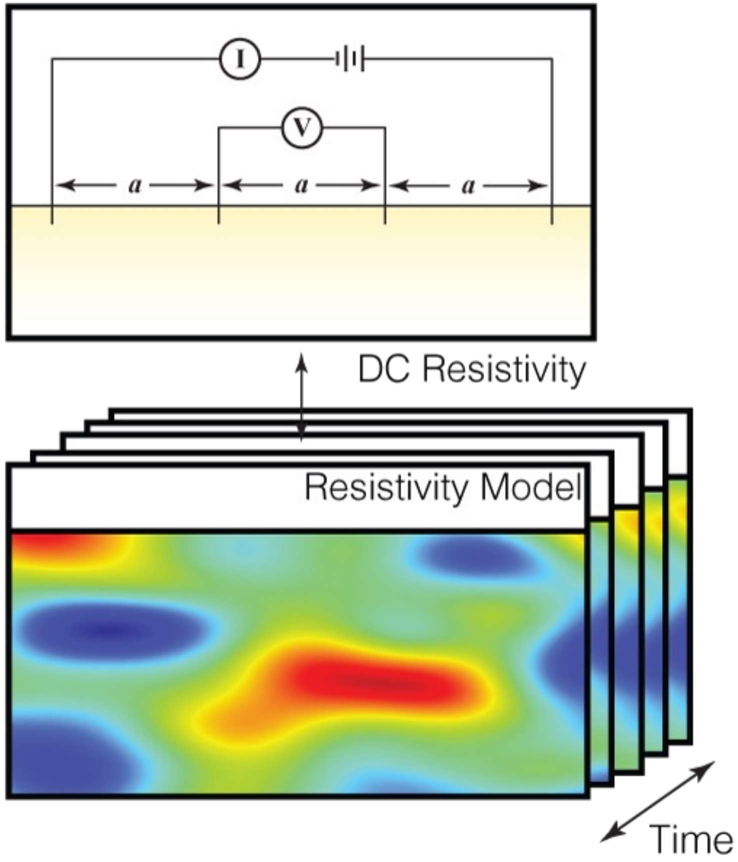

GEOLOGY

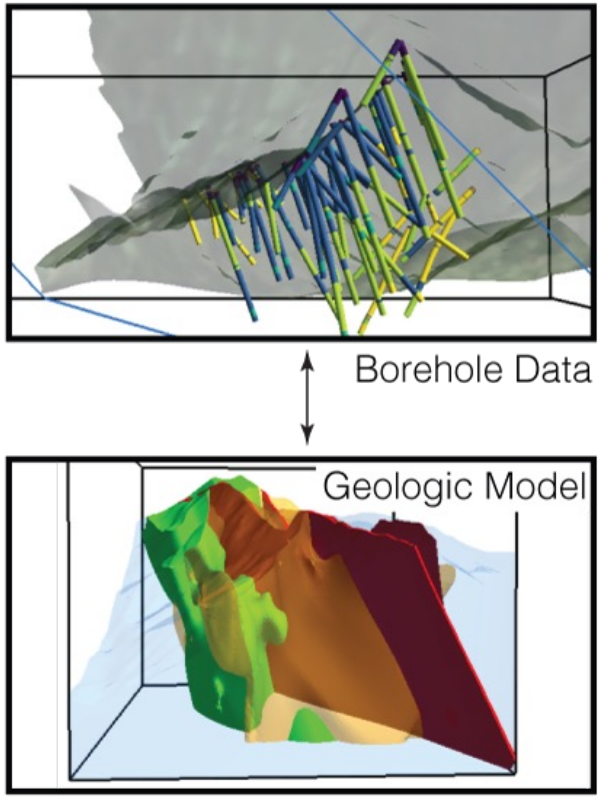

Data

Software

Story

Story

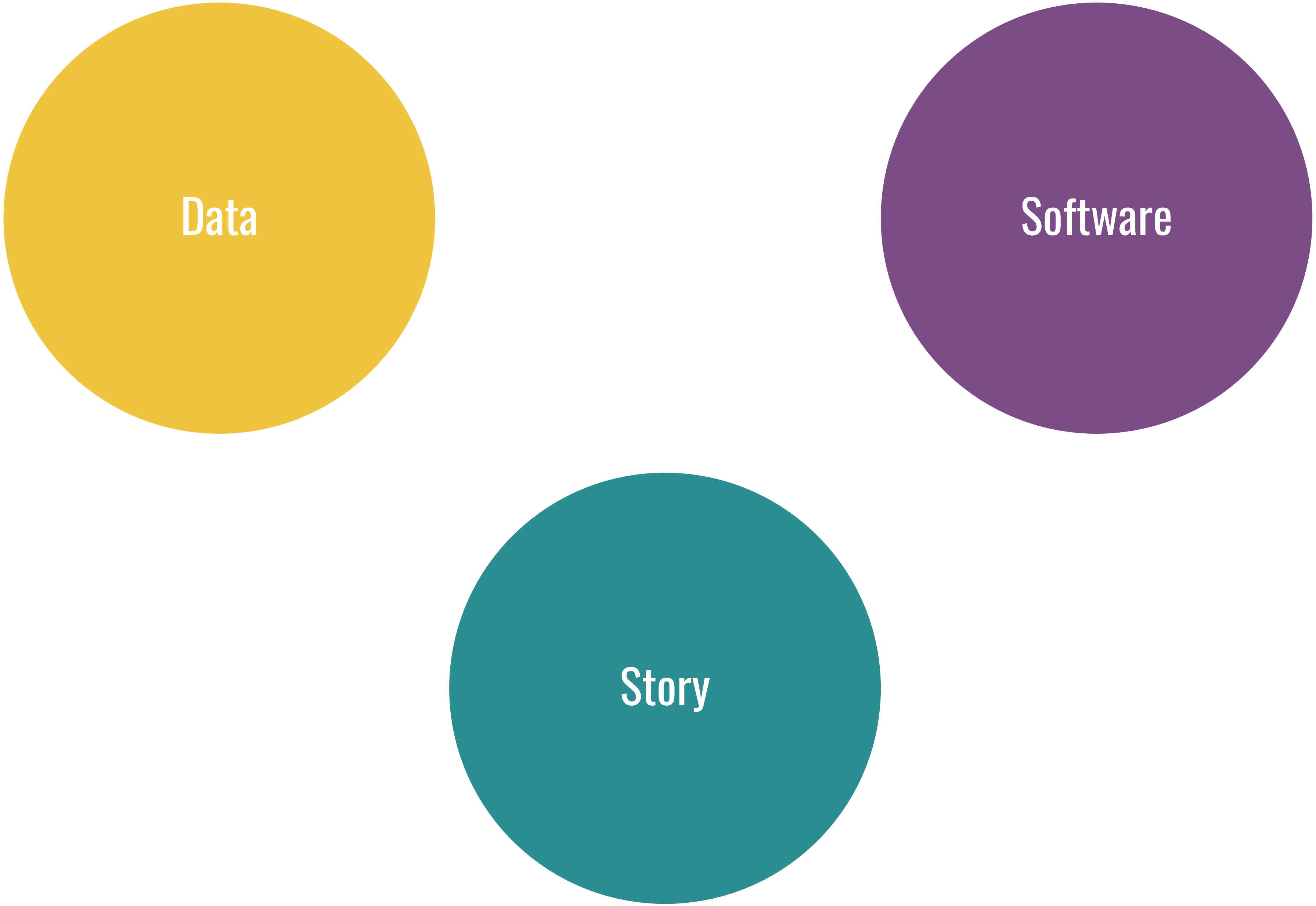
Data
Software
Story

Curvenote

Curvenote B I U S <> X₁ X¹ STOP EDITING SAVE VERSION SHARE

rowanc1 / hhmi-examples / clp1-mutations editing latest draft

Edit Subject

The Clp1 R140H mutation alters tRNA metabolism and mRNA 3′ processing in mouse models of pontocerebellar hypoplasia

Edit Subtitle

DOI: 10.1073/pnas.2110730118

AUTHOR	AFFILIATIONS
Caitlin E. Monaghan	Department of Cellular and Molecular Medicine, Division of Biological Sciences, Section of Neurobiology, University of California San Diego, La Jolla, CA 92093; HHMI, University of California San Diego, La Jolla, CA 92093;
Scott I. Adamson	The Jackson Laboratory for Genomic Medicine, Farmington, CT 06030; Department of Genetics and Genome Sciences, Institute for Systems Genomics, UConn Health, Farmington, CT 06030
Mridu Kapur	Department of Cellular and Molecular Medicine, Division of Biological Sciences, Section of Neurobiology, University of California

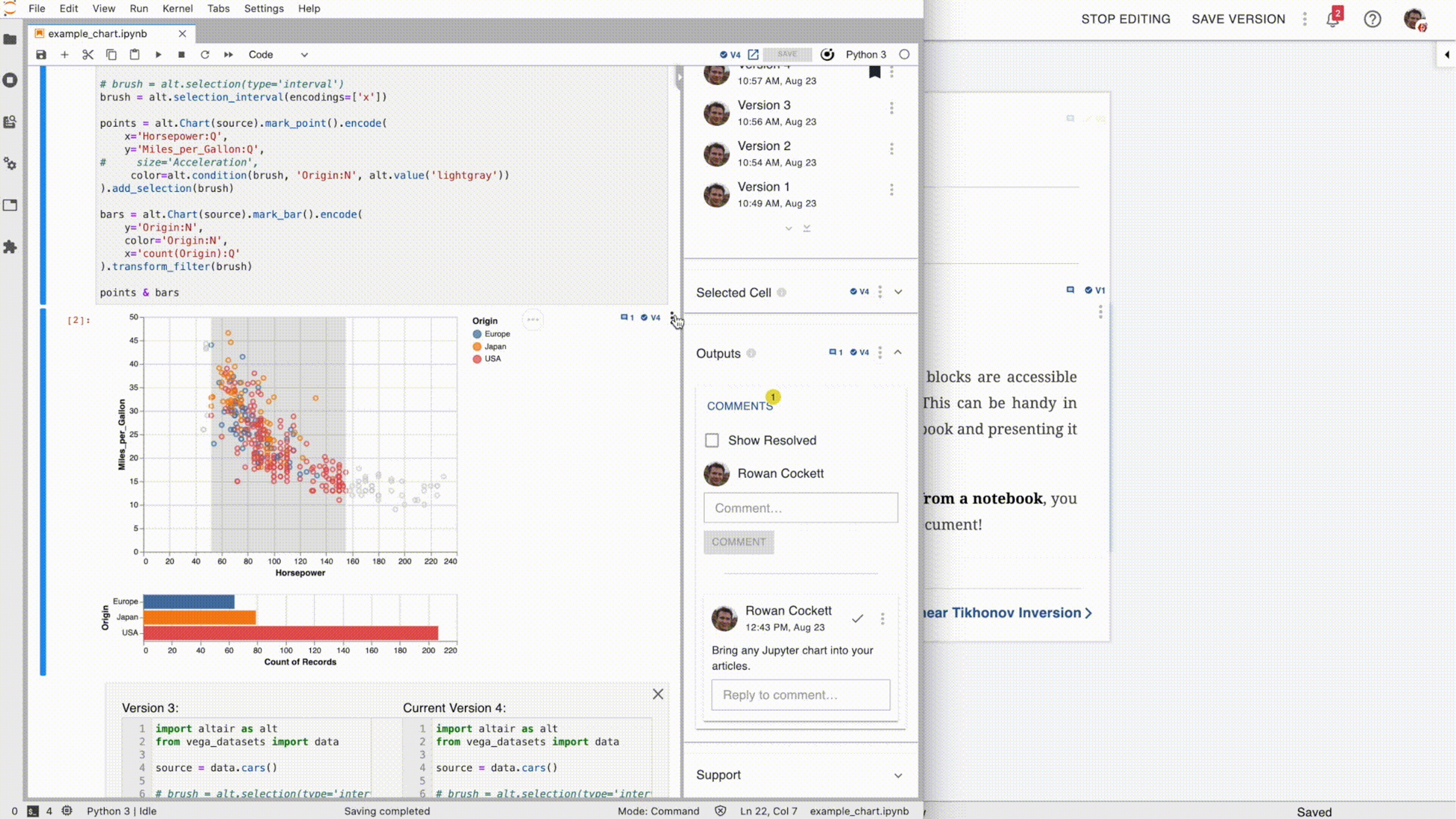
File Edit View Run Kernel Tabs Settings Help
example_chart.ipynb
Code
V4 SAVE Python 3
STOP EDITING SAVE VERSION
# brush = alt.selection(type='interval')
brush = alt.selection_interval(encodings=['x'])
points = alt.Chart(source).mark_point().encode(
x='Horsepower:Q',
y='Miles_per_Gallon:Q',
# size='Acceleration',
color=alt.condition(brush, 'Origin:N', alt.value('lightgray'))
).add_selection(brush)
bars = alt.Chart(source).mark_bar().encode(
y='Origin:N',
color='Origin:N',
x='count(Origin):Q'
).transform_filter(brush)
points & bars
[2]:
Origin
Europe
Japan
USA
Miles_per_Gallon
Horsepower
Origin
Count of Records
Version 3:
Current Version 4:
import altair as alt
from vega_datasets import data
source = data.cars()
# brush = alt.selection(type='inter
Version 3
10:56 AM, Aug 23
Version 2
10:54 AM, Aug 23
Version 1
10:49 AM, Aug 23
10:57 AM, Aug 23
Selected Cell
Outputs
COMMENTS
Show Resolved
Rowan Cockett
Comment...
COMMENT
Rowan Cockett
12:43 PM, Aug 23
Bring any Jupyter chart into your articles.
Reply to comment...
Support
blocks are accessible
This can be handy in
ook and presenting it
rom a notebook, you
cument!
near Tikhonov Inversion
Python 3 | Idle
Saving completed
Mode: Command
Ln 22, Col 7
example_chart.ipynb
Saved

RESEARCH ARTICLE AGU NOTEBOOKS NOW Volume 8, Issue 11

VESIcal: An open-source thermodynamic model engine for mixed volatile (H_2O-CO_2) solubility in silicate melts

Kayla Iacovino, Simon Matthews, Penny Wieser, Gordon M. Moore, Florence Bégué

September 13, 2021 · https://doi.org/10.1029/2020EA001584

Download PDF
Download TEX
Open in Binder

Abstract

Thermodynamics has been fundamental to the interpretation of geologic data and modeling of geologic systems for decades. However, more recent advancements in computational capabilities and a marked increase in researchers' accessibility to computing tools has outpaced the functionality and extensibility of currently available modeling tools. Here we present VESIcal (Volatile Equilibria and Saturation Identification calculator): the first comprehensive modeling tool for H_2O, CO_2, and mixed (H_2O-CO_2) solubility in silicate melts that: **a)** allows users access to seven of the most popular models, plus easy inter-comparison between models; **b)** provides universal functionality for all models (e.g., functions for calculating saturation pressures, degassing paths, etc.); **c)** can process large datasets (1,000's of samples) automatically; **d)** can output computed data into an Excel spreadsheet or CSV file for simple post-modeling analysis; **e)** integrates plotting

IN THIS ARTICLE

Curvenote

{MyST}

ALFRED P. SLOAN
FOUNDATION

{MyST}

14,318 books

13%-15% of Python docs

jupyter

Many, many contributors

mystmd.org

ALFRED P. SLOAN FOUNDATION

Write Once

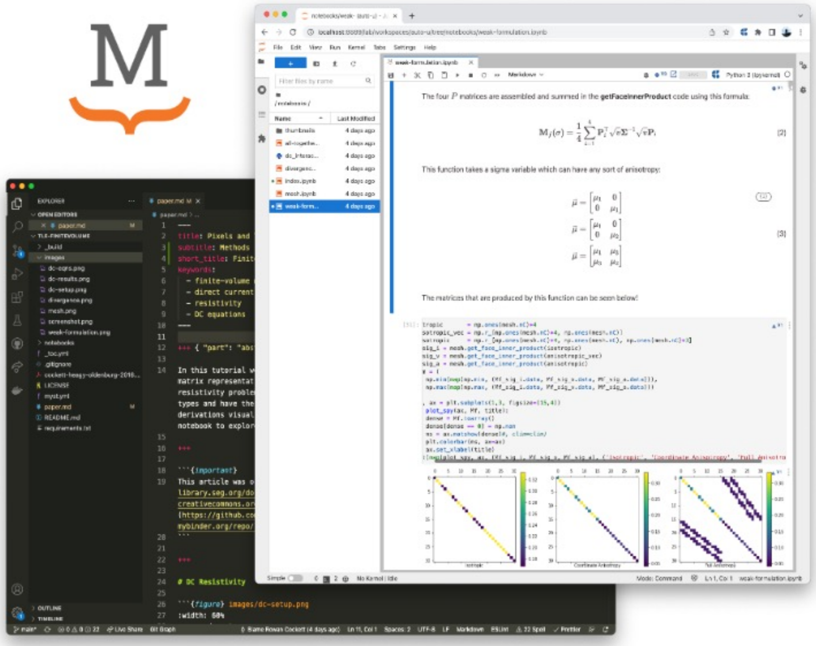

MyST Markdown & Notebooks

Export to any Template

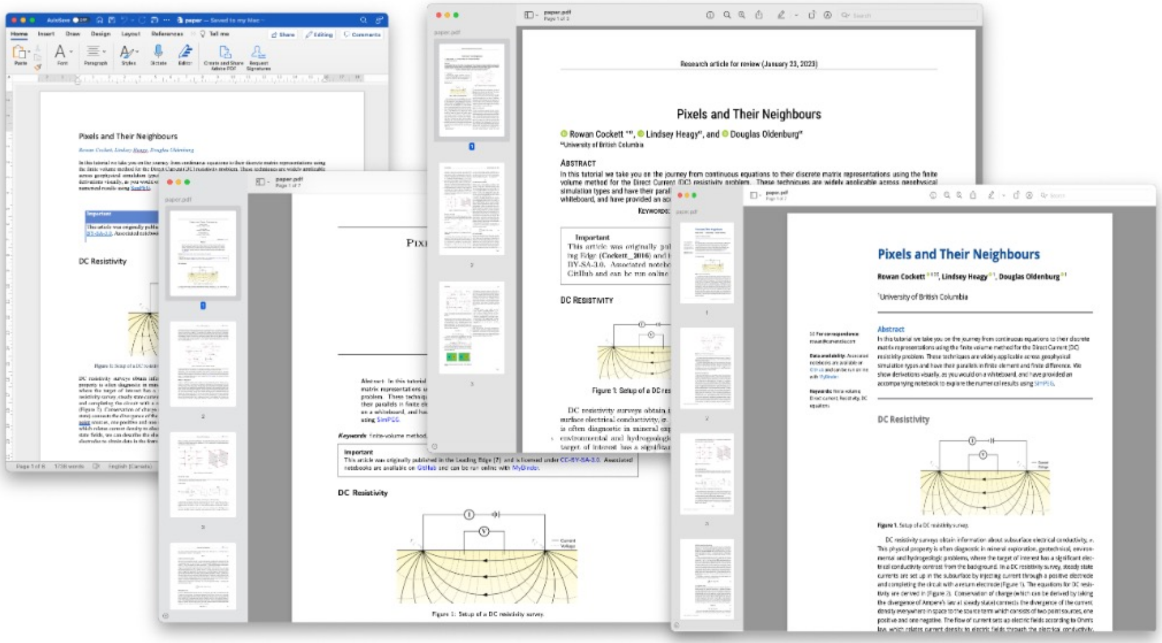

PDF + Word + LaTeX

Write Once

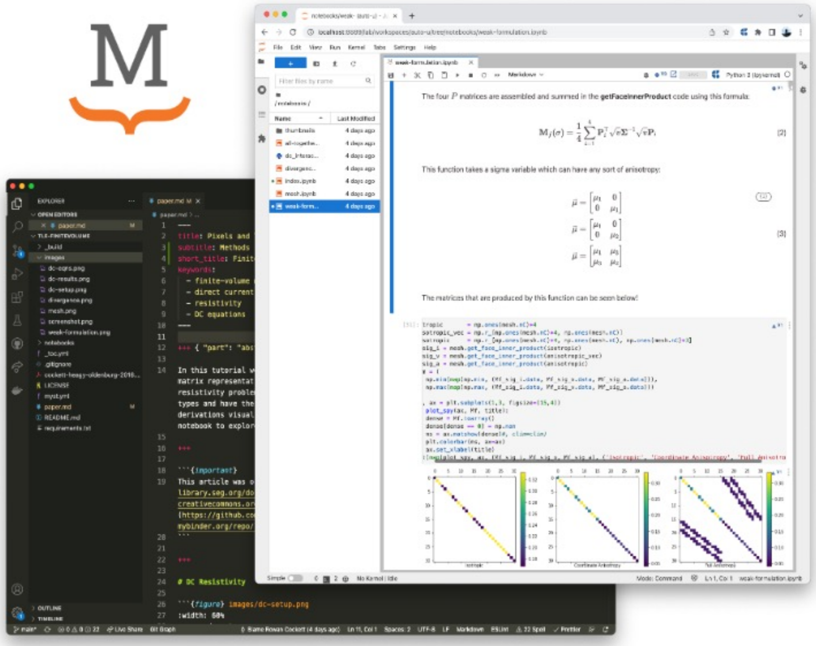

MyST Markdown & Notebooks

Websites

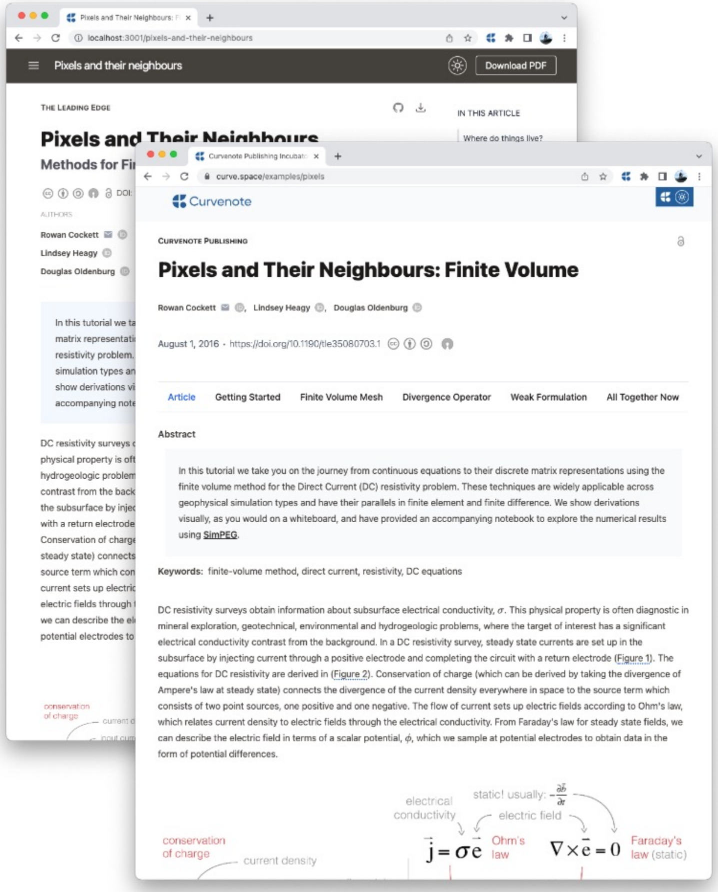

Write Once

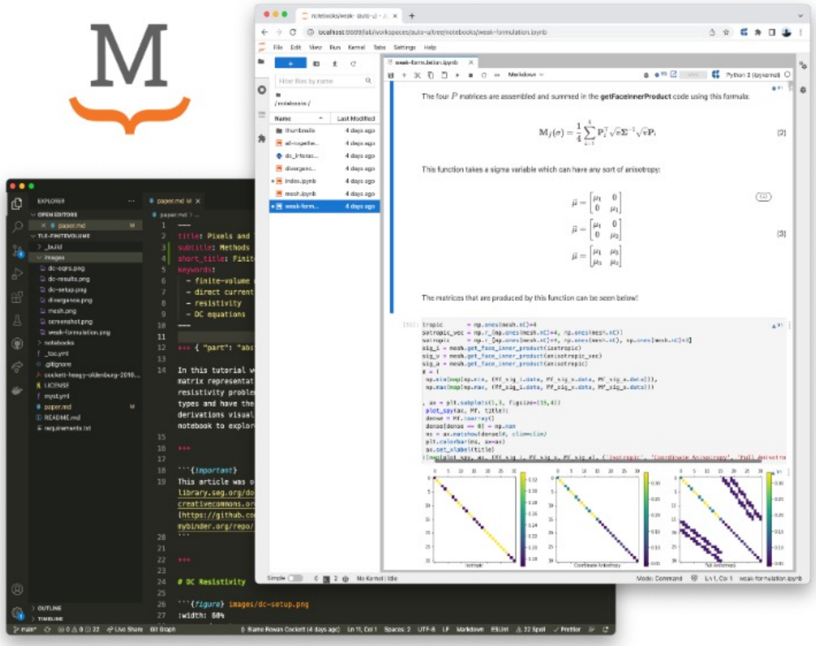

MyST Markdown & Notebooks

Structured Content

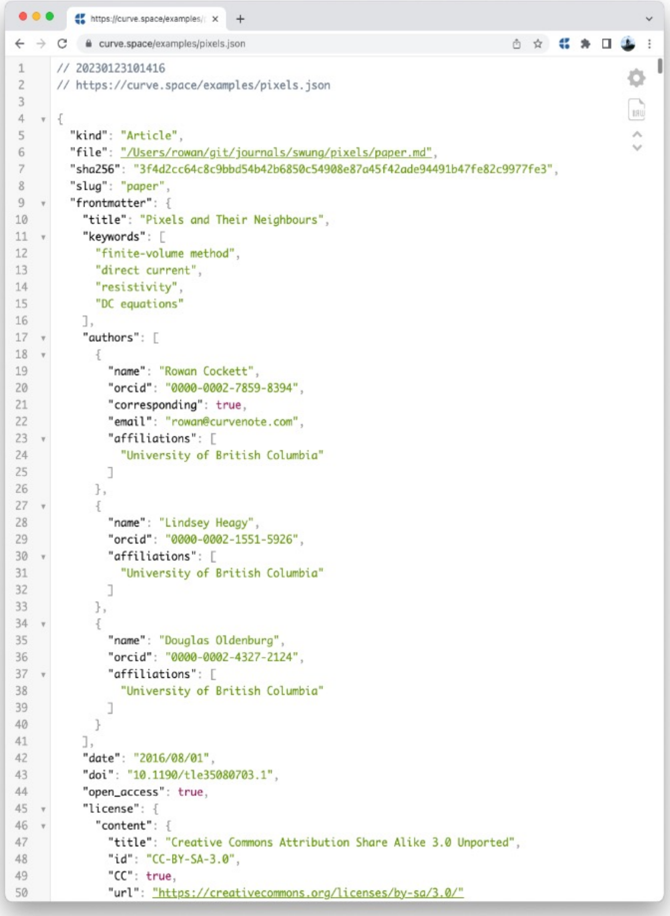

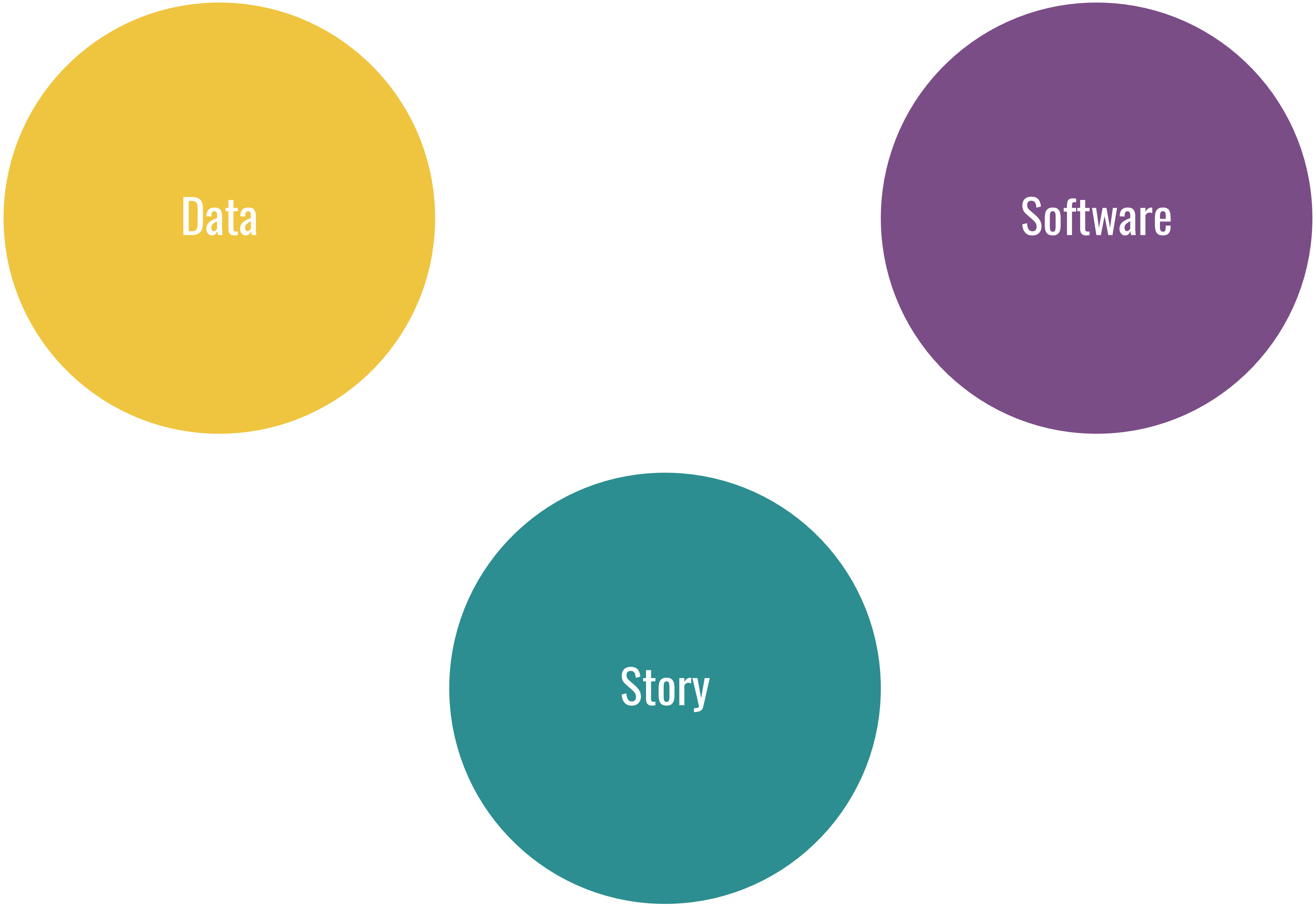

Data
Software
Story

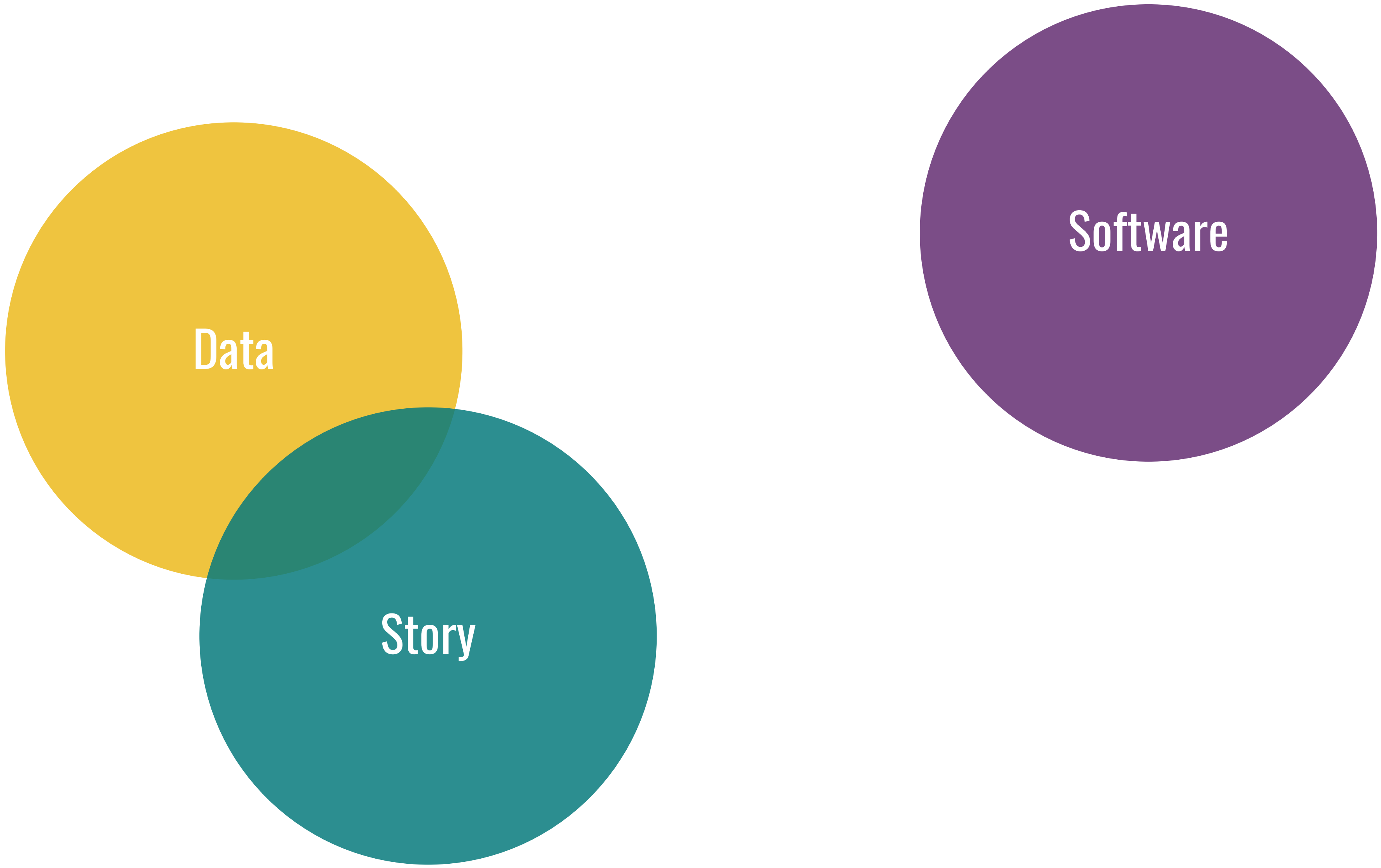
Data
Story
Software

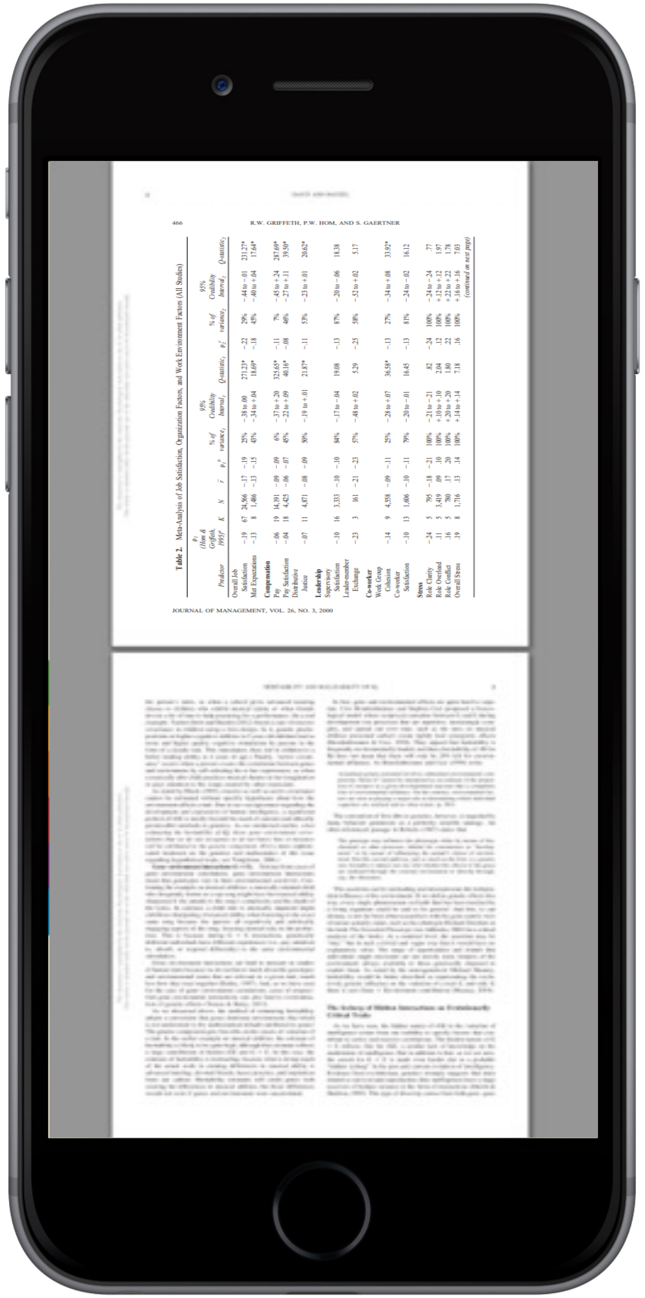

Data

Story

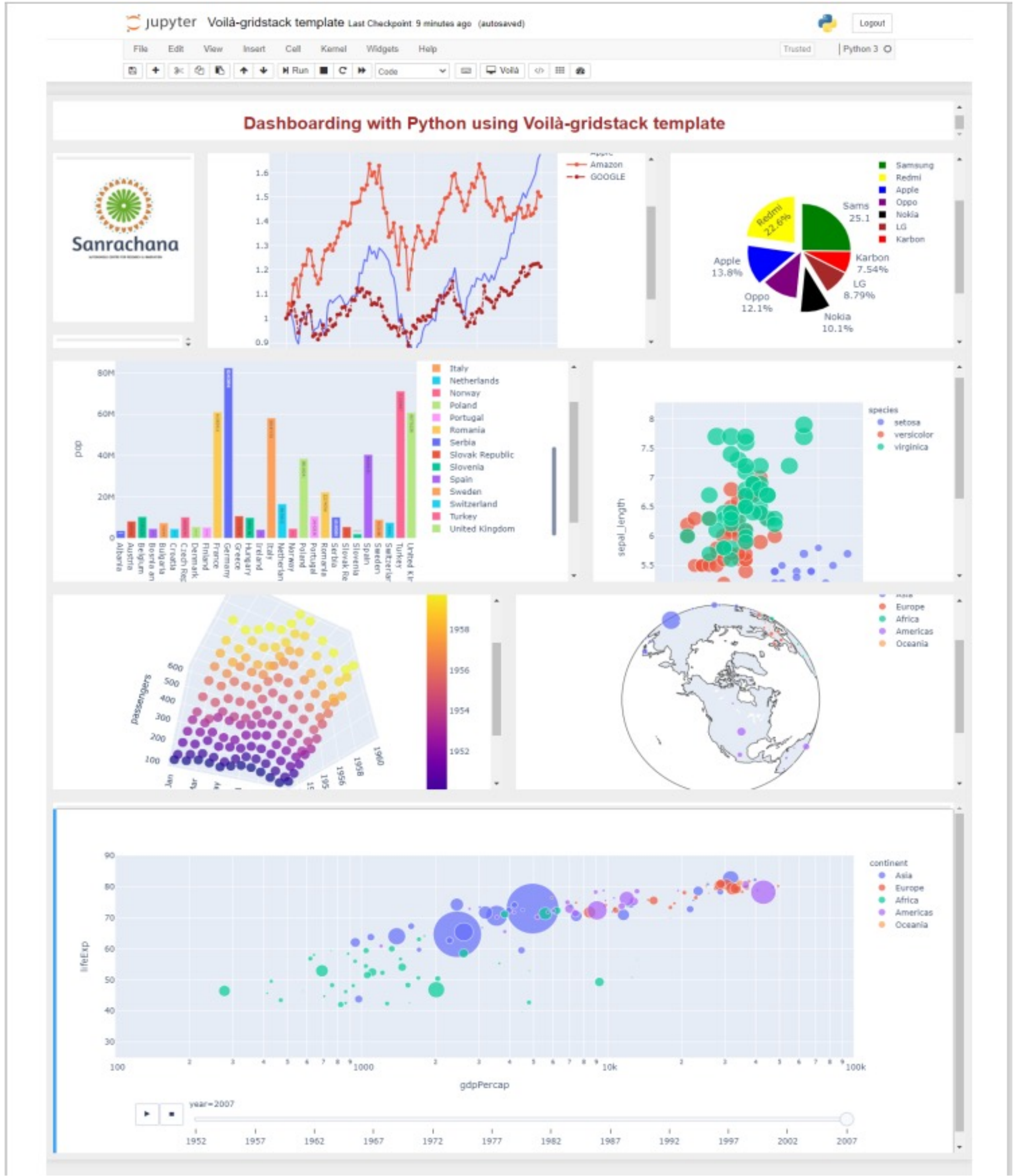

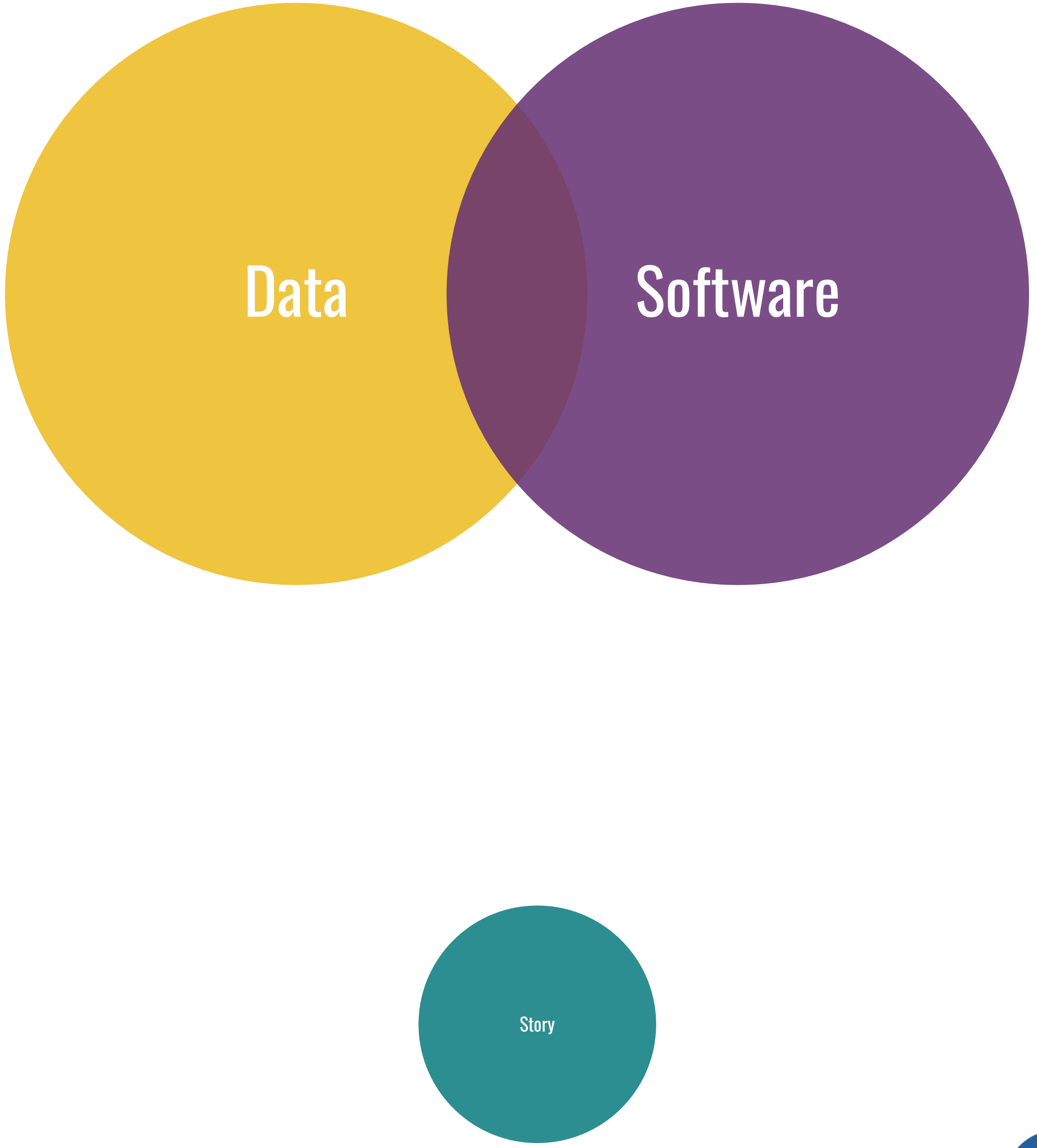

(Sanrachna Foundation, 2021)

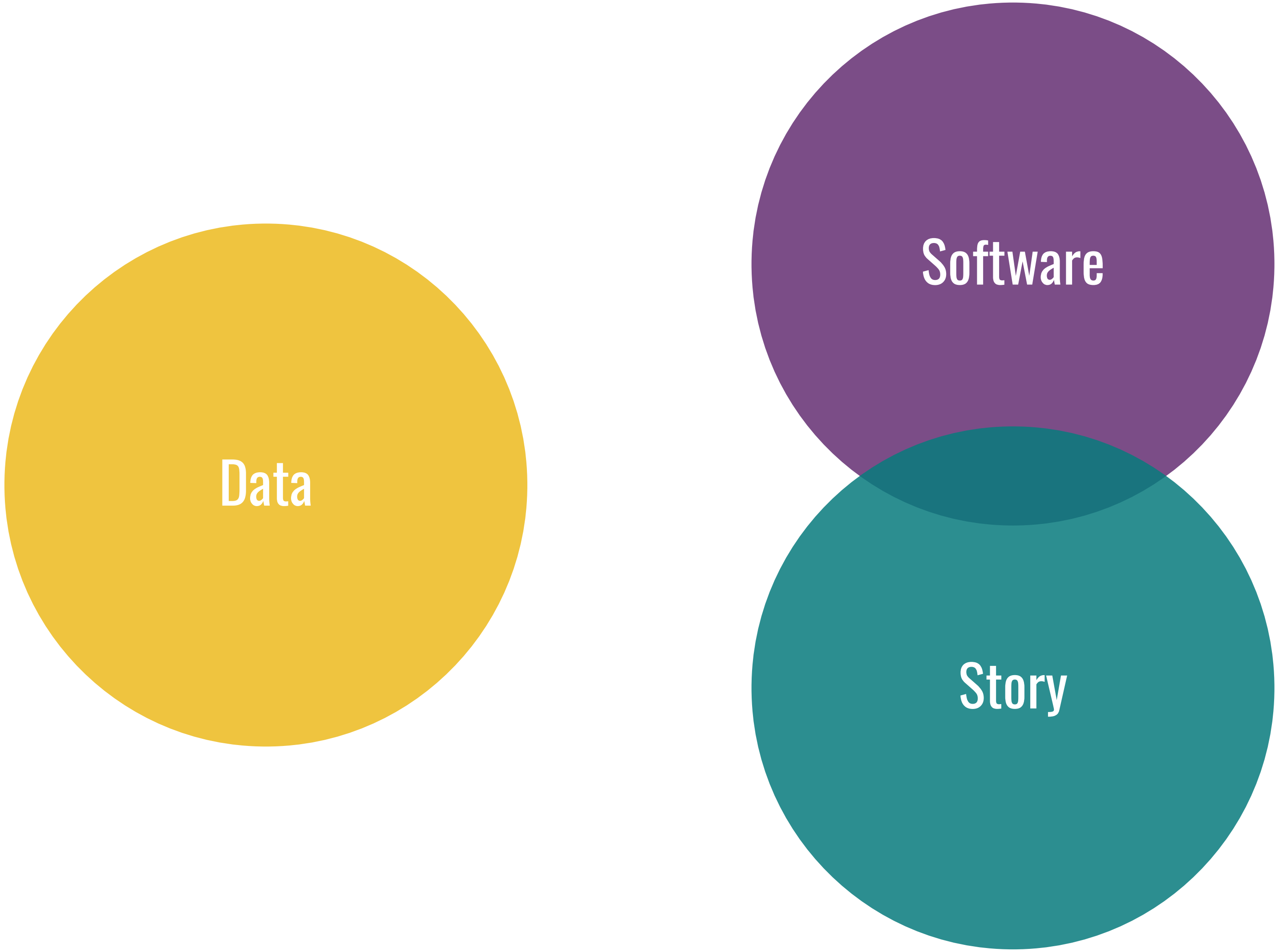
Data
Software
Story

Meta's Data

Software

Story

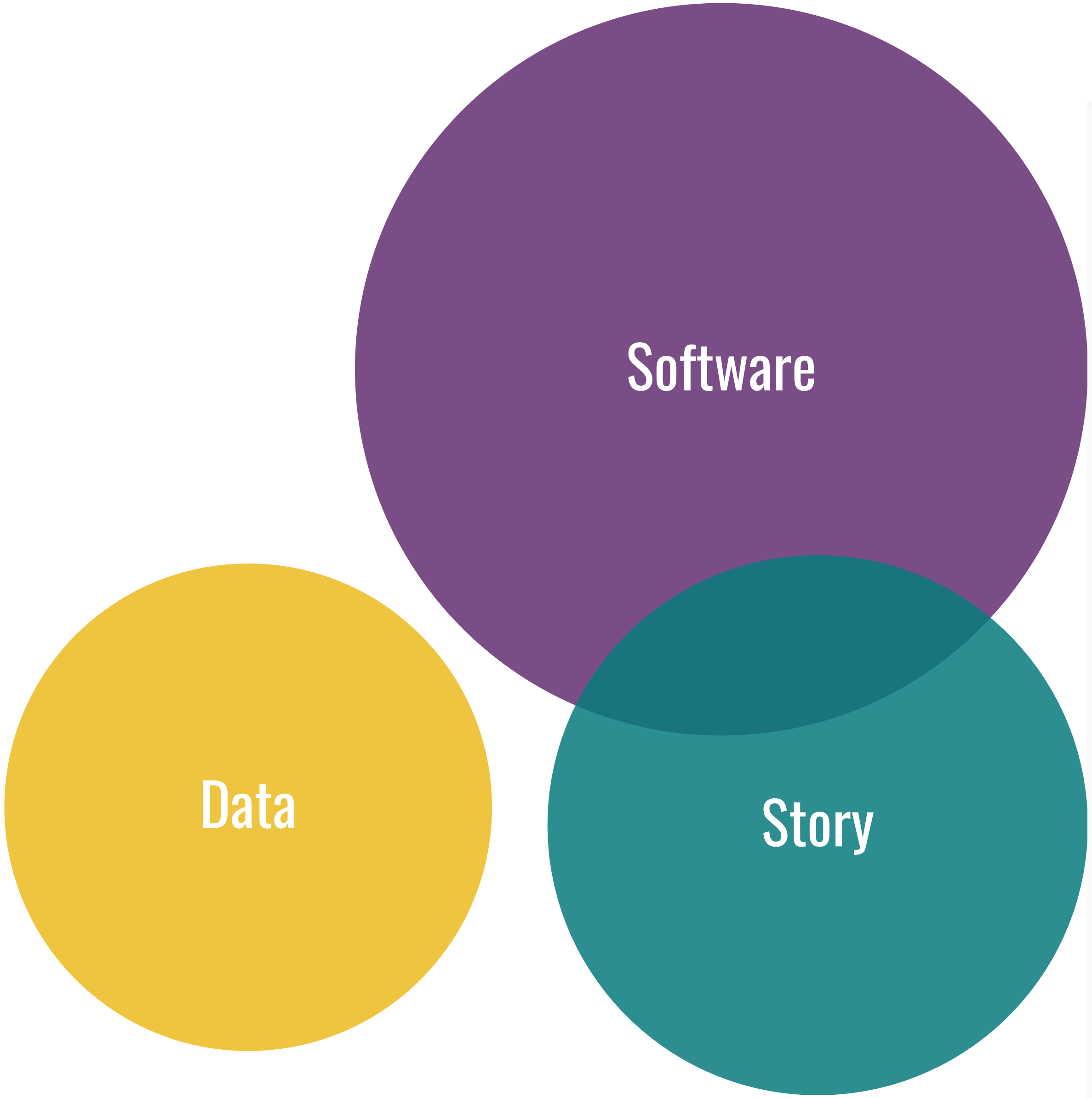
Software
Data
Story

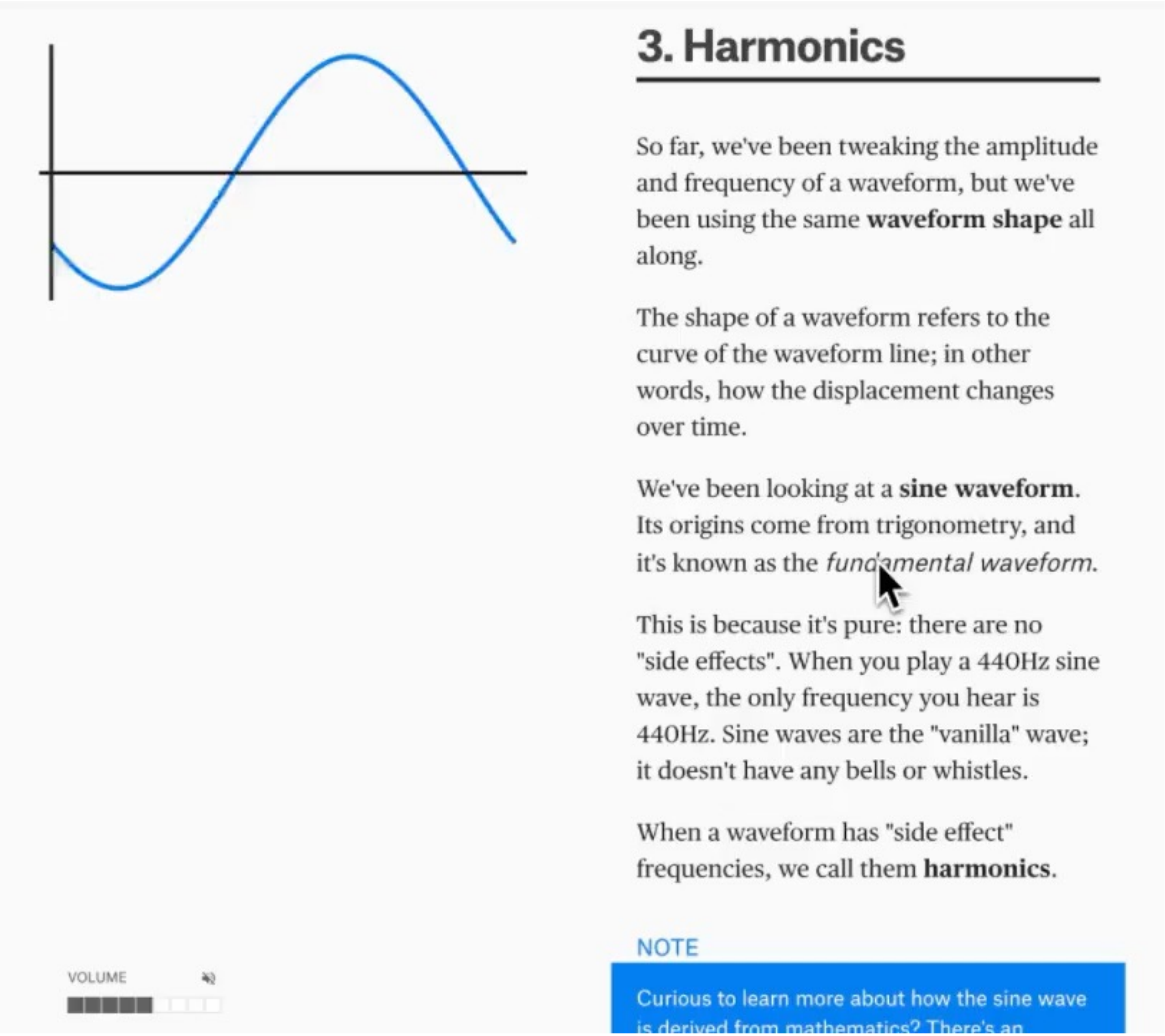
3. Harmonics
So far, we've been tweaking the amplitude and frequency of a waveform, but we've been using the same **waveform shape** all along.
The shape of a waveform refers to the curve of the waveform line; in other words, how the displacement changes over time.
We've been looking at a **sine waveform**. Its origins come from trigonometry, and it's known as the *fundamental waveform*.
This is because it's pure: there are no "side effects". When you play a 440Hz sine wave, the only frequency you hear is 440Hz. Sine waves are the "vanilla" wave; it doesn't have any bells or whistles.
When a waveform has "side effect" frequencies, we call them **harmonics**.
NOTE
Curious to learn more about how the sine wave
VOLUME

(The Pudding)

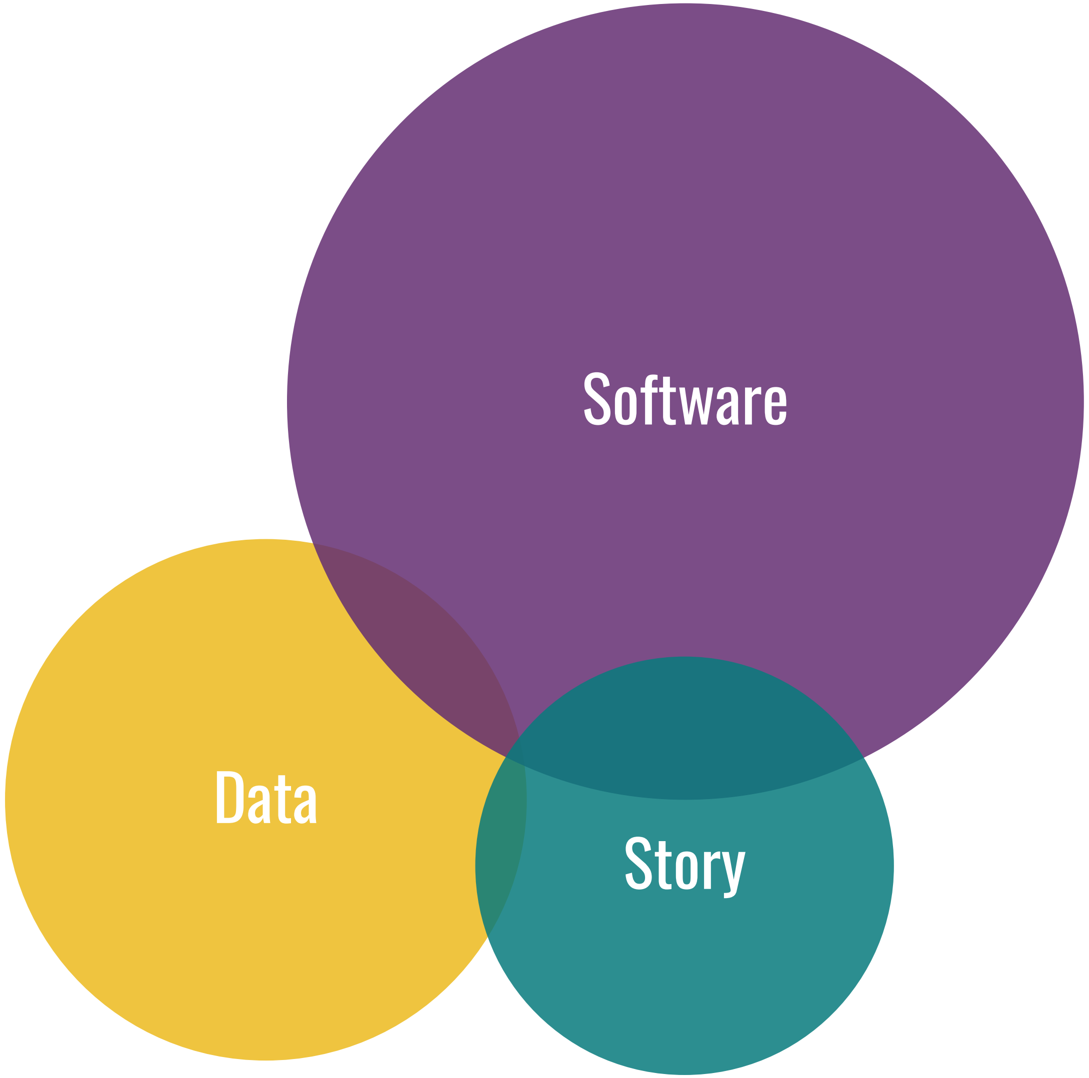
Software
Data
Story

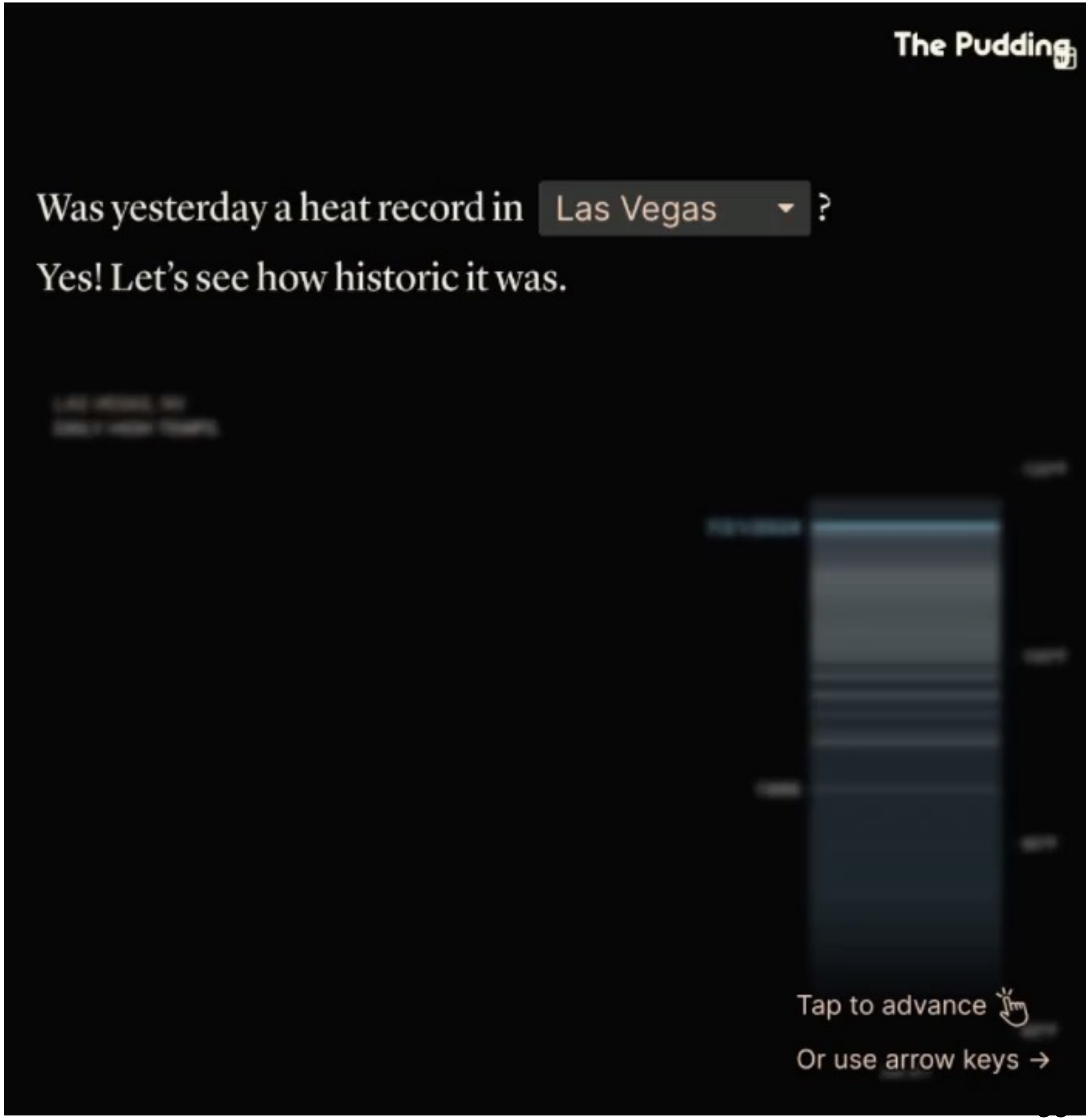
The Pudding
Was yesterday a heat record in Las Vegas ?
Yes! Let's see how historic it was.
Tap to advance
Or use arrow keys →

(The Pudding)

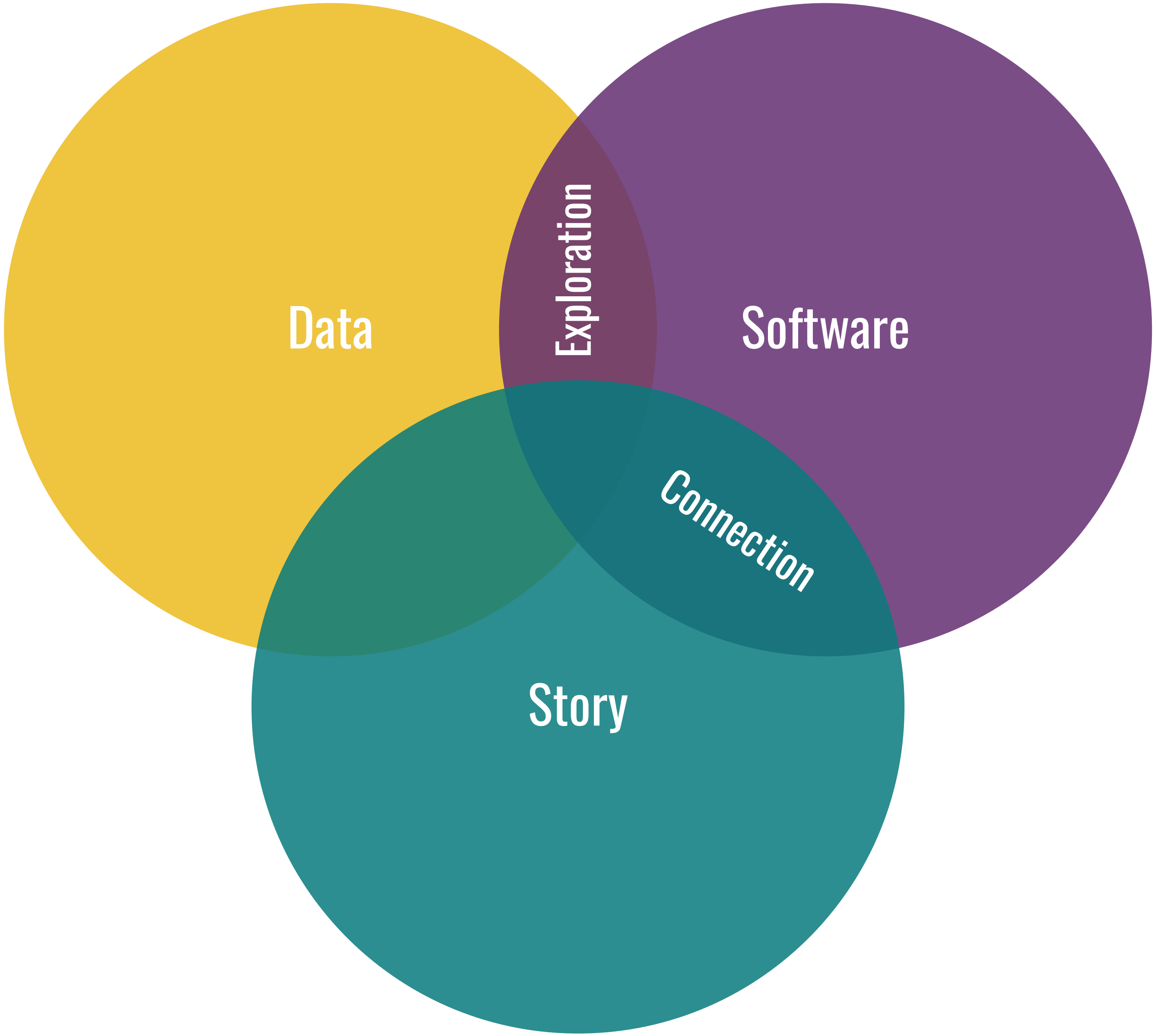
Data
Exploration
Software
Connection
Story

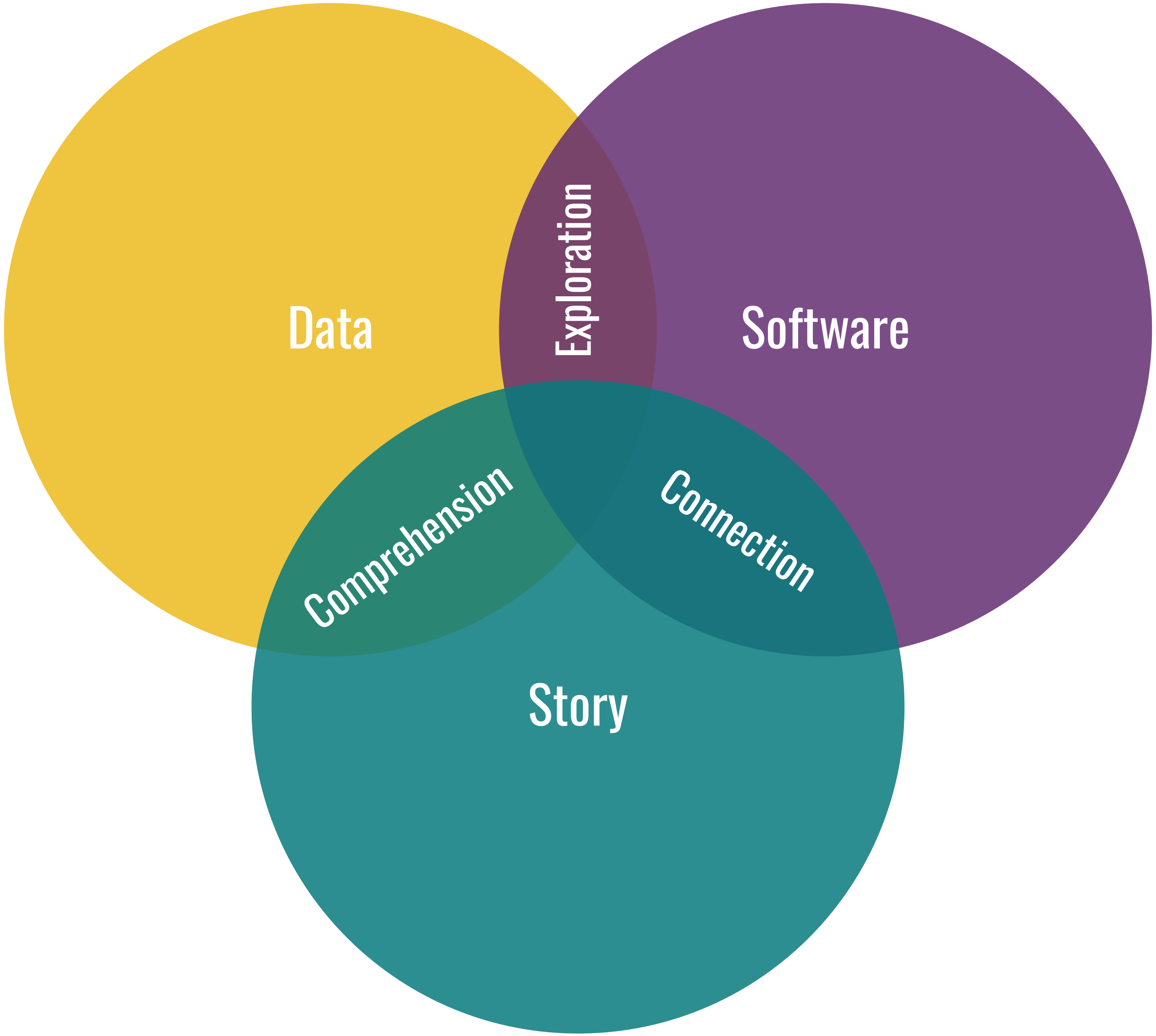
Data
Exploration
Software
Comprehension
Connection
Story

LEARNING & DISCOVERY

RESEARCH PUBLISH

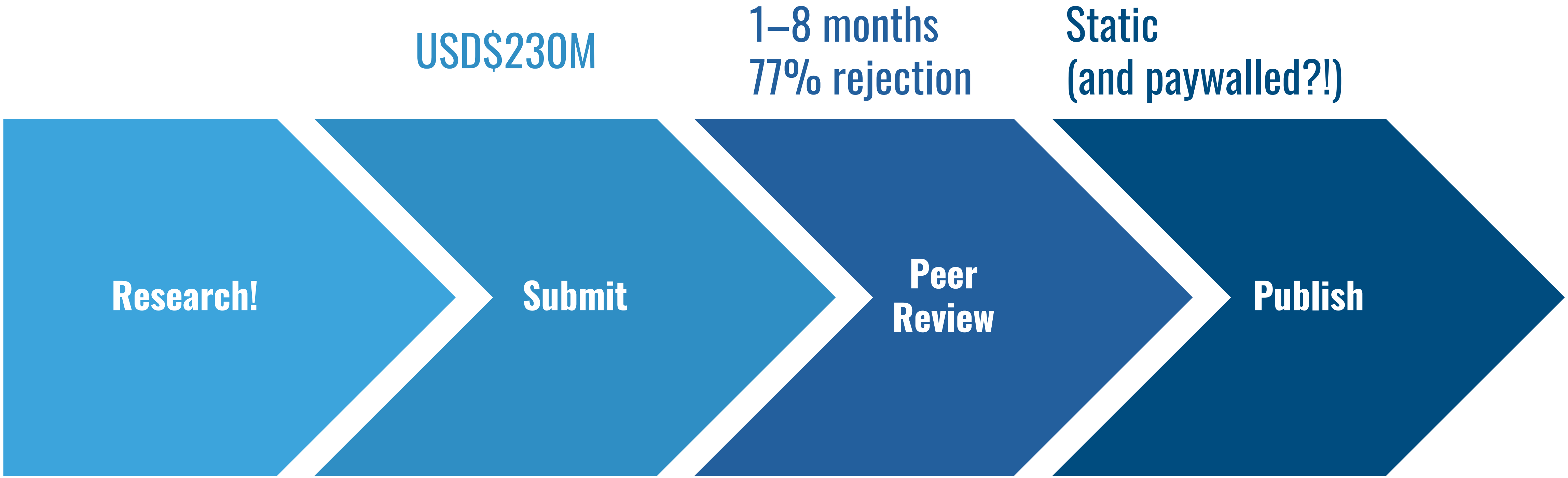
USD$230M
1–8 months
77% rejection
Static
(and paywalled?!)
Research!
Submit
Peer Review
Publish

Research!

Publish

Research!

MANUAL

CLOSED

INACCESSIBLE

Publish

Research!

AUTOMATED

OPEN

ACCESSIBLE

Publish

SOFTWARE DEVELOPMENT

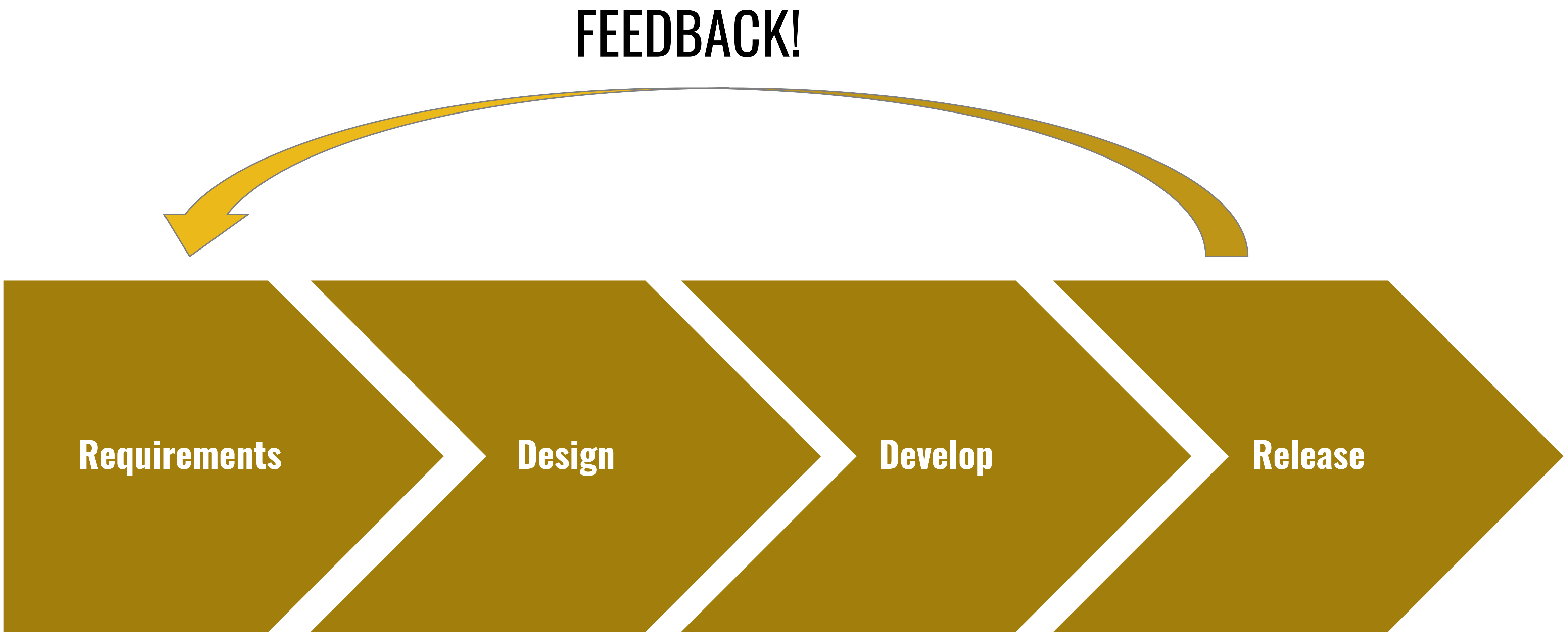
FEEDBACK!
Requirements
Design
Develop
Release

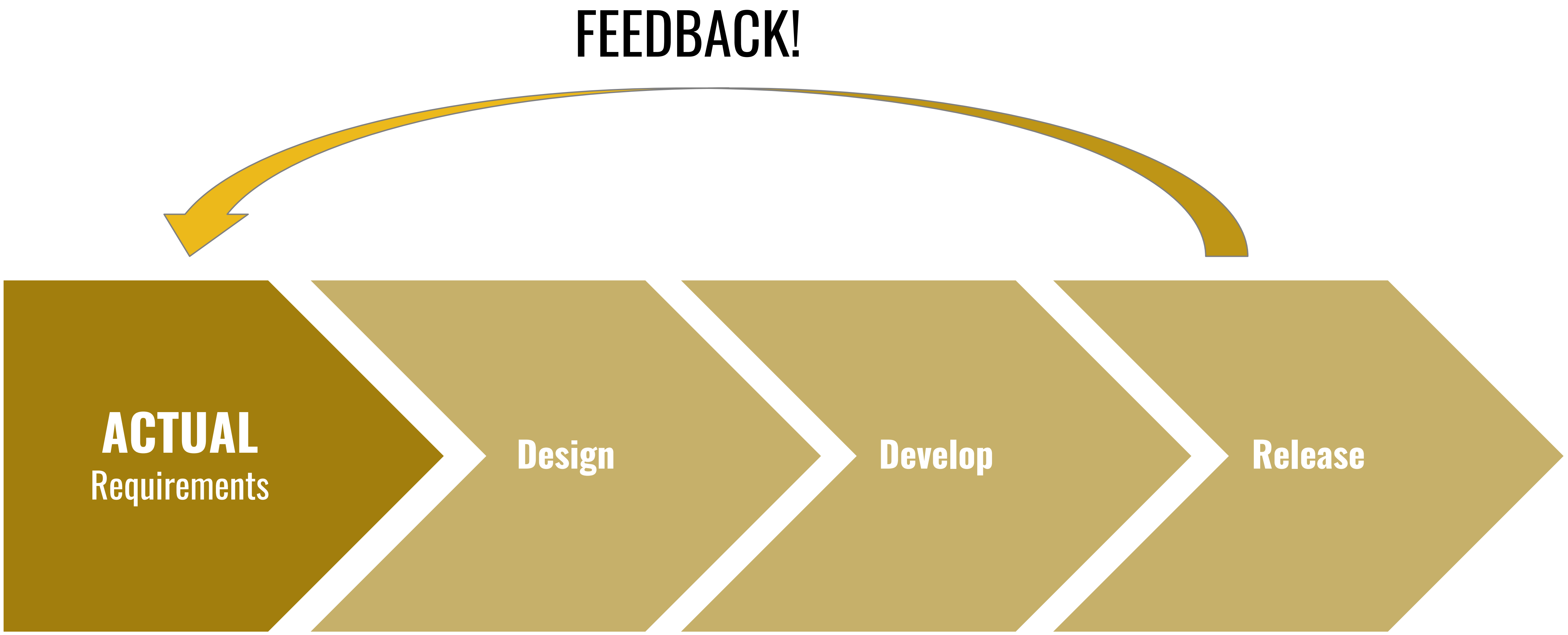

WATERFALL DEVELOPMENT

WATERFALL DEVELOPMENT

↓

CONTINUOUS DEVELOPMENT

CONTINUOUS DEVELOPMENT

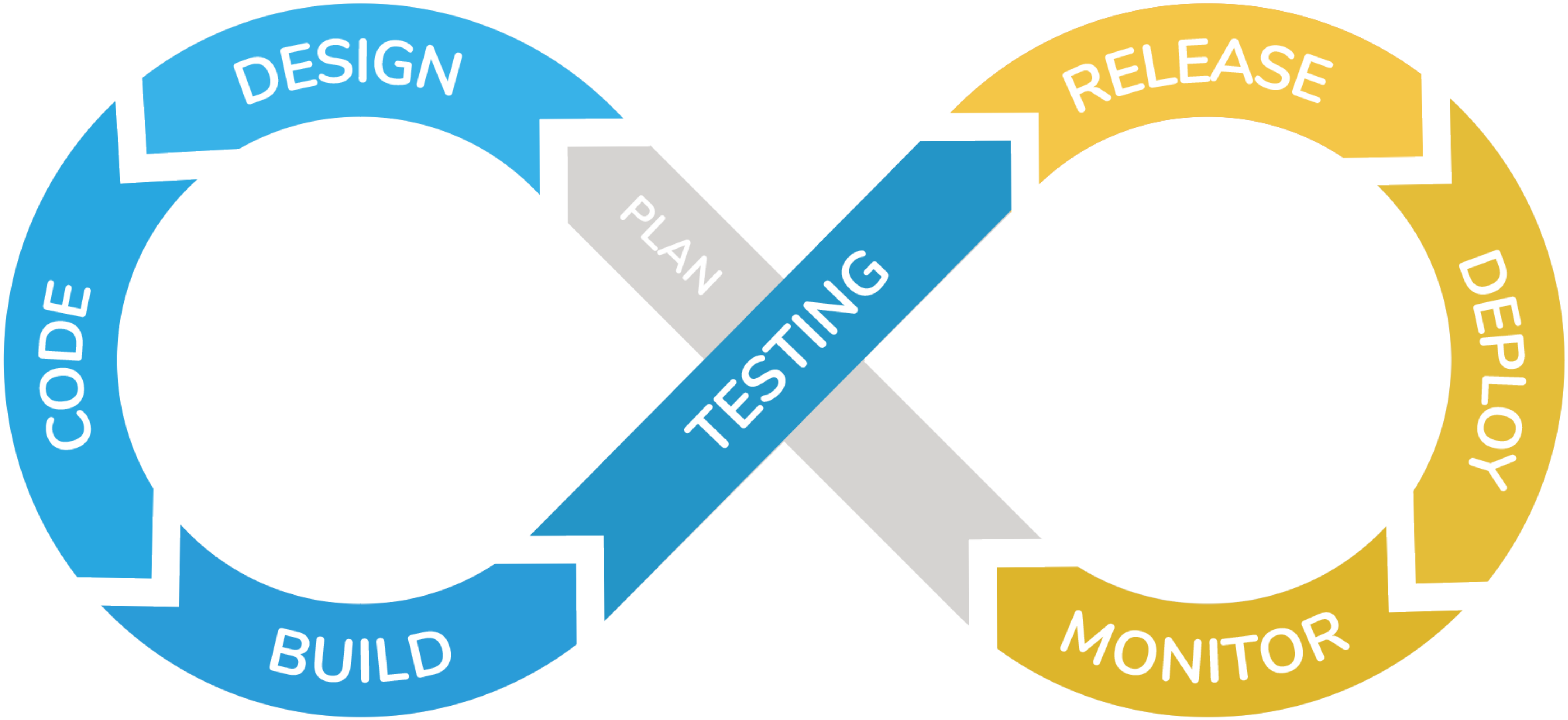

CONTINUOUS DEVELOPMENT

CONTINUOUS DEVELOPMENT

46x

DORA, 2019

7x

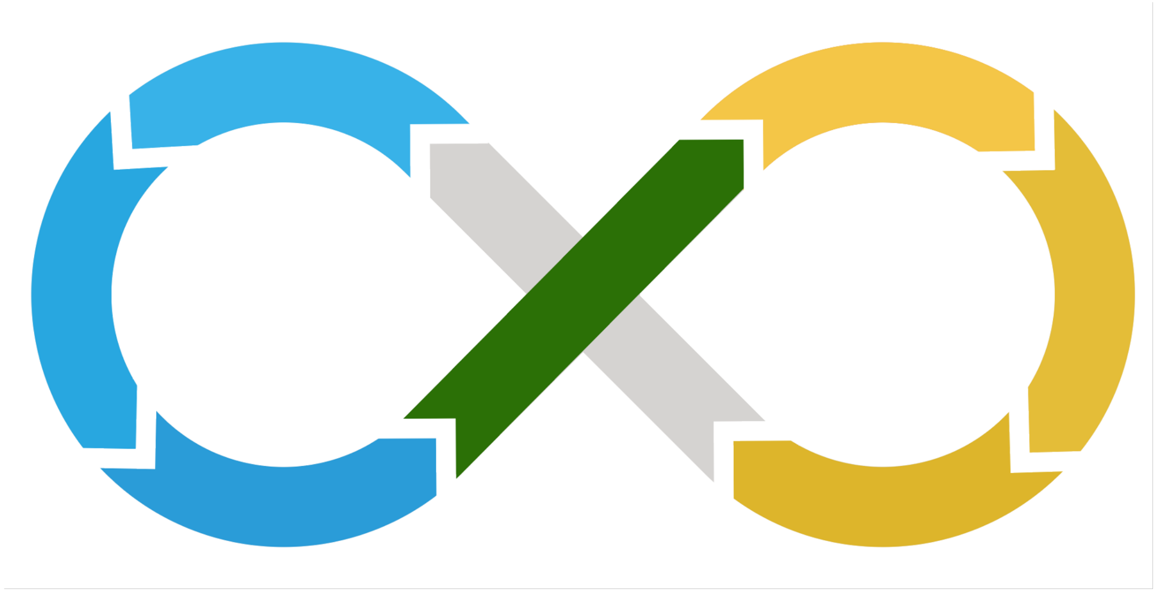

DORA, 2019


Research!
Publish

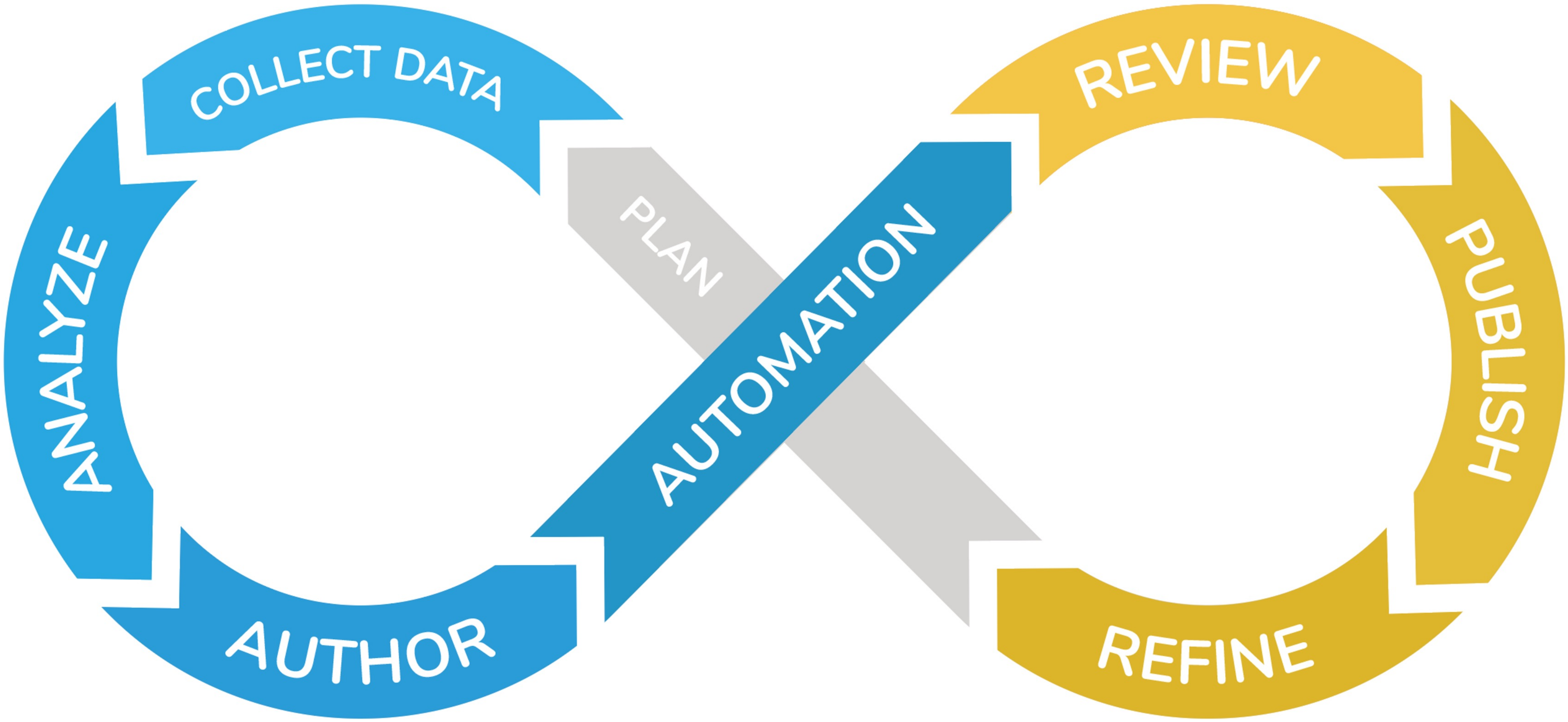

CONTINUOUS SCIENCE

CONTINUOUS SCIENCE

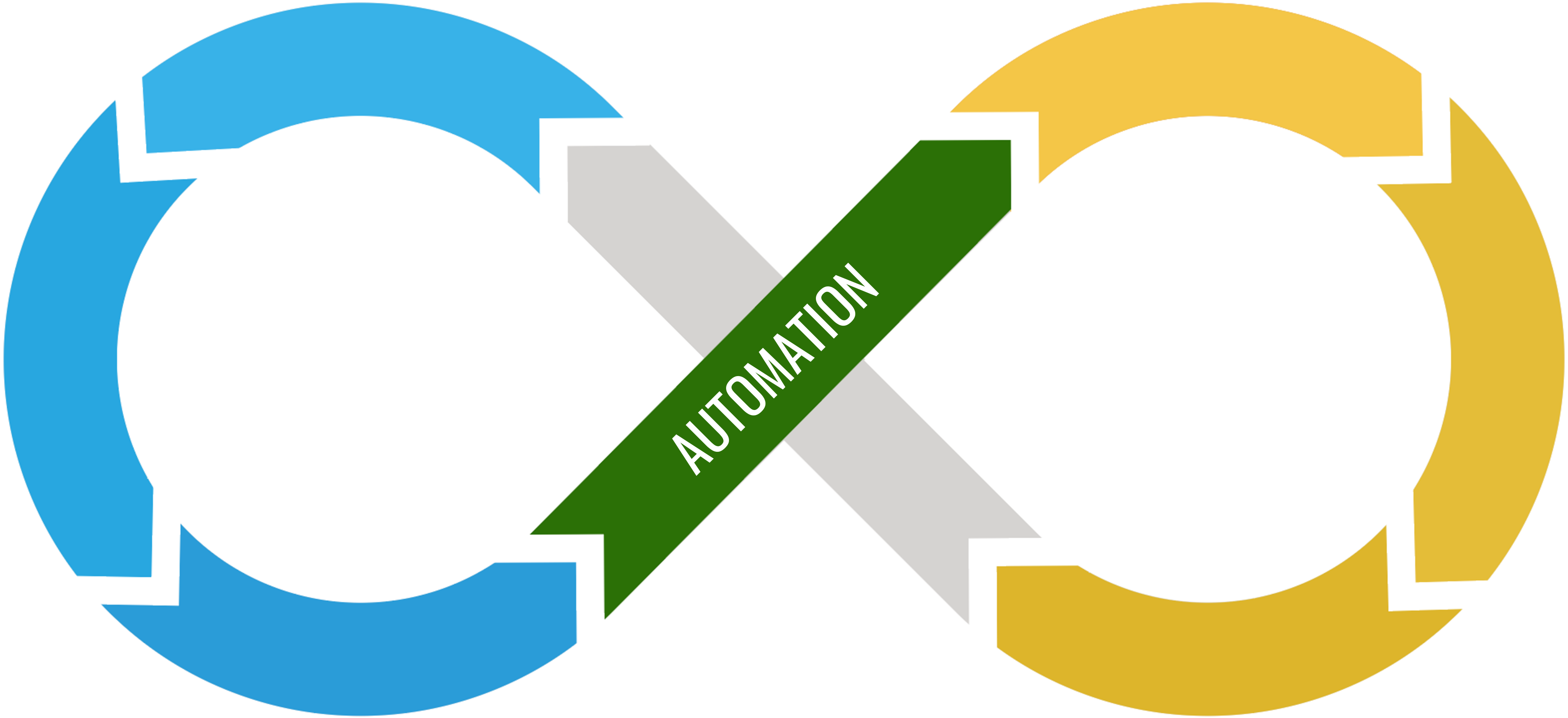

CONTINUOUS SCIENCE

CONTINUOUS SCIENCE

CONTINUOUS SCIENCE

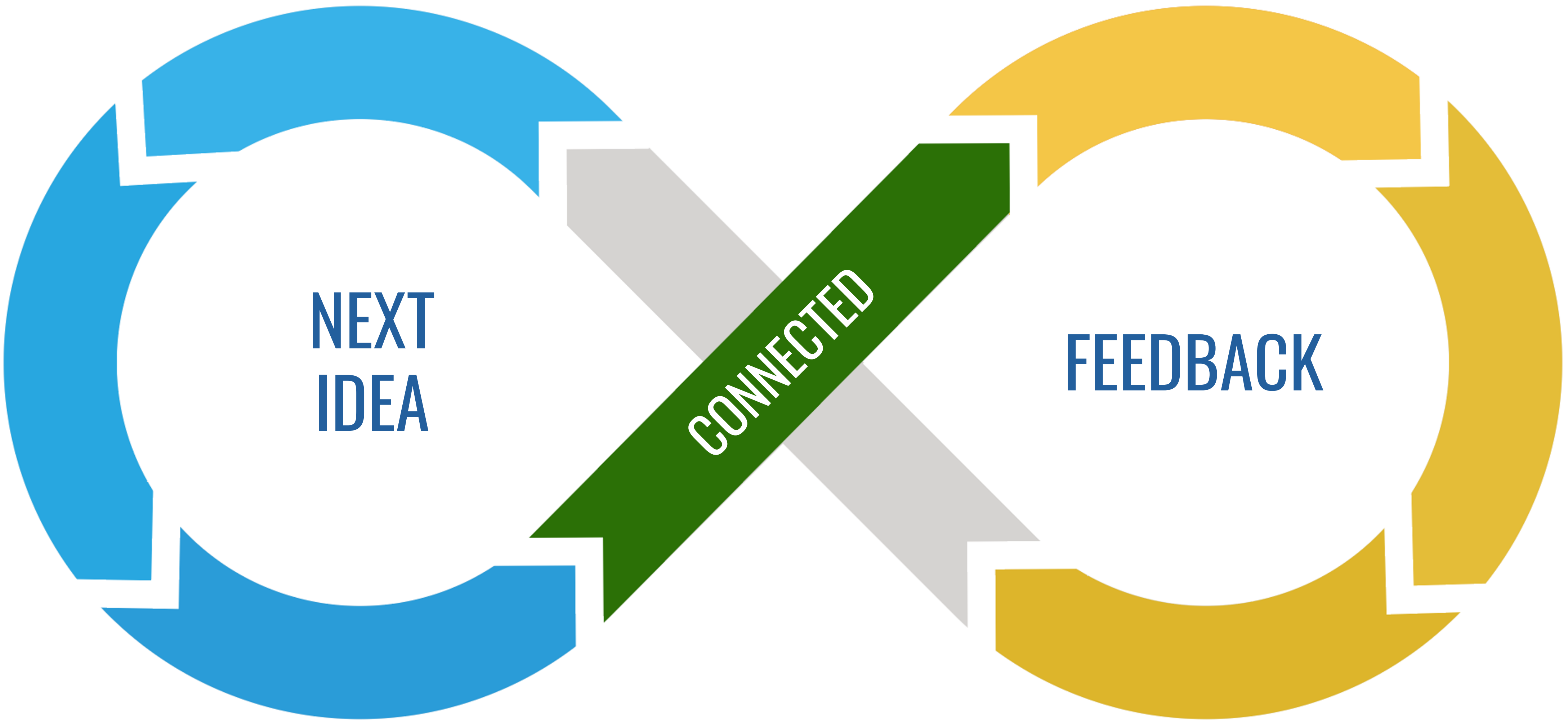

CONTINUOUS SCIENCE

SOFTWARE, STORY & DATA

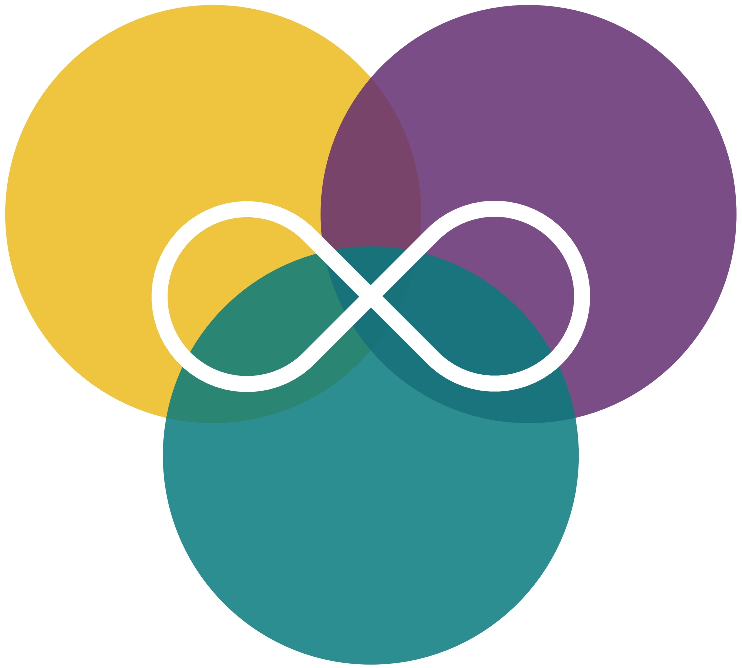

SOFTWARE, STORY & DATA

Events Timeline

The following interactive plot shows all event data to date. Make a selection on the lower bar graph in order to filter points on the top plot. To clear the selection, click on an unselected area of the chart.

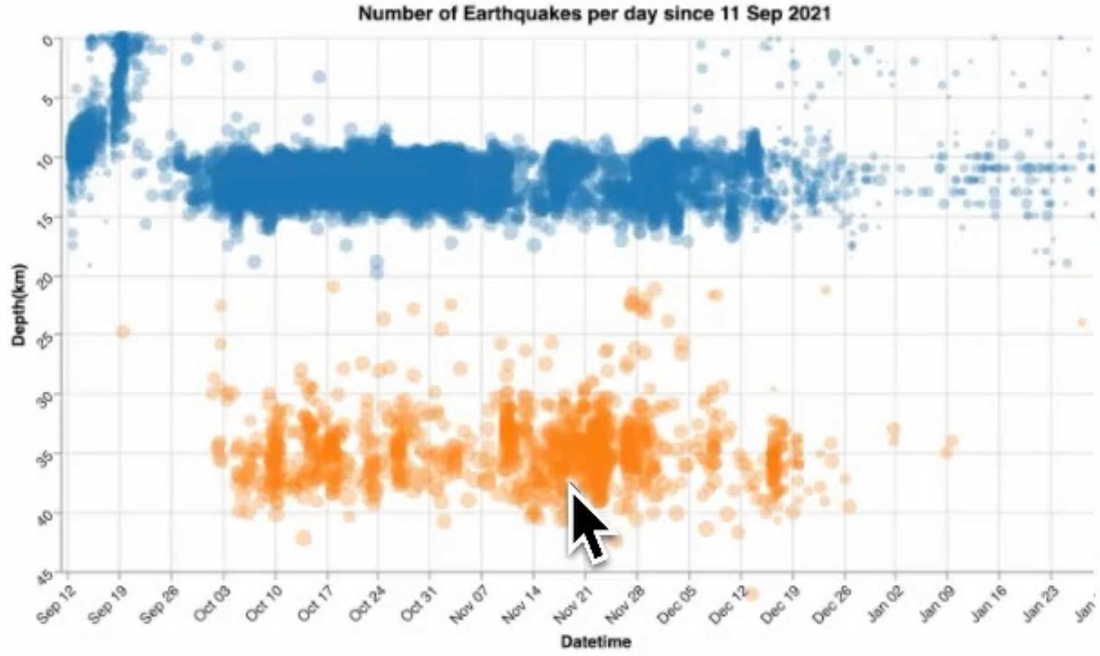

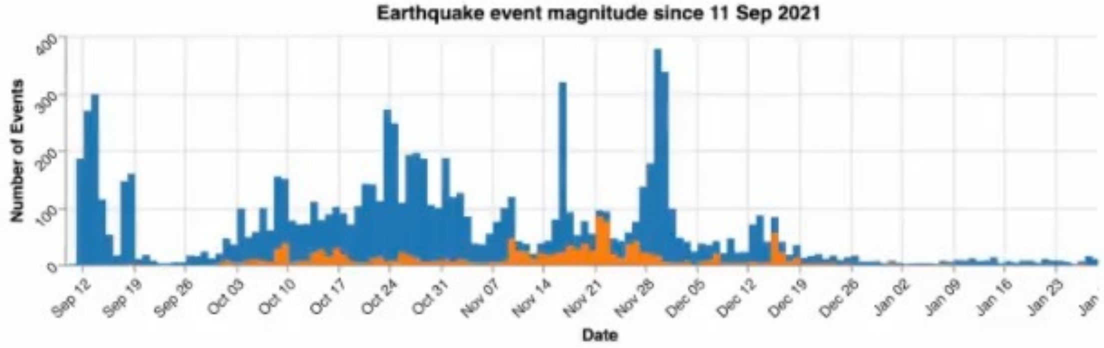

SOFTWARE, STORY & DATA

Note that now all variables are defined over the entire mesh. We could solve this coupled system or we could eliminate $\mathbf{j}$ and solve for ϕ directly (a smaller, second-order system).

$$\mathrm{diag}(\mathbf{v})\mathbf{D}\mathbf{M}_f(\sigma^{-1})^{-1}\mathbf{D}^\top\mathrm{diag}(\mathbf{v})\phi = \mathbf{q} \quad (5)$$

By solving this system matrix, we obtain a solution for the electric potential ϕ everywhere in the domain. Creating predicted data from this requires an interpolation to the electrode locations and subtraction to obtain potential differences!

Source: All Together Now

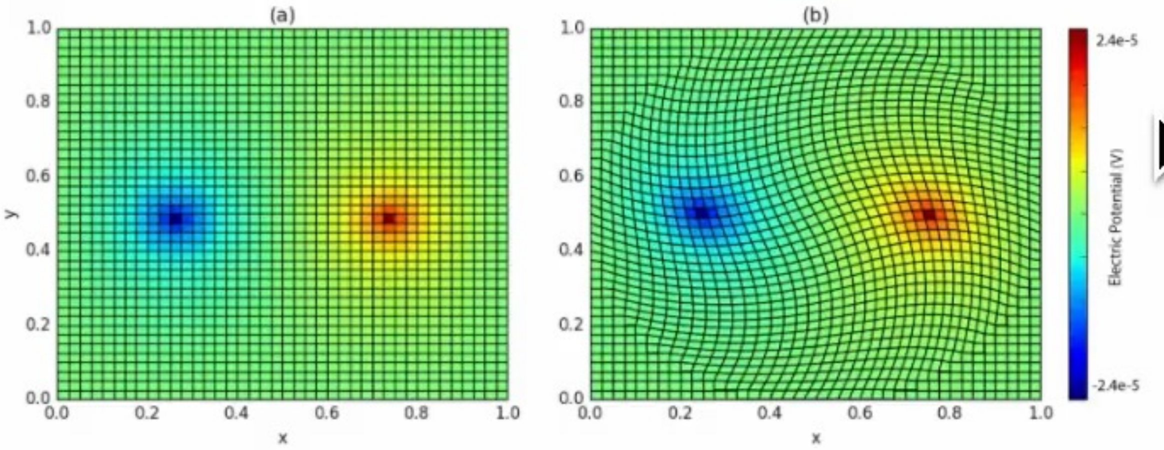

Figure 6: Electric potential on (a) tensor and (b) curvilinear meshes.

Interactive output of the a DC Resistivity simulation.

Moving from continuous equations to their discrete analogues is fundamental in geophysical simulations. In this tutorial, we have started from a continuous description of the governing equations for the DC resistivity problem, selected locations on the mesh to discretize the continuous functions, constructed differential operators by considering one cell at a time, assembled and solved the discrete DC equations. Composing the finite volume system in this way allows us to move to different meshes and incorporate various types of boundary conditions that are often necessary when solving these equations in practice.

LEARNING & DISCOVERY

LEARNING & DISCOVERY

As you have seen in the links in MyST (e.g. Frontmatter), there is information that is pulled forward into your reading context on hover or click. We believe it is important to provide as much possible context when you are reading on elements like links to other pages, cross-references to figures, tables and equations as well as traditional academic citations[2] (👈 **click the footnote!**). Additionally, all of these have fallbacks in static PDF or Word documents.

To link to a document, for example Frontmatter, is done through a simple Markdown link `[](./frontmatter.md)`, you can put your own content in between the square brackets, but if you leave it out the link contents will be filled in with the title of the page. If you define the frontmatter on that page (i.e. the description and tooltip), you will also see that information when you hover over the link. This also works for links to Wikipedia (e.g. *Ponyies*) as well as Github code (e.g. *README.md*).

To create a cross-reference, you need to label a "target", like a figure, section, equation or table (or anything!!). To be referenceable, these elements can add the `label` option in many directives. To then reference the figure, use the link syntax again pointing to the label as the target `[](#my-fig)`. If you leave the title blank the default will fill in with an enumerated "Figure 1".

````
```{figure} https://source.unsplash.com/random/500x200/?mountain
:name: my-fig
:align: center

My **bold** mountain 🏔🚠.
```

Check out [](#my-fig)!!
````

LEARNING & DISCOVERY

Scaling up annual removal

Let's look at a slightly different case, we're going to look at the cost of scaling up annual volume up to 10Gt a year. This time suppose we are currently removing 500 tonnes of carbon from the atmosphere at a unit cost of $592. To locate ourselves on the cost curve also suppose cumulatively we have removed 23,000 tonnes of carbon in total & again our learning rate is 19.7%. Now if we increase our tonnes removed by 40% a year in will take 50.0 years for us to reach a 10Gt scale and total cost of this increase will be approximately $268,873,824,800.

One thing to really emphasise about the example is the effect of changing the amount we are scaling up removal each year. Currently this is set to 40% & at this rate, with our other set values, it will take us 50.0 years to get to our 10Gt of removal a year target. The thing I really want to emphasise is that if we increase the yearly growth rate, while it means paying more in any given year it also means that the total cost to scale to our 10Gt target actually *falls*. The reasoning for this is just that if we scale slowly then we are spending more years still paying a lot for carbon removal but not actually yet at our target rate. This leads to the result that in our race to 10Gt a year **increasing speed and minimising total cost work with not against each other.**

Calculating the years to get to 10Gt annual removal

Current annual removal (C)= 500 tonnes
Yearly growth rate (r)= 40%

$$10Gt = C(1+\frac{r}{100})^t$$

$$t = log_{(1+\frac{r}{100})}(\frac{10Gt}{C})$$

$t = 50.0$ years

CONTINUOUS PROCESS

CONTINUOUS PROCESS

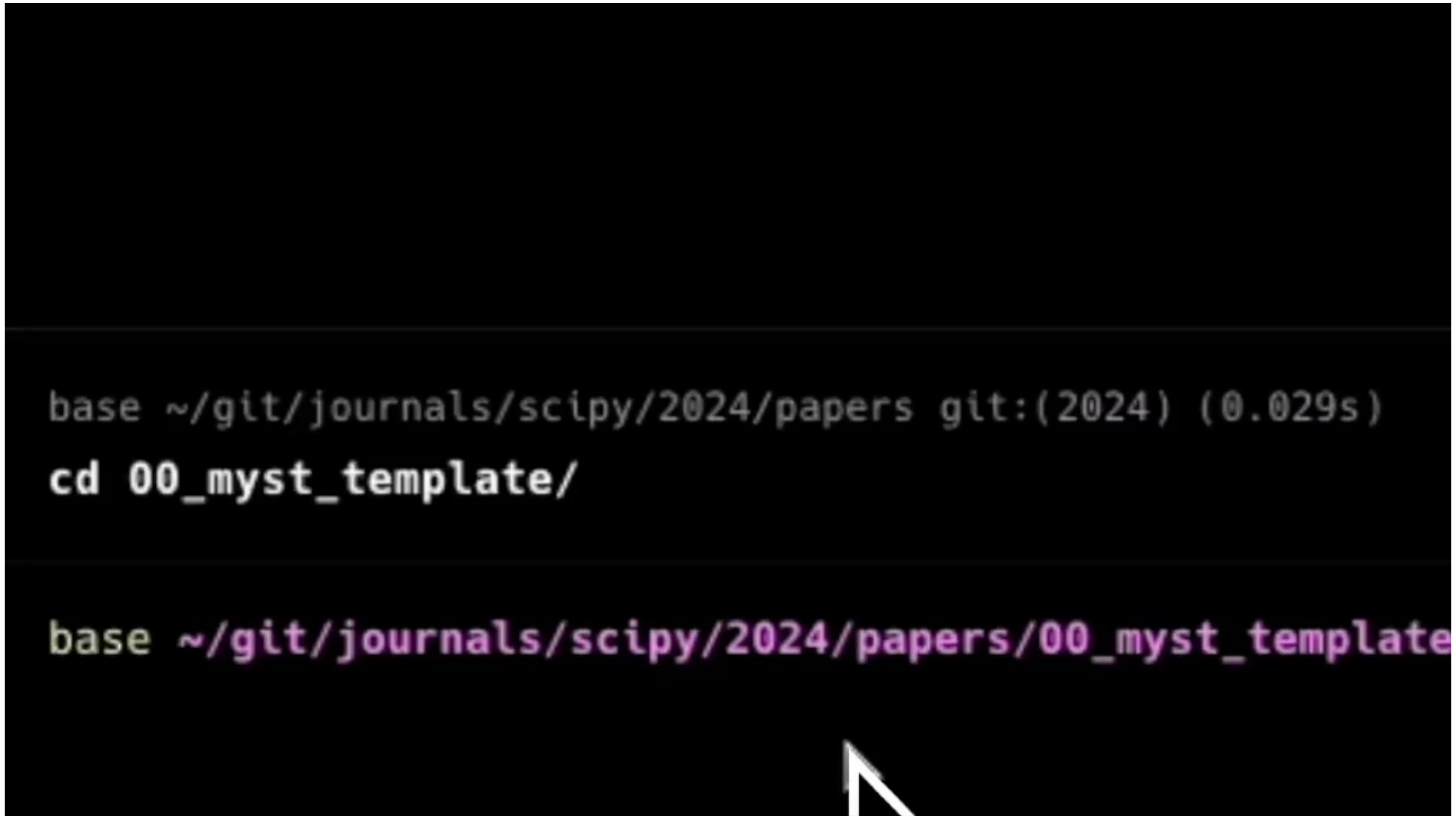

CONTINUOUS PROCESS

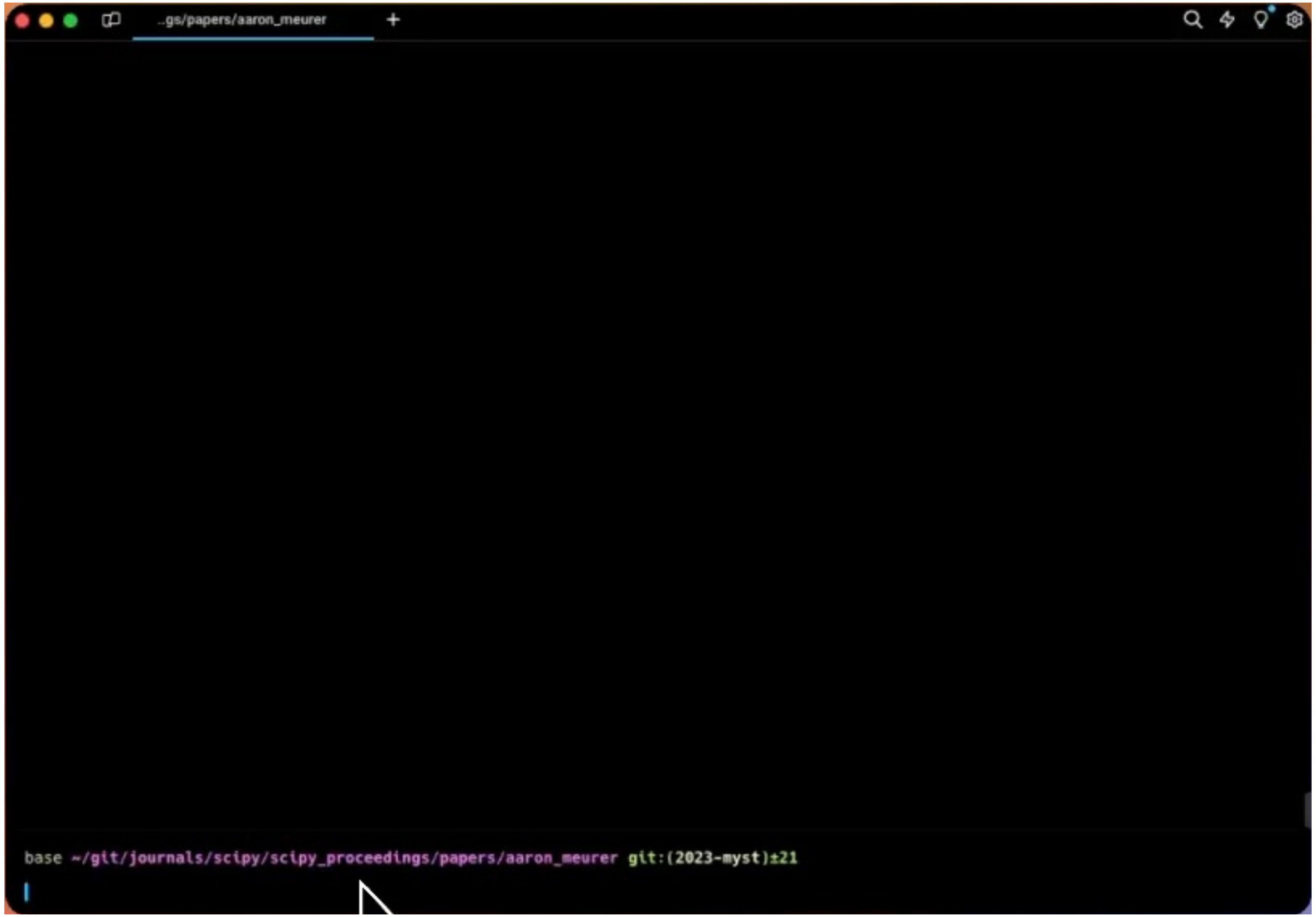

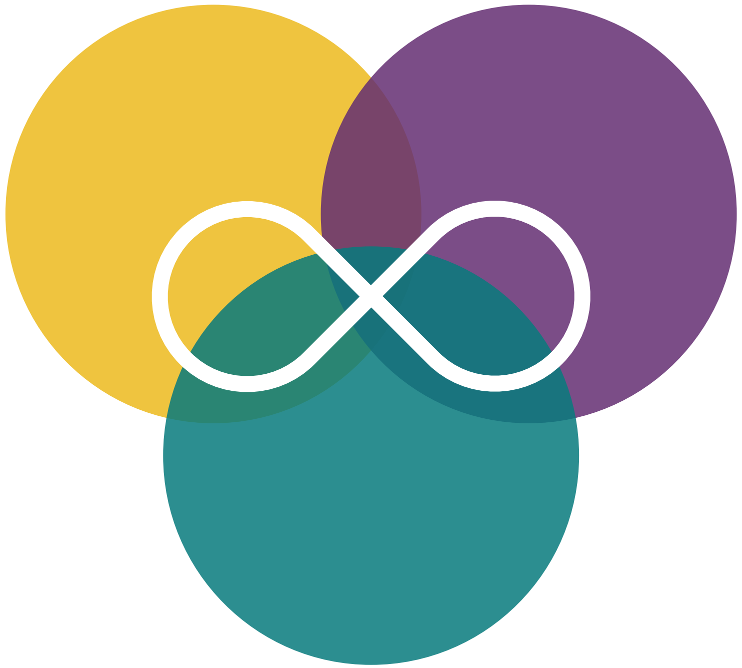

CONTINUOUS PROCESS

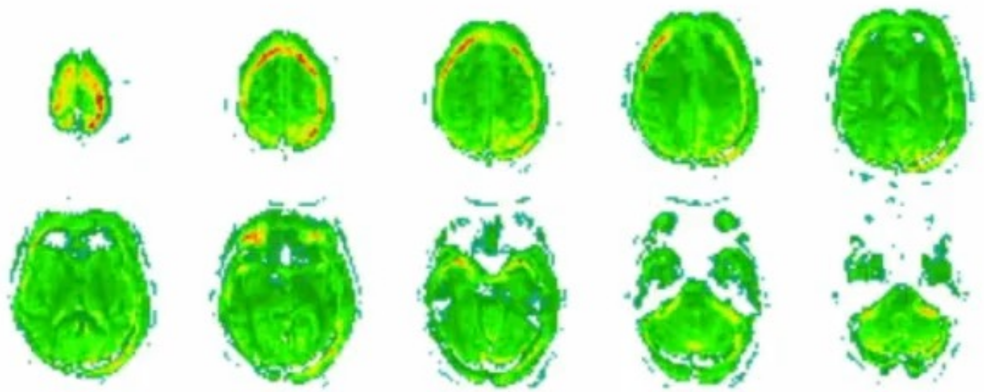

Synthesis

We provide a compressed version of the dataset of (Deligianni *et al.*, 2014). Users can directly execute the code and have both the python package, as well as the dataset, setup in a google colab environment. The flow of execution has been already described. In the end a synthesized fMRI is shown, as illustrated in Figure 2. This image is built using the *viz_utils.py*. The user can find metrics for synthesis evaluation in *eeg_to_fmri.metrics.quantitative_metrics*. We report results from the (Calhas & Henriques, 2022) study on the NODDI dataset (Deligianni *et al.*, 2014). An examp[…] best model, which used the config[…] 0.3972 RMSE and 0.4613 SSIM. This consti[…] applied in EEG only datasets for classification task.

Calhas, D., & Henriques, R. (2022) […]G to fMRI Synthesis Benefits from Attentional Graphs of Electrode Relationships. *arXiv Preprint arXiv:2203.03481*. 10.48550/arXiv.2203.03481

Classification

Figure 4: Output of the predicted fMRI when given an EEG representation. Note that, due to the EEG encoder being optimized towards classifying the data according to the groups of individuals defined, e.g. schizophrenic and healthy controls, the decoder (that has the parameters frozen) gives a slightly altered representation. This change is seen in the produced fMRI, where activity beyond the limit of the human scalp is reported. Please recall Figures 1 and 2 to directly compare with an fMRI representation without these flaws.

We also provide a compressed version of the dataset of (Padée & others, 2022). This example, available in this *classification notebook*, is based on a publicly available dataset that contains individuals diagnosed with schizophrenia and healthy controls. The whole goal of the project is to be applied in an health care setting and to this end we employ an end to end software solution. The whole software package is able to synthesize fMRI and adapt to a classification setting, that given EEG recordings outputs a set of probabilities for each group of people considered in the dataset.

doi.org/10.48550/arXiv.2203.03481

IN THIS ARTICLE

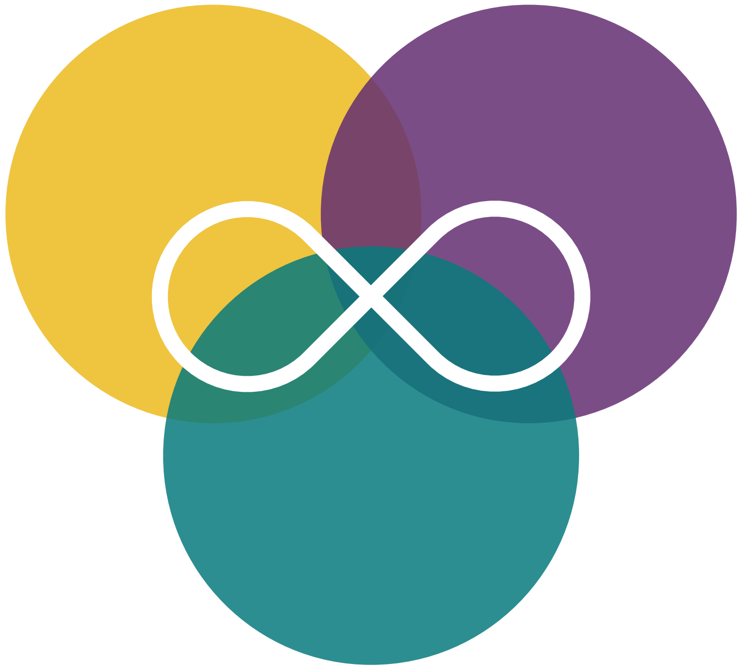

CONTINUOUS PROCESS

Open Access | https://doi.org/10.25080/gerudo-f2bc6f59-008

SciPy 2023
July 10 – July 16, 2023

Proceedings of the 22nd
Python in Science Conference
ISSN: 2575-9752

vak: a neural network framework for researchers studying animal acoustic communication

David Nicholson[1], and **Yarden Cohen**[2]

[1]Independent researcher, Baltimore, Maryland, USA, [2]Weizmann Institute of Science, Rehovot, Israel

Abstract

How is speech like birdsong? What do we mean when we say an animal learns their vocalizations? Questions like these are answered by studying how animals communicate with sound. As in many other fields, the study of acoustic communication is being revolutionized by deep neural network models. These models enable answering questions that were previously impossible to address, in part because the models automate analysis of very large datasets. Acoustic communication researchers have developed multiple models for similar tasks, often implemented as research code with one of several libraries, such as Keras and Pytorch. This situation has created a real need for a framework that allows researchers to easily benchmark multiple models, and test new models, with their own data. To address this need, we developed vak (https://github.com/vocalpy/vak), a neural network framework designed for acoustic communication researchers. ("vak" is pronounced like "talk" or "squawk" and was chosen for its similarity to the Latin root *voc*, as in "vocal".) Here we describe the design of the vak, and explain how the framework makes it easy for researchers to apply neural network models to their own data. We highlight enhancements made in version 1.0 that significantly improve user experience with the library. To provide researchers without expertise in deep learning access to these models, vak can be run via a command-line interface that uses configuration files. Vak can also be used directly in scripts by scientist-coders. To achieve this, vak adapts design patterns and an API from other domain-specific PyTorch libraries such as torchvision, with modules representing neural network operations, models, datasets, and transformations for pre- and post-processing. vak also leverages the Lightning library as a backend, so that vak developers and users can focus on the domain. We provide proof-of-concept results showing how vak can be used to test new models and compare existing models from multiple model families. In closing we discuss our roadmap for development and vision for the community of users.

Keywords animal acoustic communication, bioacoustics, neural networks

Published Jul 10, 2023

Correspondence to
David Nicholson
nicholdav@gmail.com

Data Availability
Source code available:
https://github.com/vocalpy/vak

1. Introduction

Are humans unique among animals? We seem to be the only species that speaks languages [1], but is speech somehow like other forms of acoustic communication in other animals, such as birdsong [2]? How should we even understand the ability of some animals to learn their vocalizations [3]? Questions like these are answered by studying how animals communicate with sound [4]. As others have argued, major advances in this research will require cutting edge computational methods and big team science across a wide range of disciplines, including ecology, ethology, bioacoustics, psychology, neuroscience, linguistics, and genomics [5], [6], [3], [1].

120,000 FPS

480 Gbits/s

OME-Zarr is a file format for storing large multi-dimensional arrays, such as images. It is based on Zarr, which is storage format for a chunked, compressed, N-dimensional array.

There are several viewers that can display OME-Zarr datasets, including the Vizarr, which is a web-based. Web-based viewers are cool because they can be embedded in web pages, like this one 👇:

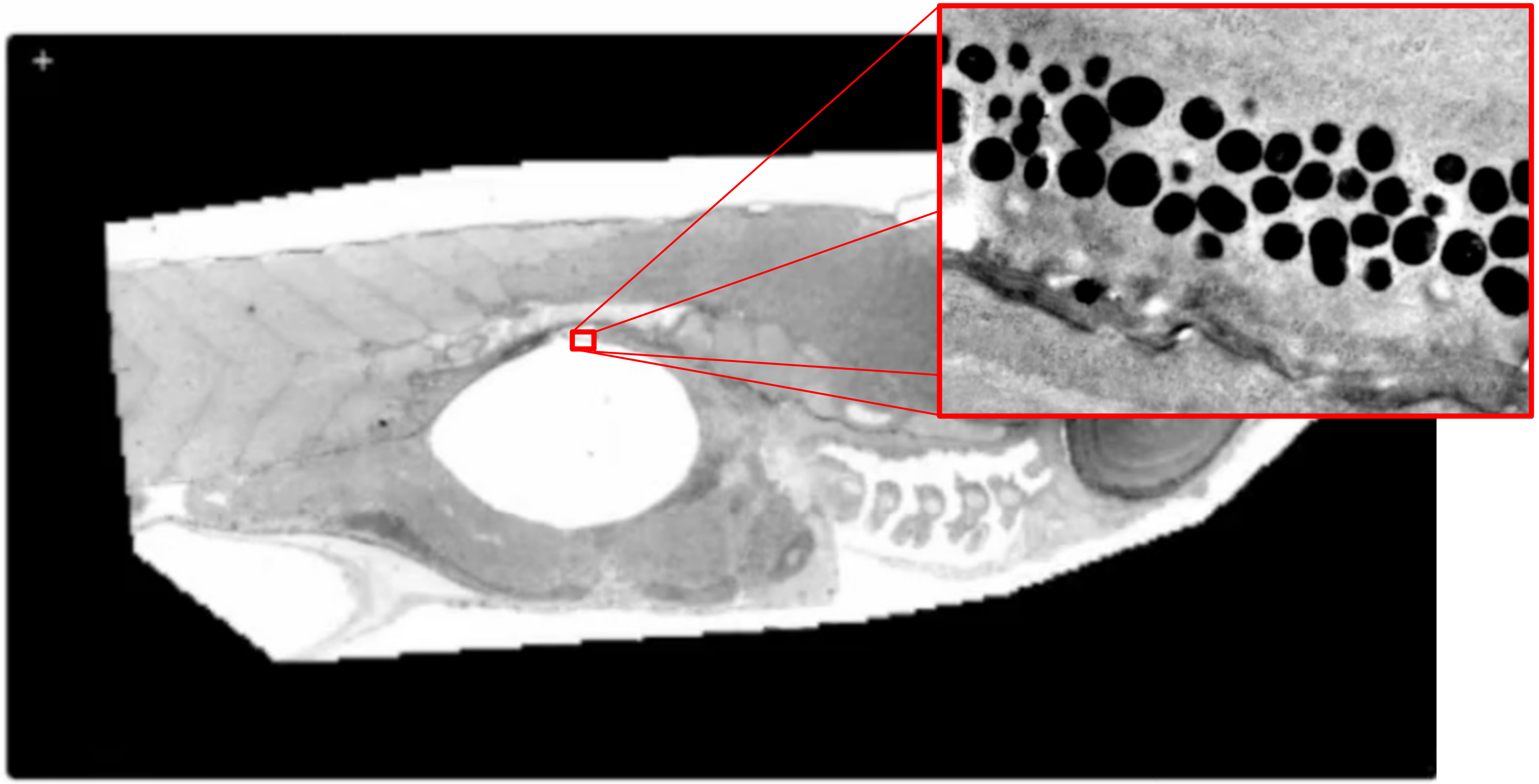

Virtual nanoscopy: generation of ultra-large high resolution electron microscopy maps.

This large electron microscopy dataset is a 1.5TB dataset of a zebrafish embryo, and it is displayed using the Vizarr viewer (Figure 1).

1.5 TB

Elemental Microscopy

We publish focused reviews and tutorials of foundational concepts and modern advances in microscopy-based imaging and spectroscopy techniques in a dynamic multi-media digital format.

Latest Articles

COMPUTATIONAL ARTICLE

Jul 25, 2024

Tilt-Corrected BF-STEM

Computational article on the tilt-corrected bright-field STEM technique -- a dose efficient phase contrast imaging modality which utilizes the principle of reciprocity.

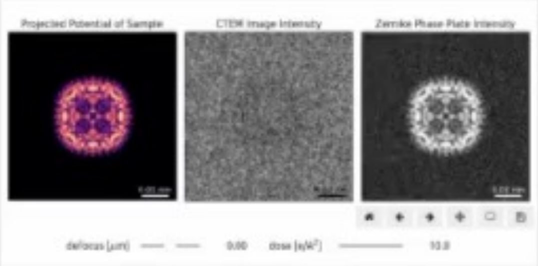

from the ground-truth values (relative rotation angle = -15°, and defocus = 1.5μm), on the apparent image shifts of virtual BF images and the aligned virtual BF stack.

Source: **py4DSTEM Parallax Fitting Notebook**

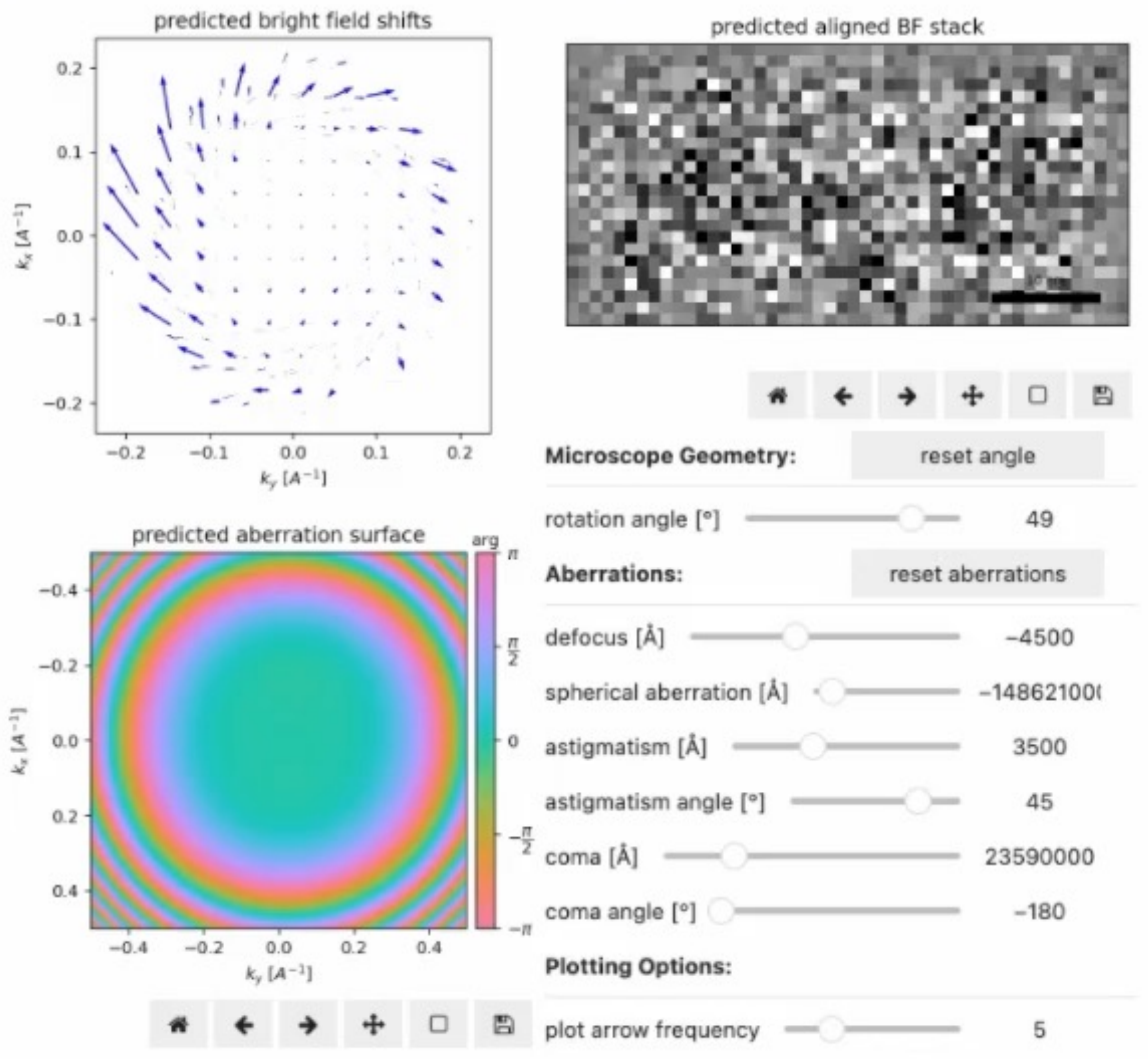

Figure 1: **Common aberrations and microscope geometry effects on tcBF-STEM.** Notice the relative robustness of the aligned BF stack when the `rotation_angle` and `defocus` sliders are moved slightly away from their ground-truth values. Other aberrations, such as astigmatism and coma, introduce more pronounced

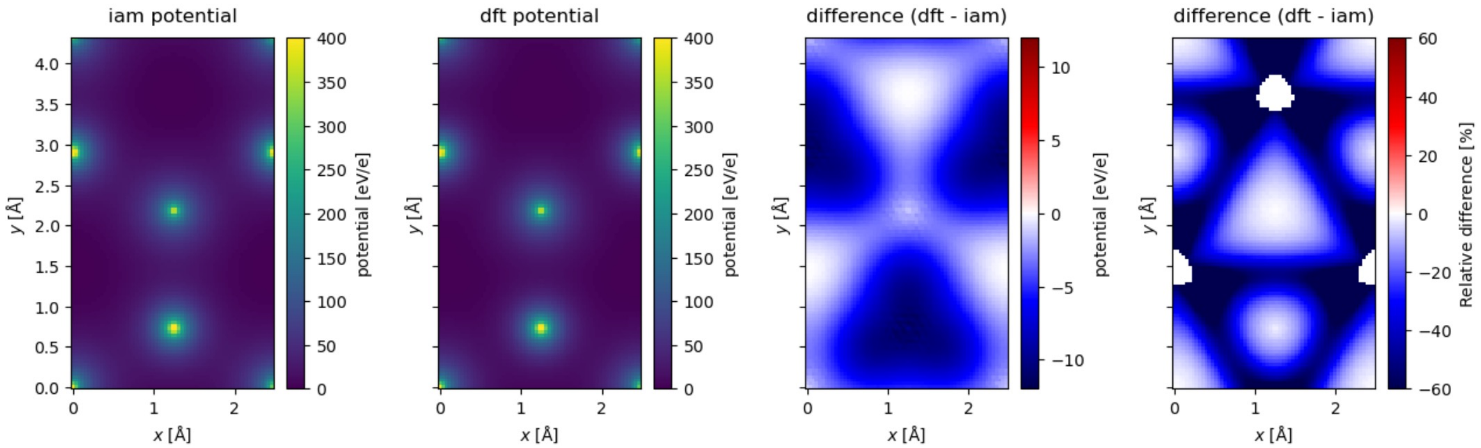

Comparing lineprofiles as below is often a preferable way of showing differences between two images. Below we show the lineprofiles of $x = 0$.

```
iam_line = projected_potential_iam.interpolate_line(
    start=(0, 0), end=(0, projected_potential_iam.extent[1])
)

dft_line = projected_potential_dft.interpolate_line(
    start=(0, 0), end=(0, projected_potential_dft.extent[1])
)

abtem.stack([iam_line, dft_line], ("IAM", "DFT")).show();
```

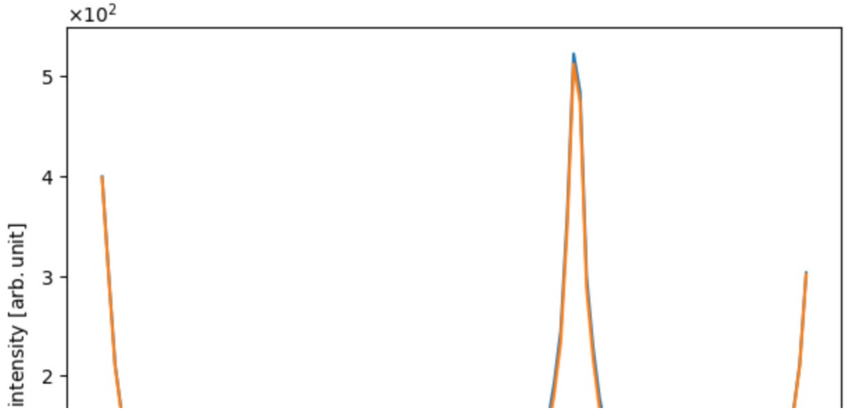

msa-em / tilt-corrected-bf-stem

Type / to search

Code · Issues · Pull requests · Actions · Projects · Security · Insights · Settings

First pass of first draft text #7

Edit | <> Code

Merged gvarnavi merged 16 commits into `main` from `dev` last week

Conversation 1 | Commits 16 | Checks 4 | Files changed 19 | +469 −319

gvarnavi commented last week — Member

Ready for proof-reading.

gvarnavi added 11 commits last week

`removing k3d volume test from this article`	36b097e
`add abstract, competing interests, and acknowledgments`	116e9b5
`updating PCI, no show toggles`	21dae75
`updated reciprocity section, notebooks to remove toggles`	d573b36
`expand caption`	d9941cb
`updating VBFs`	2d4e703
`first half of cross-correlation`	d87e36a
`second half of cross-correlation`	cbf591b

Reviewers
No reviews

Assignees
No one—assign yourself

Labels
None yet

Projects
None yet

Milestone
No milestone

Development
Successfully merging this pull request may close these issues.
None yet

OME-Zarr is a file format for storing large multi-dimensional arrays, such as images. It is based on Zarr, which is storage format for a chunked, compressed, N-dimensional array.

There are several viewers that can display OME-Zarr datasets, including the Vizarr, which is a web-based. Web-based viewers are cool because they can be embedded in web pages, like this one 👇:

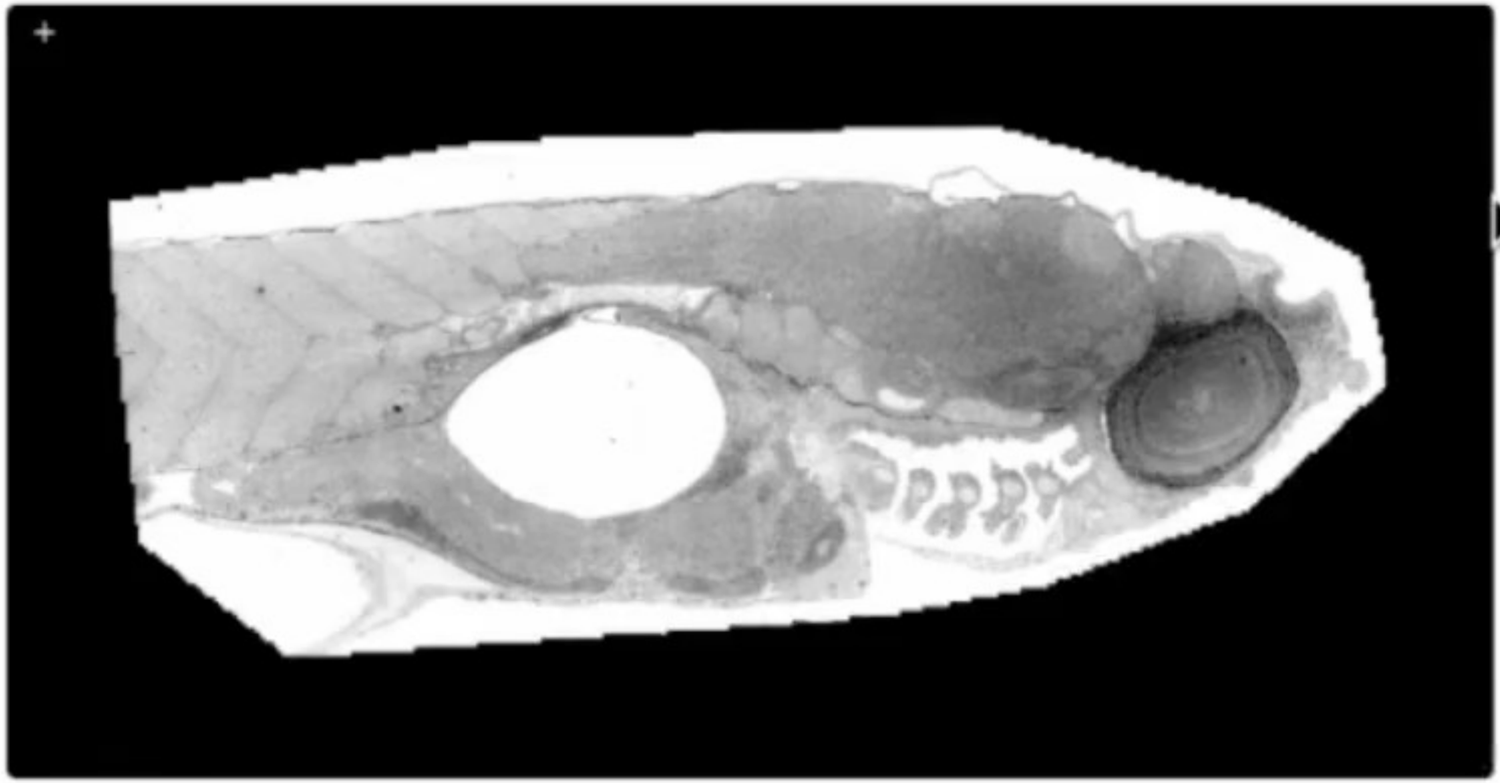

Virtual nanoscopy: generation of ultra-large high resolution electron microscopy maps.

This large electron microscopy dataset is a 1.5TB dataset of a zebrafish embryo, and it is displayed using the Vizarr viewer (Figure 1).

1.5 TB

Mantz *et al.*, 2024

Data

Software

Story

Story

Publications

Peer Reviewed Publications

2021 — Astic, T., **Heagy, L. J.** & Oldenburg, D. W., 2020. Petrophysically and geologically guided multi-physics inversion using a dynamic Gaussian mixture model. *Geophysical Journal International*. doi: 10.1093/gji/ggaa378. arXiv: 2002.09515

Werthmüller, D., Rochlitz, R., Castillo-Reyes, O., & **Heagy, L. J.**, 2021. Towards an open-source landscape for 3D CSEM modelling. *Geophysical Journal International*. doi: 10.1093/gji/ggab238. arXiv: 2010.12926

2020 — Fournier, D., **Heagy, L. J.** & Oldenburg, D. W., 2020. Sparse magnetic vector inversion in spherical coordinates. *Geophysics*. doi: 10.1190/geo2019-0244.1

Heagy, L. J., Kang, S., Cockett, R. & Oldenburg, D. W., 2020. Open source software for simulations and inversions of airborne electromagnetic data. *Exploration Geophysics*. doi: 10.1080/08123985.2019.1583538. arXiv: 1902.08238

Kang, S., Oldenburg, D. W. & **Heagy, L. J.**, 2020. Detecting induced polarization effects in time-domain data: a modeling study using stretched exponentials. *Exploration Geophysics*. doi: 10.1080/08123985.2019.1690393. arXiv: 1909.12993

Oldenburg, D. W., **Heagy, L. J.**, Kang, S. & Cockett, R., 2020. 3D electromagnetic modelling and inversion: a case for open source. *Exploration Geophysics*. doi: 10.1080/08123985.2019.1580118. arXiv: 1902.08245

2019 — **Heagy, L. J.** & Oldenburg, D. W., 2019. Modeling electromagnetics on cylindrical meshes with applications to steel-cased wells. *Computers & Geosciences*. doi: 10.1016/j.cageo.2018.11.010. arXiv: 1804.07991

Heagy, L. J. & Oldenburg, D. W., 2019. Direct current resistivity with steel-cased wells. *Geophysical Journal International*. doi: 10.1093/gji/ggz281. arXiv: 1810.12446

2018 — Cockett, R., **Heagy, L. J.** & Haber, E., 2018. Efficient 3D inversions using the Richards equation. *Computers & Geosciences*. doi: 10.1016/j.cageo.2018.04.006

2017 — **Heagy, L. J.**, Cockett, R., Kang, S., Rosenkjaer, G. K., & Oldenburg, D. W., 2017. A framework for simulation and inversion in electromagnetics. *Computers & Geosciences*. doi: 10.1016/j.cageo.2017.06.018

Caudillo-Mata, L. A., Haber, E., **Heagy, L. J.** & Schwarzbach, C., 2017. A framework for the upscaling of the electrical conductivity in the quasi-static Maxwell's equations. *Journal of Computational and Applied Mathematics*. doi: 10.1016/j.cam.2016.11.051

2015 — Cockett, R., Kang, S., **Heagy, L. J.**, Pidlisecky, A. & Oldenburg, D. W., 2015. SimPEG: An open source framework for simulation and gradient based parameter estimation in geophysical applications. *Computers & Geosciences*. doi: 10.1016/j.cageo.2015.09.015

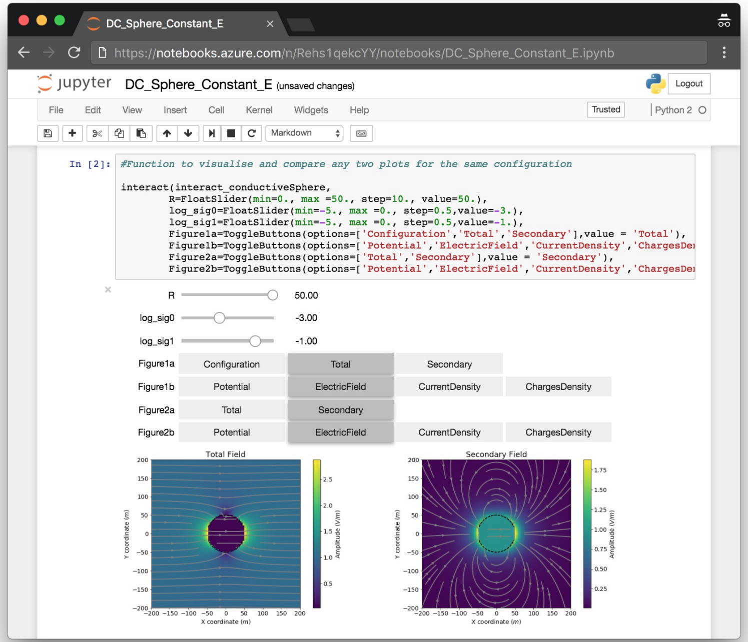
DC_Sphere_Constant_E
https://notebooks.azure.com/n/Rehs1qekcYY/notebooks/DC_Sphere_Constant_E.ipynb
jupyter DC_Sphere_Constant_E (unsaved changes)
Logout
File Edit View Insert Cell Kernel Widgets Help
Trusted
Python 2
Markdown
In [2]:
#Function to visualise and compare any two plots for the same configuration
interact(interact_conductiveSphere,
R=FloatSlider(min=0., max =50., step=10., value=50.),
log_sig0=FloatSlider(min=-5., max =0., step=0.5,value=-3.),
log_sig1=FloatSlider(min=-5., max =0., step=0.5,value=-1.),
R 50.00
log_sig0 -3.00
log_sig1 -1.00
Figure1a Configuration Total Secondary
Figure1b Potential ElectricField CurrentDensity ChargesDensity
Figure2a Total Secondary
Figure2b Potential ElectricField CurrentDensity ChargesDensity
Total Field
Secondary Field

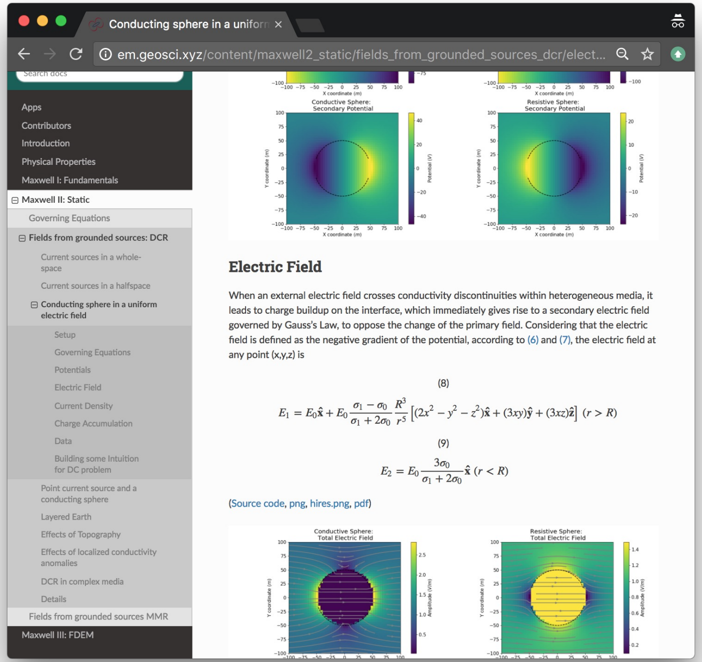
Conducting sphere in a uniform
em.geosci.xyz/content/maxwell2_static/fields_from_grounded_sources_dcr/elect...
Apps
Contributors
Introduction
Physical Properties
Maxwell I: Fundamentals
Maxwell II: Static
Governing Equations
Fields from grounded sources: DCR
Current sources in a whole-space
Current sources in a halfspace
Conducting sphere in a uniform electric field
Setup
Governing Equations
Potentials
Electric Field
Current Density
Charge Accumulation
Data
Building some Intuition for DC problem
Point current source and a conducting sphere
Layered Earth
Effects of Topography
Effects of localized conductivity anomalies
DCR in complex media
Details
Fields from grounded sources MMR
Maxwell III: FDEM
Electric Field
When an external electric field crosses conductivity discontinuities within heterogeneous media, it leads to charge buildup on the interface, which immediately gives rise to a secondary electric field governed by Gauss's Law, to oppose the change of the primary field. Considering that the electric field is defined as the negative gradient of the potential, according to (6) and (7), the electric field at any point (x,y,z) is
(8)
(9)
(Source code, png, hires.png, pdf)
Conductive Sphere: Total Electric Field
Resistive Sphere: Total Electric Field

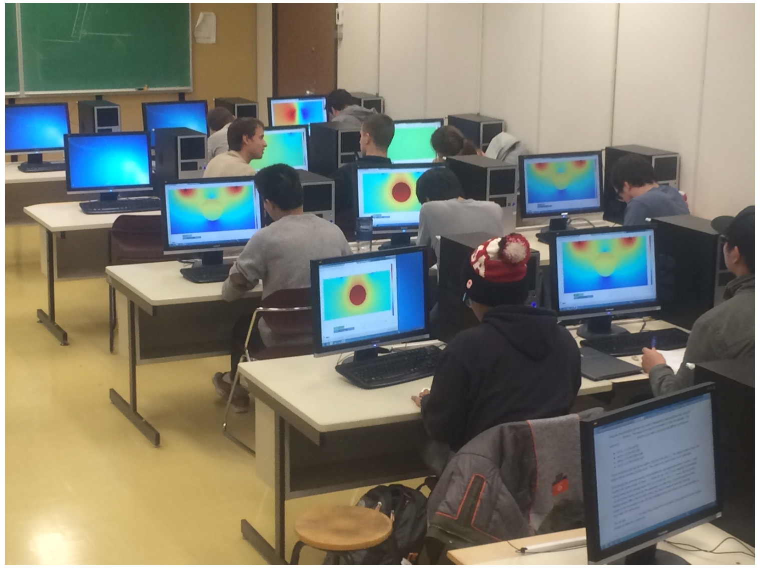


AGU
Home Showcase Author Instructions
Curvenote
RESEARCH ARTICLE AGU NOTEBOOKS NOW Volume 8, Issue 12
pyUserCalc: A Revised Jupyter Notebook Calculator for Uranium-Series Disequilibria in Basalts
Lynne J. Elkins, Marc Spiegelman
October 1, 2021 · https://doi.org/10.1029/2020EA001619
Download PDF
Download TEX
Learn More
Launch Binder
Abstract
IN THIS ARTICLE
Introduction

Research!

Publish


Research!
Publish

Geophysical Inversion Facility

UBC-GIF advances methods in computational geophysics to solve applied problems. Explore our recent research, presentations, and projects

Recent Research   Read our Mission

Latest Research

Publications | Article
Jan 1, 2020

Detecting induced polarisation effects in time-domain data - a modelling study using stretched exponentials

The effects of the background conductivity are investigated; this study shows that a moderately conductive and chargeable target in a resistive host is an ideal scenario for generating strong IP signals

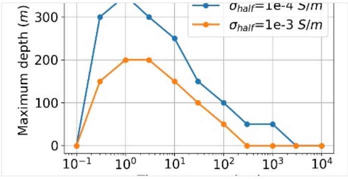

Publications | Article
Oct 12, 2020

Joint inversion of potential-fields data over the DO-27 kimberlite pipe using a Gaussian mixture model prior

Producing a quasi-geology model that presents good structural locations of the diamondiferous PK unit and can be used to provide a resource estimate or decide the locations of future drillholes.

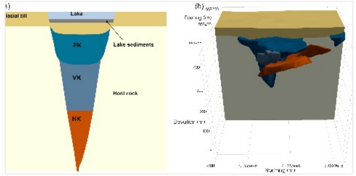

Publications | Article
Aug 30, 2019

A framework for petrophysically and geologically guided geophysical inversion using a dynamic Gaussian mixture model prior

Applying our framework to inverting airborne frequency domain data, acquired in Australia, for the detection and characterization of saline contamination of freshwater.

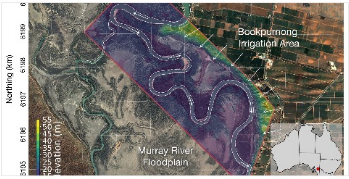

```
    cbar1[ii].set_label("%", labelpad=5, size=12)

plt.show(fig)
```

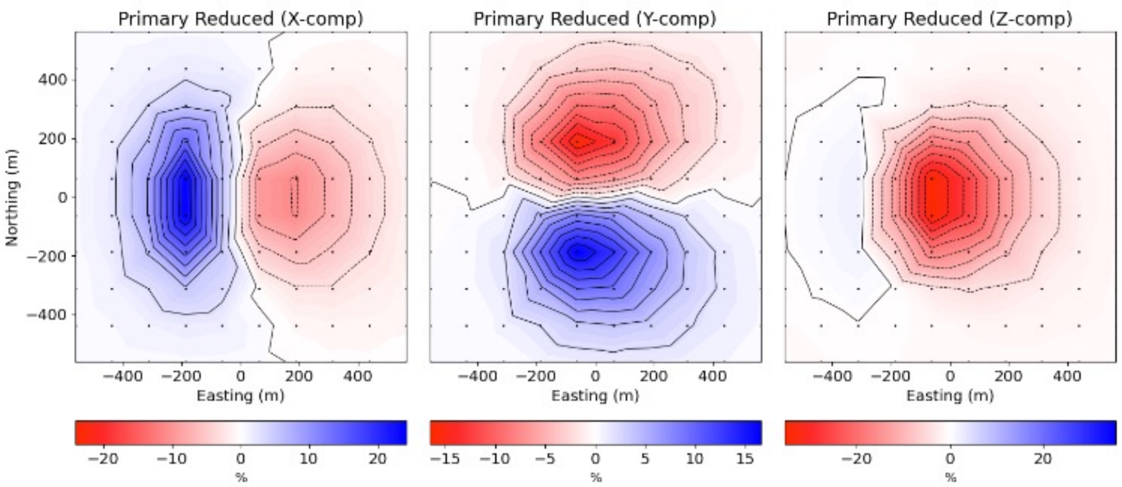

TDEM Profile

Here, we plot the TDEM profile for the Northing position specified.

```
EW_line_index = 6

y_unique = np.unique(receiver_locations[:, 1])
locations_indices = receiver_locations[:, 1] == y_unique[EW_line_index]

fig = plt.figure(figsize=(15, 5))
ax1 = [fig.add_axes([0.05 + 0.3 * ii, 0.2, 0.24, 0.75]) for ii in range(0, 3)]

comp_list = ["X", "Y", "Z"]

for ii in range(0, 3):
    d_temp = data_plotting[ii][:, locations_indices]

    for jj in range(n_times):
        ax1[ii].plot(
```

SimPEG User Tutorials
Gravity
Magnetics
Direct Current Resistivity
Induced Polarization
Frequency-Domain Electromagnetics
Time-Domain Electromagnetics
1D Forward Simulation for a Single Sounding
Fundamentals of Finite Volume for TDEM Simulations
3D Forward Simulation for On-Time Large-Loop Data
1D Inversion for a Single Sounding

SimPEG Seminar

March 2022: Seogi Kang

How do we plot a resistivity model from airborne electromagnetic data?

Seogi Kang

March 24, 2022

Abstract

The use of airborne electromagnetic (AEM) data for geoscience applications is rapidly increasing. For instance, in California USA, there is an ongoing AEM project led by the California Department of Water Resources (CDWR), which plans to map out most of the Central Valley of California and some water basins in California: https://water.ca.gov/Programs/Groundwater-Management/Data-and-Tools/AEM All acquired AEM data and resulting interpretation of the data, which are resistivity models of the subsurface will be publicly available. There are many big initiatives like this project throughout the world (e.g., AusAEM: https://www.ga.gov.au/eftf/minerals/nawa/ausaem). Therefore, it is critical to understand how the resulting resistivity models are obtained from the acquired AEM data, and further equipped with an ability to download and explore the available resistivity data. In this talk, I will first introduce how a resistivity model is obtained from the AEM data then introduce open-source tools that can be used to explore this resistivity model.

March 24th, 2022 @ 10 am PT

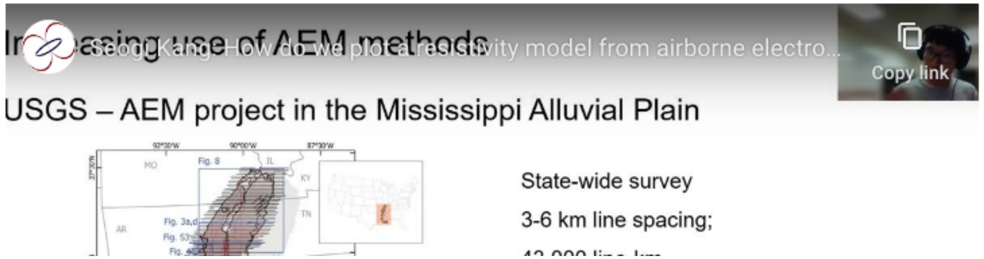

Applied Geophysics
Our Mission and Approach
Open Science
Presentations
Publications

Publications

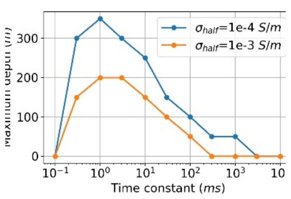

Detecting induced polarisation effects in time-domain data - a modelling study using stretched exponentials

The effects of the background conductivity are investigated; this study shows that a moderately conductive and chargeable target in a resistive host is an ideal scenario for generating strong IP signals

ARTICLE Jan 1, 2020

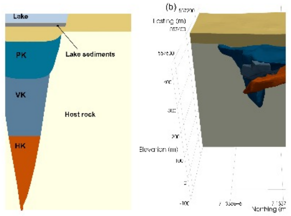

Joint inversion of potential-fields data over the DO-27 kimberlite pipe using a Gaussian mixture model prior

Producing a quasi-geology model that presents good structural locations of the diamondiferous PK unit and can be used to provide a resource estimate or decide the locations of future drillholes.

ARTICLE Oct 12, 2020

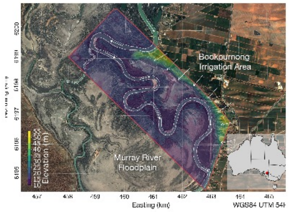

A framework for petrophysically and geologically guided geophysical inversion using a dynamic Gaussian mixture model prior

Applying our framework to inverting airborne frequency domain data, acquired in Australia, for the detection and characterization of saline contamination of freshwater.

ARTICLE Aug 30, 2019

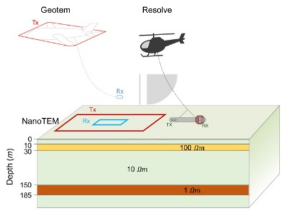

3D electromagnetic modelling and inversion - a case for open source

Presenting arguments for adopting an open-source methodology for geophysics and provide some background about open-source software for electromagnetics.

ARTICLE Jan 1, 2020

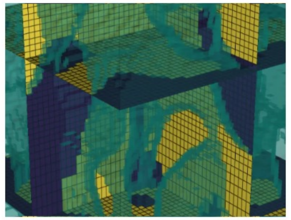

Efficient 3D inversions using the Richards equation

Fluid flow in the vadose zone, governed by the Richards equation, requires characterizing hydraulic properties using direct and proxy measurements. We present an efficient inversion technique for 1D, 2D, and 3D hydraulic properties, implemented in SimPEG, enabling large-scale inversions with modest resources.

ARTICLE Jul 1, 2018

Geophysical Inversion Facility

Research group at the University of British Columbia

Pinned

appliedgeophysics.org Public
1

Repositories

Find a repository... Type Language Sort New

2024-kuttai-automated_rotation_for_regularization Private
Using segmentation and rotated regularization gradients to automate geolgical orientation from geophysical inversion
Jupyter Notebook 0 0 0 0 Updated 16 hours ago

2022-peacock-etal-computers-and-geosciences Public
MTH5 - An archive and exchangeable data format for magnetotelluric time series data
0 0 1 1 Updated 3 days ago

2021-werthmuller-etal-gji Public
Towards an open-source landscape for 3-D CSEM modelling
0 0 0 1 Updated 3 days ago

2020-kang-etal-exploration-geophysics-aem-ip Public
TeX 1 0 0 0 Updated 5 days ago

2020-astic-etal-interpretation Public
Joint inversion of potential-fields data over the DO-27 kimberlite pipe using a Gaussian mixture model prior
TeX 0 0 0 0 Updated 5 days ago

2019-astic-oldenburg-gji Public

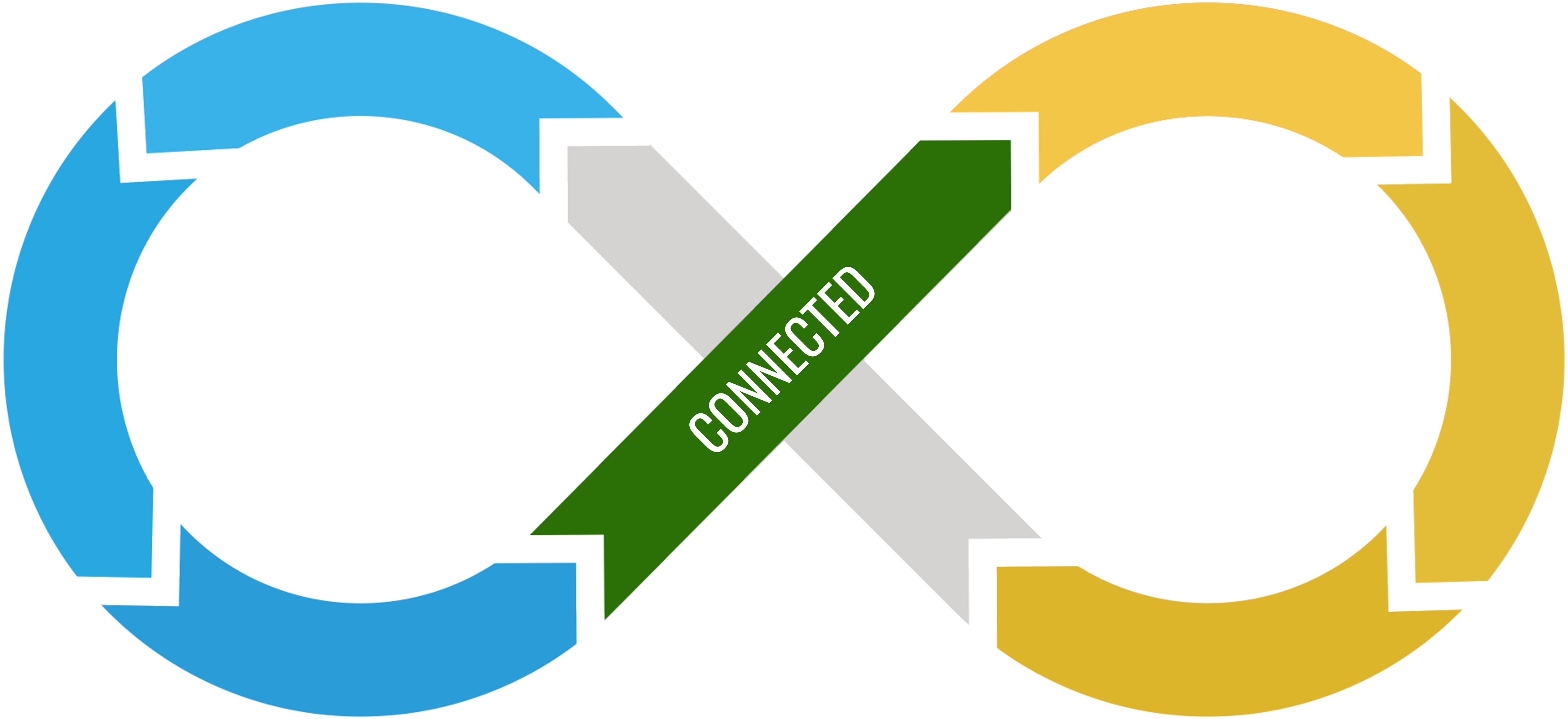

CONTINUOUS SCIENCE

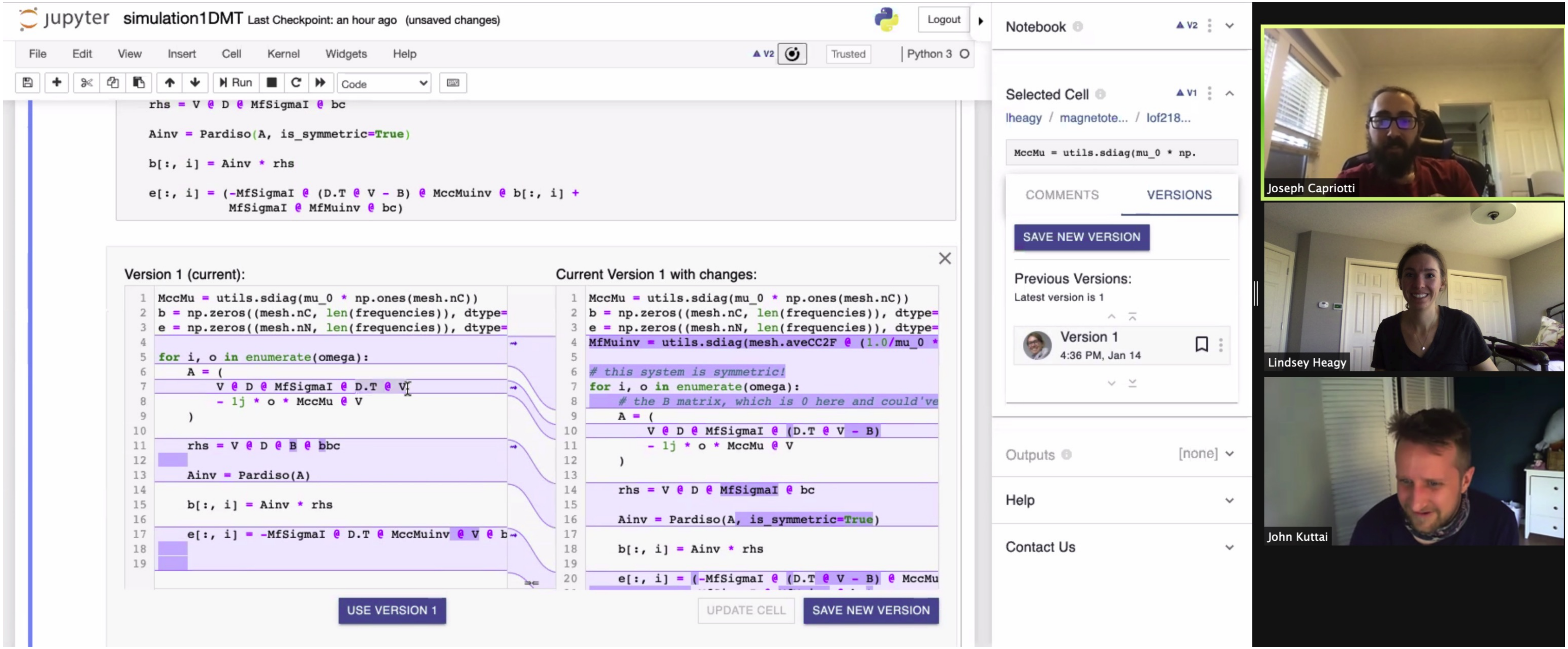
jupyter simulation1DMT Last Checkpoint: an hour ago (unsaved changes)
Logout
File Edit View Insert Cell Kernel Widgets Help
V2 Trusted Python 3
Run Code
rhs = V @ D @ MfSigmaI @ bc
Ainv = Pardiso(A, is_symmetric=True)
b[:, i] = Ainv * rhs
e[:, i] = (-MfSigmaI @ (D.T @ V - B) @ MccMuinv @ b[:, i] +
MfSigmaI @ MfMuinv @ bc)
Version 1 (current):
MccMu = utils.sdiag(mu_0 * np.ones(mesh.nC))
b = np.zeros((mesh.nC, len(frequencies)), dtype=
e = np.zeros((mesh.nN, len(frequencies)), dtype=
for i, o in enumerate(omega):
A = (
V @ D @ MfSigmaI @ D.T @ V
- 1j * o * MccMu @ V
)
rhs = V @ D @ B @ bbc
Ainv = Pardiso(A)
b[:, i] = Ainv * rhs
e[:, i] = -MfSigmaI @ D.T @ MccMuinv @ V @ b
Current Version 1 with changes:
MccMu = utils.sdiag(mu_0 * np.ones(mesh.nC))
b = np.zeros((mesh.nC, len(frequencies)), dtype=
e = np.zeros((mesh.nN, len(frequencies)), dtype=
MfMuinv = utils.sdiag(mesh.aveCC2F @ (1.0/mu_0 *
# this system is symmetric!
for i, o in enumerate(omega):
# the B matrix, which is 0 here and could've
A = (
V @ D @ MfSigmaI @ (D.T @ V - B)
- 1j * o * MccMu @ V
)
rhs = V @ D @ MfSigmaI @ bc
Ainv = Pardiso(A, is_symmetric=True)
b[:, i] = Ainv * rhs
e[:, i] = (-MfSigmaI @ (D.T @ V - B) @ MccMu
USE VERSION 1
UPDATE CELL
SAVE NEW VERSION
Notebook V2
Selected Cell V1
lheagy / magnetote... / lof218...
MccMu = utils.sdiag(mu_0 * np.
COMMENTS VERSIONS
SAVE NEW VERSION
Previous Versions:
Latest version is 1
Version 1
4:36 PM, Jan 14
Outputs [none]
Help
Contact Us
Joseph Capriotti
Lindsey Heagy
John Kuttai

illa *BD*. Eodem argumento in fine temporis ejuſdem reperietur alicubi in linea *CD*, & idcirco in utriuſq; lineæ concurſu *D* reperiri neceſſe eſt.

Corol. II.

Et hinc patet compoſitio vis directæ AD ex viribus quibuſvis obliquis AB & BD, & viciſſim reſolutio vis cujuſvis directæ AD in obliquas quaſcunq; AB & BD. Quæ quidem Compoſitio & reſolutio abunde confirmatur ex Mechanica.

Ut ſi de rotæ alicujus centro O exeuntes radij inæquales *OM*, *ON* filis *MA*, *NP* ſuſtineant pondera *A* & *P*, & quærantur vires ponderum ad movendam rotam: per centrum O agatur recta *KOL* filis perpendiculariter occurrens in *K* & *L*, centroq; O & intervallorum *OK*, *OL*, majore *OL*, deſcribatur circulus occurrens filo *MA* in *D*: & actæ rectæ *OD* parallela ſit *AC* & perpendicularis *DC*. Quoniam nihil refert utrum filorum puncta *K*, *L*, *D* affixa ſint vel non affixa ad planum rotæ, pondera idem valebunt ac ſi ſuſpenderentur a punctis *K* & *L* vel *D* & *L*. Ponderis autem *A* exponatur vis tota per lineam *AD*, & hæc reſolvetur in vires *AC*, *CD*, quarum *AC* trahendo radium *OD* directe a centro nihil valet ad movendam rotam; vis autem altera *DC*, trahendo radium *DO* perpendiculariter, idem valet ac ſi perpendiculariter traheret radium *OL* ipſi *OD* æqualem; hoc eſt idem atq; pondus *P*, ~~quod ſit~~ ad pondus *A* ut vis *DC* ad vim *DA*, id eſt (ob ſimilia triangula *ADC*, *DOK*,) ut OK (ad OD) ſit ad OL. Pondera igitur *A* & *P*, quæ ſunt reciproce ut radii in directum poſiti *OK* & *OL*, idem pollebunt & ſic conſiſtent in æquilibrio: (quæ eſt proprietas notiſſima Libræ, Vectis

Si modo pondus illud ſit

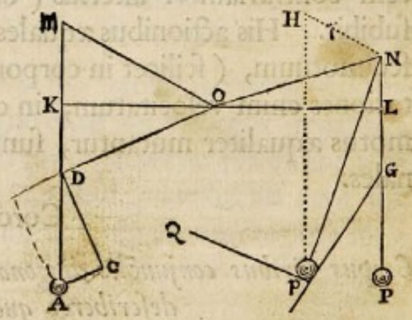

propagation time, the events have a combined signal-to-noise ratio (SNR) of 24 [45].

Only the LIGO detectors were observing at the time of GW150914. The Virgo detector was being upgraded, and GEO 600, though not sufficiently sensitive to detect this event, was operating but not in observational mode. With only two detectors the source position is primarily determined by the relative arrival time and localized to an area of approximately 600 deg^2 (90% credible region) [39,46].

The basic features of GW150914 point to it being produced by the coalescence of two black holes—i.e., their orbital inspiral and merger, and subsequent final black hole ringdown. Over 0.2 s, the signal increases in frequency and amplitude in about 8 cycles from 35 to 150 Hz, where the amplitude reaches a maximum. The most plausible explanation for this evolution is the inspiral of two orbiting masses, m_1 and m_2, due to gravitational-wave emission. At the lower frequencies, such evolution is characterized by the chirp mass [11]

$$\mathcal{M} = \frac{(m_1 m_2)^{3/5}}{(m_1 + m_2)^{1/5}} = \frac{c^3}{G}\left[\frac{5}{96}\pi^{-8/3} f^{-11/3} \dot{f}\right]^{3/5},$$

where f and $\dot{f}$ are the observed frequency and its time derivative and G and c are the gravitational constant and speed of light. Estimating f and $\dot{f}$ from the data in Fig. 1, we obtain a chirp mass of $\mathcal{M} \simeq 30 M_\odot$, implying that the total mass $M = m_1 + m_2$ is $\gtrsim 70 M_\odot$ in the detector frame. This bounds the sum of the Schwarzschild radii of the binary components to $2GM/c^2 \gtrsim 210$ km. To reach an orbital frequency of 75 Hz (half the gravitational-wave frequency) the objects must have been very close and very compact; equal Newtonian point masses orbiting at this frequency would be only $\simeq$350 km apart. A pair of neutron stars, while compact, would not have the required mass, while a black hole neutron star binary with the deduced chirp mass would have a very large total mass, and would thus merge at much lower frequency. This leaves black holes as the only known objects compact enough to reach an orbital frequency of 75 Hz without contact. Furthermore, the decay of the waveform after it peaks is consistent with the damped oscillations of a black hole relaxing to a final stationary Kerr configuration. Below, we present a general-relativistic analysis of GW150914; Fig. 2 shows the calculated waveform using the resulting source parameters.

III. DETECTORS

Gravitational-wave astronomy exploits multiple, widely separated detectors to distinguish gravitational waves from local instrumental and environmental noise, to provide source sky localization, and to measure wave polarizations. The LIGO sites each operate a single Advanced LIGO detector [33], a modified Michelson interferometer (see Fig. 3) that measures gravitational-wave strain as a difference in length of its orthogonal arms. Each arm is formed by two mirrors, acting as test masses, separated by $L_x = L_y = L = 4$ km. A passing gravitational wave effectively alters the arm lengths such that the measured difference is $\Delta L(t) = \delta L_x - \delta L_y = h(t)L$, where h is the gravitational-wave strain amplitude projected onto the detector. This differential length variation alters the phase difference between the two light fields returning to the beam splitter, transmitting an optical signal proportional to the gravitational-wave strain to the output photodetector.

To achieve sufficient sensitivity to measure gravitational waves, the detectors include several enhancements to the basic Michelson interferometer. First, each arm contains a resonant optical cavity, formed by its two test mass mirrors, that multiplies the effect of a gravitational wave on the light phase by a factor of 300 [48]. Second, a partially transmissive power-recycling mirror at the input provides additional resonant buildup of the laser light in the interferometer as a whole [49,50]: 20 W of laser input is increased to 700 W incident on the beam splitter, which is further increased to 100 kW circulating in each arm cavity. Third, a partially transmissive signal-recycling mirror at the output optimizes

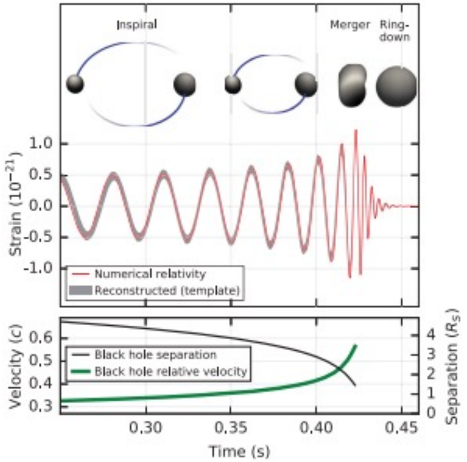

FIG. 2. *Top:* Estimated gravitational-wave strain amplitude from GW150914 projected onto H1. This shows the full bandwidth of the waveforms, without the filtering used for Fig. 1. The inset images show numerical relativity models of the black hole horizons as the black holes coalesce. *Bottom:* The Keplerian effective black hole separation in units of Schwarzschild radii ($R_S = 2GM/c^2$) and the effective relative velocity given by the post-Newtonian parameter $v/c = (GM\pi f/c^3)^{1/3}$, where f is the gravitational-wave frequency calculated with numerical relativity and M is the total mass (value from Table I).

propagation time, the events have a combined signal-to-noise ratio (SNR) of 24 [45].

Only the LIGO detectors were observing at the time of GW150914. The Virgo detector was being upgraded, and GEO 600, though not sufficiently sensitive to detect this event, was operating but not in observational mode. With only two detectors the source position is primarily determined by the relative arrival time and localized to an area of approximately 600 deg^2 (90% credible region) [39,46].

The basic features of GW150914 point to it being produced by the coalescence of two black holes—i.e., their orbital inspiral and merger, and subsequent final black hole ringdown. Over 0.2 s, the signal increases in frequency and amplitude in about 8 cycles from 35 to 150 Hz, where the amplitude reaches a maximum. The most plausible explanation for this evolution is the inspiral of two orbiting masses, m_1 and m_2, due to gravitational-wave emission. At the lower frequencies, such evolution is characterized by the chirp mass [11]

$$\mathcal{M} = \frac{(m_1 m_2)^{3/5}}{(m_1 + m_2)^{1/5}} = \frac{c^3}{G}\left[\frac{5}{96}\pi^{-8/3} f^{-11/3} \dot{f}\right]^{3/5},$$

where f and $\dot{f}$ are the observed frequency and its time derivative and G and c are the gravitational constant and speed of light. Estimating f and $\dot{f}$ from the data in Fig. 1, we obtain a chirp mass of $\mathcal{M} \simeq 30 M_\odot$, implying that the total mass $M = m_1 + m_2$ is $\gtrsim 70 M_\odot$ in the detector frame. This bounds the sum of the Schwarzschild radii of the binary components to $2GM/c^2 \gtrsim 210$ km. To reach an orbital frequency of 75 Hz (half the gravitational-wave frequency) the objects must have been very close and very compact; equal Newtonian point masses orbiting at this frequency would be only $\simeq$350 km apart. A pair of neutron stars, while compact, would not have the required mass, while a black hole neutron star binary with the deduced chirp mass would have a very large total mass, and would thus merge at much lower frequency. This leaves black holes as the only known objects compact enough to reach an orbital frequency of 75 Hz without contact. Furthermore, the decay of the waveform after it peaks is consistent with the damped oscillations of a black hole relaxing to a final stationary Kerr configuration. Below, we present a general-relativistic analysis of GW150914; Fig. 2 shows the calculated waveform using the resulting source parameters.

III. DETECTORS

Gravitational-wave astronomy exploits multiple, widely separated detectors to distinguish gravitational waves from local instrumental and environmental noise, to provide source sky localization, and to measure wave polarizations. The LIGO sites each operate a single Advanced LIGO

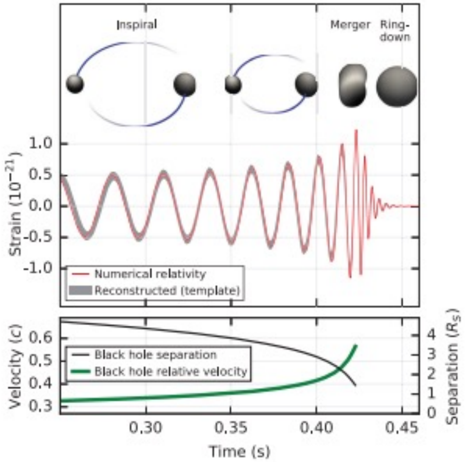

FIG. 2. *Top:* Estimated gravitational-wave strain amplitude from GW150914 projected onto H1. This shows the full bandwidth of the waveforms, without the filtering used for Fig. 1. The inset images show numerical relativity models of the black hole horizons as the black holes coalesce. *Bottom:* The Keplerian effective black hole separation in units of Schwarzschild radii ($R_S = 2GM/c^2$) and the effective relative velocity given by the post-Newtonian parameter $v/c = (GM\pi f/c^3)^{1/3}$, where f is the gravitational-wave frequency calculated with numerical relativity and M is the total mass (value from Table I).

detector [33], a modified Michelson interferometer (see Fig. 3) that measures gravitational-wave strain as a difference in length of its orthogonal arms. Each arm is formed by two mirrors, acting as test masses, separated by $L_x = L_y = L = 4$ km. A passing gravitational wave effectively alters the arm lengths such that the measured difference is $\Delta L(t) = \delta L_x - \delta L_y = h(t)L$, where h is the gravitational-wave strain amplitude projected onto the detector. This differential length variation alters the phase difference between the two light fields returning to the beam splitter, transmitting an optical signal proportional to the gravitational-wave strain to the output photodetector.

To achieve sufficient sensitivity to measure gravitational waves, the detectors include several enhancements to the basic Michelson interferometer. First, each arm contains a resonant optical cavity, formed by its two test mass mirrors, that multiplies the effect of a gravitational wave on the light phase by a factor of 300 [48]. Second, a partially transmissive power-recycling mirror at the input provides additional resonant buildup of the laser light in the interferometer as a whole [49,50]: 20 W of laser input is increased to 700 W incident on the beam splitter, which is further increased to 100 kW circulating in each arm cavity. Third, a partially transmissive signal-recycling mirror at the output optimizes

MSA Curvenote

COMPUTATIONAL ARTICLE ELEMENTAL MICROSCOPY

Nanocartography: Planning for success in analytical electron microscopy

Matthew J Olszta, Kevin R Fiedler

June 11, 2023 · https://doi.org/10.69761/DNKA1581

› Contents

Tilt series for TEM foils can also be performed along a single orthogonal axis (whether it be α or β) using a double tilt stage, but there are limitations to this approach. Depending on the orientation of objects within the TEM foil, especially when they are oriented obliquely to the stage axes, single axis tilt series may not provide a clear picture. For instance, when a grain boundary decorated with precipitates is tilted in a non-logical manner (i.e., not against its long axis) it is difficult to observe the full distribution of precipitates or voids on the boundary. Yet, when the boundary is tilted against its long axis, the boundary moves in a logical fashion, and the distribution can be readily observed (Badwe *et al.*, 2018) (). Equally important, if not more, is the ability to create tilt series along specific planes of atoms that can be beneficial to demonstrate dislocation microstructures in three dimensions (Liu & Robertson, 2011; Hata *et al.*, 2020; Yamasaki *et al.*, 2015).

Source: Ag-Au Interactive Movie


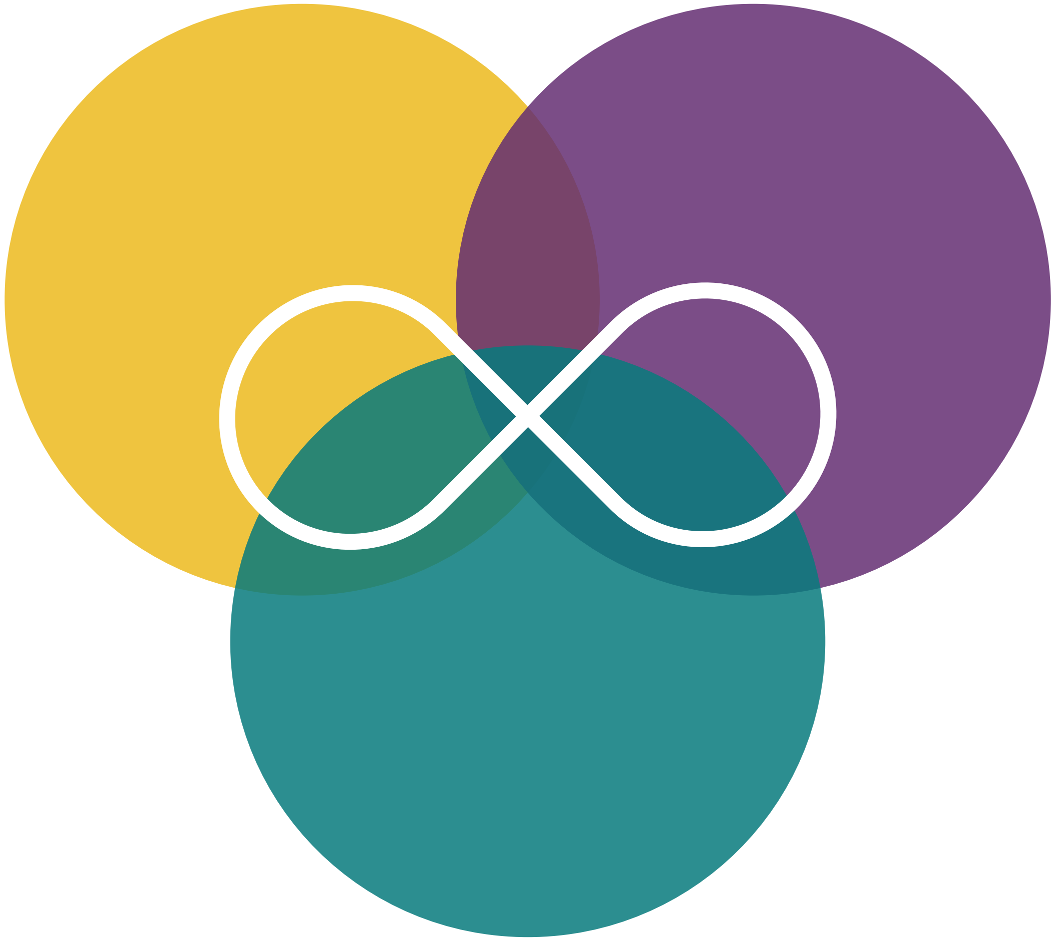

LET'S CHAT

Curvenote

rowan@curvenote.com

{MyST}

mystmd.org